UNIVERSITY OF CALIFORNIA
RIVERSIDE

Measurement of Neutral Pions and Direct Photons in Cu + Cu Collisions at 62.4 GeV Center of Mass Energy

A Dissertation submitted in partial satisfaction
of the requirements for the degree of

Doctor of Philosophy

in

Physics

by

Timothy James Hester

June 2012

Dissertation Committee:

Professor Kenneth Barish, Chairperson
Professor Richard Seto
Professor Robert Clare

The Dissertation of Timothy James Hester is approved:

Committee Chairperson

University of California, Riverside

Acknowledgments

I thank my advisor Dr. Kenneth Barish for his enthusiastic support and generosity over the years. I was never led to feel small about any mistakes I made in the pursuit of my research. He allowed me to follow my curiosity and always met my questions with patience and thought provoking answers.

I would also like to thank the other members of my dissertation committee. Dr. Richard Seto was always available to me as a valuable source of knowledge of high energy nuclear physics, and Dr. Robert Clare, whose excellent instruction in both my undergraduate and graduate courses inspired pursuit in the field. Also, I greatly appreciate the assistance of Drs. Richard Hollis and Aneta Iordanova. The day–to–day communication with both of them on many topics, physics and more, made this work achievable.

Oleg Eyser, Ondrej Chvala, Gabor David, and Stefan Bathe also provided knowledge and experience that was invaluable, and I would like to thank them for their assistance.

I would like to thank the Department of Physics and Astronomy for providing me with this opportunity and for the education I received at the hands of so many capable instructors, especially Dr. Gordon VanDalen, who mentored me as an undergraduate and fueled in me a passion for physics. I thank the department staff for providing me with the means to continue my efforts, in particular Luci Pacocha and Barbara Simandl.

My graduate experience at UC Riverside was rich, and at times, trying. I would not have made it through the first few years if it were not for my fellow classmates. In particular I would like to thank Jojit Torcedo, Ken James and Peter Hunana, who kept my sanity during those times when it seemed I had lost it.

Lastly, I would like to thank my family, especially my parents for all their support, and little Rose and Adam, who provided wonderful distractions.

Dedicated to my parents.
Their unwavering support made this work possible.

ABSTRACT OF THE DISSERTATION

Measurement of Neutral Pions and Direct Photons in Cu + Cu Collisions at 62.4 GeV Center of Mass Energy

by

Timothy James Hester

Doctor of Philosophy, Graduate Program in Physics
University of California, Riverside, June 2012
Professor Kenneth Barish, Chairperson

Direct-photons measured with the PHENIX detector at RHIC, in Au+Au collisions, have been found to scale with the number of binary (nucleon-nucleon) collisions at large transverse momenta. In contrast, earlier measurements from RHIC, using charged and neutral hadron spectra, showed a clear suppression with respect to pp collisions. That suppression was interpreted to be due to the energy loss of scattered partons in the produced dense medium in heavy-ion collisions. Thus, it is concluded that such an energy loss is not evident for direct-photons. In order to understand the turn-on of these effects, similar measurements have been subsequently made for Cu+Cu collisions at various collision energies. This work will present a new measurement of direct photons in Cu+Cu collisions at $\sqrt{s} =$ 62.4 GeV. The smaller system size may provide new insight into the system size dependence of photon production. These data will be compared to pp collision data, as well as neutral pion spectra from the same collision data, to check for modification of particle production due to effects of the system created in the heavy ion collisions.

Contents

List of Figures

List of Tables

Chapter 1

Introduction

The strong nuclear force binds protons and neutrons (nucleons) in atomic nuclei, and also binds the smallest constituents of matter, quarks and gluons, into nucleons and other particles. The physical processes of this force, which arise when colliding elementary particles, have been described very well by the Quantum Chromodynamics (QCD) [1, 2] theory over the past several decades[3]. A natural question arises: What more can QCD tell us about the nature of matter? Are there other interesting realms left to be explored? How does nuclear matter behave under the intense conditions inside neutron stars, or more to the point, in the very first fractions of a second after the Big Bang? In that brief time of the early Universe all the matter and energy that currently exists today did so then, just in a very small Universe, compacted to an extreme density and temperature.

The collision of heavy ions at high energy is theoretically expected to recreate this extreme environment of high energy density, and hence provides the opportunity to study such matter in the laboratory. In this environment quarks move freely, they are *deconfined*, i.e. they are no longer restricted inside hadrons. These free quarks can interact with each other via the strong nuclear force, bringing QCD into the forefront of the physics of heavy ion collision, and allowing the study of the conditions of the early Universe.

cite:AGSsite

Over the past several decades experiments at the Alternating Gradient Synchrotron (AGS [4] at Brookhaven National Laboratory (BNL)[5] and at the Super Proton Synchrotron (SPS)[6] at the European Center for Nuclear Research (CERN)[7] have studied heavy ion collisions of many different species and energies. During this time the search for a state of matter with freed quarks has provided many interesting results. However, confirmation of

the creation of the conditions close to that of the early Universe was not achieved.

To continue the effort, at BNL in the first year of the new millennium, the Relativistic Heavy Ion Collider (RHIC) began taking physics data. RHIC offered the possibility to increase the collision energies of heavy ions by more than 10 times what had been studied previously. In terms of heavy ion research, RHIC's goal was to confirm the freedom of quarks from their nuclei, and to do this, gold ions were first collided at a center–of–mass energy of 56 GeV and 130 GeV, and then one year later at 200 GeV.

The PHENIX experiment, a collaborative effort of hundreds of scientists, was first to report one of RHIC's prominent results: the suppression of hadron production in Au+Au collisions at $\sqrt{s} =$ 130 GeV [8]. This result suggested the formation of a novel medium in RHIC collisions, which was strongly interacting with partons produced in the collisions. Subsequent results by PHENIX and STAR (another of the four original experiments on the RHIC ring) confirmed the creation of this new form of nuclear matter, with the observation of the suppression of back–to–back jets of particles in central (head–on) heavy ion collisions [9].

In order to better understand the properties of the created medium, the question arose of what energy and system size does this suppression begin to occur? If the suppression was not present in the smaller system sizes (non–central or glancing collisions), nor in energies used in past experiments, yet is present at RHIC, at what point does hadron suppression begin? Studying the particle production in heavy ion collisions, and in particular photon production, can help to answer these questions. Photons interact only via the electromagnetic force, whereas quarks couple to the strong force. The medium created at RHIC, being strongly coupled, interacts with quarks (and antiquarks) and leads to the observed hadron suppression. Photons do not interact with the medium, thus they provide a calibration of the underlying physics processes, prior to any interaction with the medium.

During the 2005 run at RHIC, Cu+Cu collisions at center–of–mass energies of 22.4, 62.4, and 200 GeV per nucleon provided data to be analyzed with the aim of investigating the turn–on of hadron suppression. This Thesis presents the results from both hadron (specifically neutral pion) and photon production in the Cu+Cu system using data collected by the PHENIX detector.

1.1 Quantum Chromodynamics

In the early twentieth century the basic building blocks of matter were beginning to be explored. Scientists such as J. J. Thomson and Ernest Rutherford (discoverers of the electron and atomic nucleus, respectively), among many others, were accumulating evidence of the structure of atoms. This eventually led to the realization that the atomic nucleus was a collection of positively charged and electrically neutral components. This was intriguing at the time, as the electro–static force between same–sign electric charges should repel them causing the nucleus to fly apart, or simply not to form in the first place.

Thomson's famous "plum pudding" model described atoms as "corpuscles" of negative charge embedded in a positively charged medium; negative plums in a positive pudding. Later experiments under the direction of Rutherford using accelerated alpha particles to probe atoms on a thin gold foil led to the discovery of the atomic nucleus and a better description of the atom. The "nucleus model" saw the atom as having a small, dense inner region of positive electric charge surrounded by layers of negative charge. The move from the plum pudding model to the nucleus model was possible only because the energy of the experimental probes increased. With the extra energy, or momentum, smaller distances were explored[1], which resulted in more detailed information about the atom. This increase in energy led to further discoveries, such as nuclei composed of protons and neutrons (nucleons), and later to the discovery of the smallest building blocks of matter, quarks and gluons. It is possible that further subquark structure may be found at an even higher energy (maybe at the LHC at CERN).

To understand how a nucleus consisting of only neutral and positively–charged particles can stay bound together, a new theory was needed. By the mid–twentieth century it was understood that the like sign electric charges of the protons in nuclei should repel one another, and that some other, stronger force must be in play to keep the protons in close proximity. The strong force is also responsible for binding the quarks and gluons inside the protons and neutrons. After many different attempts to understand how the quarks and gluons are bound together by the strong force, a new theory emerged, the theory of Quantum Chromodynamics or QCD. QCD is a field theory that can be thought of as analogous to quantum electrodynamics (QED), the quantum theory of electromagnetism. There are however some notable differences. First, unlike QED (which has one charge and

[1]The correlation between higher energy and smaller distance can be seen in the Heisenberg Uncertainty Priniple where a change in momentum corresponds inversely to a change in distance ($\Delta p \sim \frac{1}{\Delta x}$)

its corresponding anti–charge), QCD has three charges. The three charges of QCD were likened to the three primary colors, which is where the "chromo" comes–in, thus the name "color force". The QCD theory describes the quarks, the building blocks of nuclear matter, as color charged particles, and gluons as the force carriers between the quarks. Although the quarks have color, colored matter does not exist. When quarks combine to form normal matter, their colors must "blend", resulting in colorless particles – hadrons.

Hadrons, (protons, neutrons, pions, etc.) come in two varieties: mesons are quark–antiquark pairs ($q\bar{q}$), which have color and anticolor, and baryons contain 3 quarks (qqq), each with a different color (or 3 antiquarks: $\bar{q}\bar{q}\bar{q}$, each with a different anti–color). Another, important way that QCD differs from QED is that the force carriers also are charge carriers. This means that unlike photons, gluons can interact with each other.

The QCD potential between a quark and anti–quark[10] separated by distance r is given in Equation 1.1:

$$V(r) = \frac{A(r)}{r} + Kr. \tag{1.1}$$

The first term in Eqn. 1.1 resembles the Coulomb potential (in that it has a $1/r$ dependence), but A has a dependence on distance, and is proportional to α_s, the strong coupling constant. The strong coupling constant is analogous to the QED fine structure constant ($\alpha = \frac{1}{137}$). However, the value of α_s varies depending on the momentum transferred (Q^2) between the quark and gluon in the hadron. Figure 1.1 illustrates this, showing various values for α_s for different Q^2 values in both experimental data (points) and theory (curves)[11].

For large momentum transfers (large Q^2) or at small distances (small r), α_s decreases (see Figure 1.1) corresponding to a weakening of the force as quarks are squeezed together. For very small separations the quarks behave as though they were free. This QCD phenomenon is called "asymptotic freedom." The small value of the strong coupling constant in these situations makes possible the application of perturbative calculations, and thus a check of the QCD theory.

It is the second term in the potential that gives QCD its unique properties. As distances become large, this second term dominates, and the potential grows with increasing separation between the quarks. This separation condenses the field lines of the force into a narrow flux tube between the quarks. Figure 1.2 illustrates the increasing potential, and the flux tubes at the point where the distance between the two quarks has grown large enough that the potential equals the mass of a quark–antiquark pair. At that point, it is

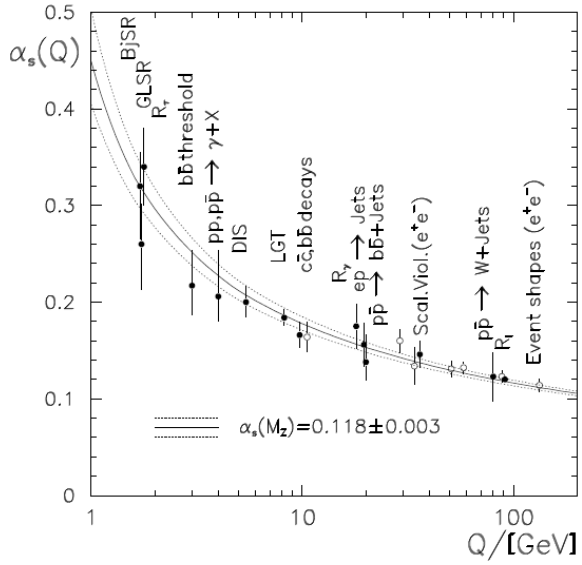

Figure 1.1: Running of the strong coupling constant as measured by several different experiments and compared to the QCD prediction[11].
.

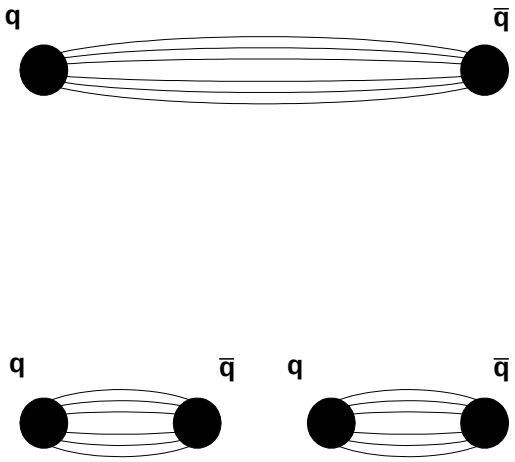

Figure 1.2: Schematic illustrating the flux lines between a quark–antiquark pair (top), and the formation of a new pair (bottom) as the distance between the original becomes large enough.

energetically more efficient to create a second quark–antiquark pair, rather than continuing to allow the potential to grow. This behavior is called "confinement," and is the reason why it is impossible to observe a single quark, only color–neutral new particles emerge which are visible to us in detectors.

Inside hadrons, the momentum exchanged between quarks and gluons is small and α is large, and the perturbative techniques used in QED cannot be employed to describe QCD phenomena. Several "bag models" have been developed (for example the MIT Bag Model [12]). In such models the hadron is treated as a bag of finite temperature and the quarks are massless inside. Outside the bag, the quarks are given an infinite mass. Confinement arises from a balance between the outward pressure due to the quarks' kinetic energy and an inward pressure due to the bag. If this balance is tipped such that the kinetic energy of the quarks becomes larger than the bag pressure, deconfined quarks and gluons are the result. This deconfined state represents a new phase of nuclear matter, the Quark Gluon Plasma (QGP).

1.1.1 QCD Phase Diagram

Figure 1.3 shows a schematic picture of the phase diagram for nuclear matter. It illustrates the different phases of nuclear matter, as temperature and baryon density change. The horizontal axis represents baryon chemical potential (μ_B), a measure of baryon density of the system. μ_B can be thought of as the energetic "cost" of producing a particle (baryon). The vertical axis represents the temperature of the system.

The region at low (near zero) μ_B and very high T resembles the conditions moments after the Big Bang. The temperature and density of the Universe was so large that baryons could not form. As the Universe expanded it cooled, which allowed hadronization of the quarks to occur, and matter transitioned from the QGP phase to the hadron gas phase. The region at high μ_B and low T resemble the conditions near the center of neutron stars[2]. These objects are extremely compact remnants of the gravitational collapse and subsequent explosion (supernovae) of very massive stars.

In Figure 1.3, the solid curve is the first order phase transition between the hadron gas phase and the quark gluon plasma phase; the dashed portion to the left of the critical point represents the region where a smooth, fast, cross–over between the two phases is expected. The quark gluon phase is the high temperature deconfined nuclear matter predicted

[2]Low temperature compared to the QGP phase of the early Universe. Internal temperatures of neutron stars are extremely hot relative to our everyday experience

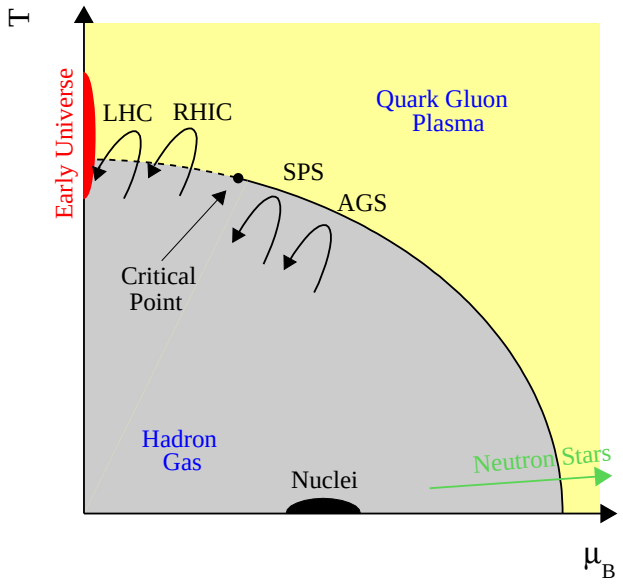

Figure 1.3: Schematic phase diagram of nuclear matter. The solid line represents the phase transition between normal hadronic matter and the quark gluon plasma, and the dashed line an expected first–order cross over region. Also on the diagram (curved arrows) are the regions thought to be probed at RHIC and other accelerators by heavy ion collisions.

by theory. As this matter expands it cools, and when a critical temperature (T_C) is reached, hadonization into mesons and baryons occurs[3]. It is these particles which can be detected experimentally. Lastly, the curved arrows show the region of the phase diagram that RHIC (and other colliders) is thought to probe. In heavy ion collisions at RHIC, hadronic matter is heated through the phase boundry into the quark gluon plasma state. Theoretical models along with information of the temperature and chemical potential at the freeze–out stages narrow down the phase boundary crossing point on the phase diagram [23].

1.2 Ultra Relativistic Heavy Ion Collisions

Heavy ion collisions are an ideal tool to probe the several interesting areas of the QCD phase diagram, and experiments at BNL and CERN have provided many results that have advanced the understanding in the field over the past four decades [15]. In the mid

[3] T_C is predicted from lattice QCD [13], and can be estimated experimentally from the relative abundances of particle species.

1980's the AGS led the way by colliding "light" nuclei such as sulfur, oxygen and silicon before moving to "heavy" ion research with gold–gold collisions in the beam energy range of $\sqrt{s_{NN}} = 2\,\text{GeV/nucleon}$ to $10\,\text{GeV/nucleon}$. These fixed target experiments were among the first ion collisions studied. At CERN, the SPS ran with the light ions at $200\,\text{GeV/nucleon}$ and at $158\,\text{GeV/nucleon}$ with beams of lead. The lead collisions were also studied at energies as low as $\sqrt{s_{NN}} = 20\,\text{GeV/nucleon}$ as efforts were made to map the QCD phase diagram, in the hopes of finding the critical point (see Figure 1.3). These studies did not find evidence of deconfinement or the QGP.

Efforts then turned to higher energies, and to colliding beam experiments. Two colliding beams of particles can impart more energy into the colliding system as a lone beam and a stationary target. As mentioned previously, RHIC was built for this purpose, and has collided gold and copper ions over a broad range of energies, from $\sqrt{s} = 7.7\,\text{GeV/nucleon}$ to $100\,\text{GeV/nucleon}$ in Au+Au and from $\sqrt{s} = 11\,\text{GeV/nucleon}$ to $100\,\text{GeV/nucleon}$ in Cu+Cu (see Table C.1 in the appendix). In the past two years, the Large Hadron Collider (LHC) at CERN has begun [22] colliding beams of lead nuclei at even higher energies than RHIC, further pushing the limits on heavy ion research. The LHC has collided lead ions up to an energy of $\sqrt{s} = 2.8$ TeV/nucleon and has the capability to go to even higher energies.

The remainder of this section will present and describe definitions of terms associated with heavy ion collision research. Figure 1.4 will be referred to for some items below.

Centrality Centrality is an important property of collisions, used to classify how "violent" the collisions are. It is a measure of the overlap of the two colliding particles (ions), and its value affects the resulting medium. Collision centrality ranges from peripheral (a glancing blow) to fully overlapped (a head–on collision). Centrality and how it is determined will be discussed in the next section.

Impact Parameter The impact parameter (b in Fig. 1.4) of a heavy ion collision is the distance separating the two nuclei's centers. This varies from collision to collision and cannot be controlled by the RHIC machine, or measured by PHENIX directly. b is small for central collisions, and large for peripheral collisions.

N_{part}, the Number of Participating Nucleons The right side of Figure 1.4 shows the collision along the line of travel for one ion, i.e. along the beam direction. The nucleons

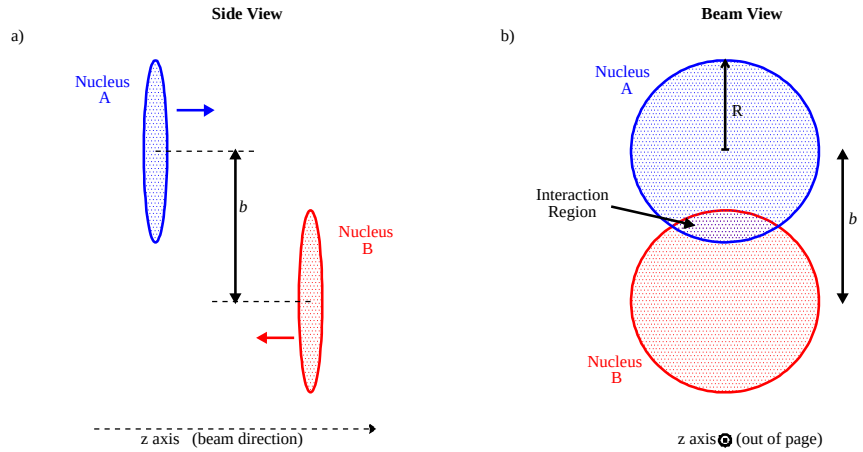

Figure 1.4: Schematic illustration of a collision between two nuclei of typical radius R and separated by impact parameter b. The side view (where beams traverse along the page) is shown in (a) and the beam view (where the beams travel perpendicular to the page) is shown in (b).

within the overlap region are those that participate in the collision; the number of interacting nucleons is $N_{\rm part}$. As this is a geometric quantity, $N_{\rm part}$ depends only weakly on the collision energy. $N_{\rm part}$ is maximal for head–on collisions.

$N_{\rm coll}$, the Number of Collisions $N_{\rm coll}$ is a measure of the total number of binary collisions all (individual) nucleons suffer in the whole of the ion–ion collision. If the number of participating nucleons is small (a very peripheral collision), $N_{\rm coll}$ is roughly equal to $N_{\rm part}-1$. For more central collisions $N_{\rm coll}$ has a power law dependence on $N_{\rm part}$. That is, the more nucleons participating, the larger the number available to hit. $N_{\rm coll}$ is strongly dependent on collision energy (nucleon–nucleon cross–section), and on the model(s) employed to calculate it.

Spectator Nucleons In Figure 1.4, the nucleons not in the almond shape overlap region are considered spectators. These are not involved in the heavy ion collision and continue with their momentum along the beam direction after the collision. The total number of spectators is $N_{\rm spec} = 2A - N_{\rm part}$

1.2.1 Centrality

A nuclear collision is considered "central" if the impact parameter b is small and "peripheral" if b is large [16]. The questions arises, however, as to the degree of "central" and "peripheral", as b could be any value between 0 and the diameter of the nucleus[4]. Common convention is to separate centrality into percentages, with 0% central describing a collision with $b = 0$ and 100% central to be the most peripheral collisions.

The method used to calculate centrality employs the Glauber Model [14]. The Glauber Model uses a Monte–Carlo framework to describe the geometry of nuclei and provides a value to each parameter (b, N_{part}, N_{coll}) to classify the nuclear collisions. The charge density ($\rho(r)$) of a nucleus is described by a Woods–Saxon distribution:

$$\rho(r) = \frac{\rho_0}{1 + e^{-\frac{R-r}{d}}}. \tag{1.2}$$

The constant, ρ_0, is the charge density of the nucleus, defined by the number of protons, R is the nuclear radius and d the skin thickness. This skin thickness is related to the nuclear surface thickness, which is the radial distance over which the probability of finding a nucleon in the nucleus changes from 90% to 10% [24] (as seen in figure 1.5) .

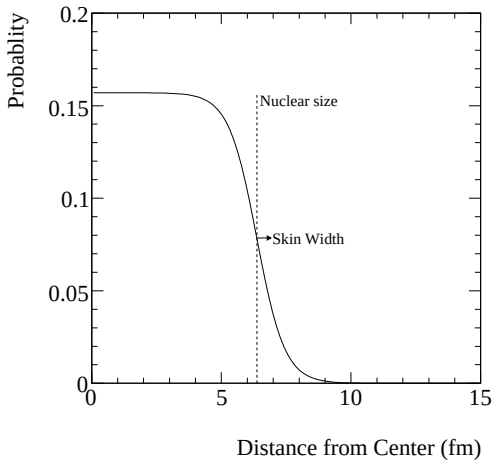

Figure 1.5: Woods–Saxon distribution for the probability of finding a nucleon in a gold nucleus. The integral of this distribution is normalized to one when given as a probability.

The probability of finding a nucleon at some radius r is given in Equation 1.3,

[4]The nuclear wave function actually extends to ∞ and ultra peripheral collisions, with impact parameter larger than the radius of the nucleus, are observed.

where the r^2 dependence allows for a uniform density in 3–dimensions.

$$P(r) = \frac{Ar^2}{1 + e^{-\frac{R-r}{d}}} \tag{1.3}$$

1.2.2 Nucleon–Nucleon Reactions

In order to fully understand the results of heavy ion collisions, an understanding of the more simple proton–proton (pp) reaction is needed. At a center–of–mass energy of 100 GeV the total pp cross section ($\sigma^{pp}_{total} = \sigma^{pp}_{elastic} + \sigma^{pp}_{inelastic}$) involves mostly inelastic processes[5], and the colliding particles lose energy which goes into particle production. The average number of particles produced (of which most are charged and neutral pions) will increase with increased center–of–mass energy. Most of the produced particles have small transverse momenta (p_T), the component of the momentum perpendicular to the beam axis.

1.2.2.1 Soft Process

Figure 1.6 shows particle production in pp collisions at different energies from different experiments at CERN. In the low momentum range ($0< p_T < 2$ GeV/c) the spectra have a shape described by an exponential ($e^{-\alpha p_T}$), also in the figure as the steepest line. In this low p_T region, production is dominated by soft processes. Soft processes are low Q^2, low momentum transfer processes, which cannot be described by perturbative QCD. Instead, phenomenological models are employed to describe the bulk of produced particles by soft processes.

1.2.2.2 Hard Processes

The exponential shape in Figure 1.6 fails to describe the data as p_T increases, as can be seen by the second line on the figure. As p_T increases the points move away from the exponential shape. In this second region (p_T larger than ~ 2 GeV/c) the spectra is best described by a power law. Here the particle production is resultant from large Q^2 processes, or hard processes. Inelastic hard scattering of protons is described in the pertabative techniques of QCD as the scattering of point–like partons (quarks and gluons) inside the nucleus. This results in jets of particles streaming out of the reaction in the same direction as, and following, the lead of the scattered parton. The time scale of hard

[5] At 200 GeV the inelastic cross section for pp collisions is 42 mb while the total cross section is ≈ 50 mb.

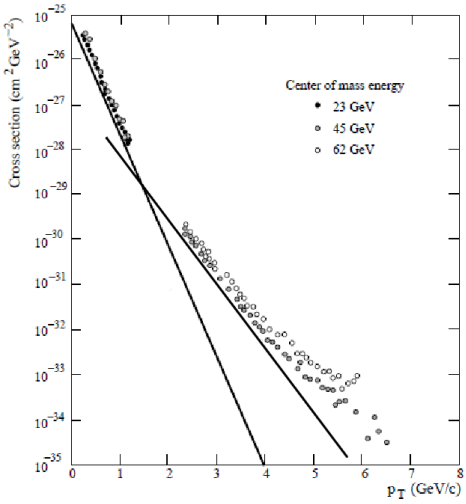

Figure 1.6: Neutral pion production at different center–of–mass energies in pp collisions at CERN [25]. Production at lower p_T due to soft processes produce yields that have an exponential shape while production at higher p_T follow a power law. The two lines illustrate the different spectral shapes.

processes is short compared to that of soft processes, and are thought to occur prior to the formation of the Quark Gluon Plasma.

1.3 The Quark Gluon Plasma

In an ultra relativistic heavy ion collision, each nucleus can be thought of as a collection of independent nucleons, and as mentioned above, only those nucleons within the range of the impact parameter are involved in the collision (N_{part}), the rest are spectators. Those that do collide form a fireball, the region of extreme heat and density unique to heavy ion collisions.

The space–time evolution of a heavy ion collision is illustrated in Figure 1.7. The two nuclei approach each other at close to the speed of light and collide. After the first few initial interactions, the reaction zone is filled with very excited matter, which is not in thermal equilibrium. Upon thermalization, a quark gluon plasma is formed and it is at this time that partons can interact with one another. Deconfinement is achieved. As the system begins to expand into the vacuum, temperatures begin to lower, and a less excited medium exists. Quarks and antiquarks begin to form hadrons and a possible mixed state of hadron gas and QGP coexist before the final stage of the reaction, when the hadron gas expands

further and particle types and momentum freeze–out.

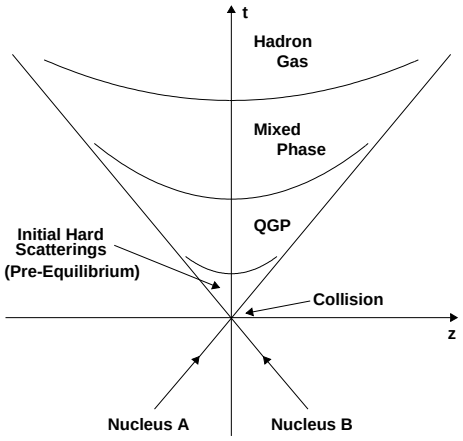

Figure 1.7: The space–time evolution of a heavy ion collision of nucleus A and B. At early time (t) the initial scattering prevents equilibrium. As the system settles, a quark–gluon plasma forms and equilibrium is established. The nuclear matter then moves through a phase containing a mix of QGP and hadron gas as the system cools. Further expansion results in hadronic freeze–out.

1.3.1 Parton Energy Loss and the Nuclear Modification Factor R_{AB}

Particles with large p_T are produced in hard parton scattering, as discussed above. In a *pp* collision, these particles fragment directly in the vacuum, and are seen as jets, back–to–back streams of particles created from the fragmentation of the two initially scattered partons (see Section 1.1 and Fig. 1.2). In heavy ion collisions the situation is different. The hard scattering occurs in the initial moments of the collision (see Figure 1.7), and the scattered partons now may have to traverse the newly created hot, dense medium before they fragment into hadrons. As a result of the scattered partons now interacting with the medium (and hence losing energy), a large energy loss was predicted [26]. Also, the back–to–back correlation of jets of particles seen in *pp* interactions are expected to be distorted [27]. That is, one of the particles leading to a jet may be near the surface of the created medium, and have little or no medium to transverse, and so will not lose much energy, but the other will. Therefore only one jet of particles may be observed in the detectors. This phenomenon is called jet quenching and leads to a suppression of particle production in heavy ion collisions compared to that in *pp* collisions.

1.3.1.1 Nuclear Modification Factor, R_{AB}

As in pp collisions, the large momentum transfer of the initial hard scattering means the partons can be considered to be free. The cross section in a collision of two nuclei $A + B$ should then be related to the pp cross section. The two are connected by the scaling factor N_{coll}, the number of inelastic binary nucleon–nucleon collisions expected in the reaction. For heavy ion collisions at a fixed centrality (fixed impact parameter b) involving nuclei $A + B$, N_{coll} is proportional to the nuclear thickness function $T_{AB}(b)$, see Equation 1.4 for a certain centrality bin.

$$\langle T_{AB} \rangle_{Cen} = \frac{\langle N_{\text{coll}} \rangle_{Cen}}{\sigma_{NN}} \tag{1.4}$$

The thickness function can be thought of as a measure of how many nucleons are "stacked" in the flat nucleus[6]. Figure 1.8 illustrates the singular T_A for a nucleus A. The nucleons which make up the nucleus in the rest frame become stacked on top of one another in the lab frame when the ion is accelerated to relativistic speeds.

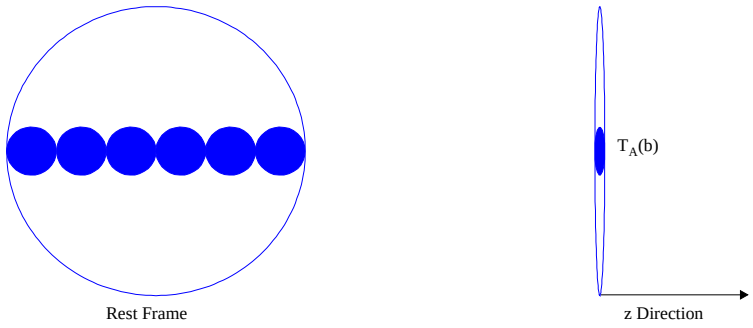

Figure 1.8: Schematic diagram illustrating $T_A(b)$. The left side shows a nucleus in its rest frame, with 6 nucleons inside. The right side shows the same nucleus in the lab frame (relativity accelerated). Here the same 6 nucleons are now stacked on top of one another due to Lorentz contraction.

Equation 1.5 shows the expected hadronic cross–section (h) in the collision of two ions (A and B). As the mean impact parameter changes as a function of centrality, so

[6] As the nuclei are moving at relativistic speed, they are Lorentz–contracted in the lab frame into two dimensions perpendicular to the direction of travel.

too does the average nuclear thickness function, $\langle T_{AB} \rangle$, labeled Cen for a given centrality. This thickness, scaled by the measured cross–section in pp collisions yields the expected cross–section in heavy ion collisions.

$$\frac{d^2N^h_{AB}}{dp_T dy}\Big|_{Cen} = \langle T_{AB} \rangle_{Cen} \cdot \frac{d^2\sigma^h_{pp}}{dp_T dy} \tag{1.5}$$

The scaling of particle production with the number of binary collisions described by Equation 1.5 can be modified when the energy of the hard scattered partons is modified; for example, when the partons lose energy (within the created nuclear medium) before fragmentation. This modification is studied with the nuclear modification factor R_{AB}:

$$\begin{aligned} R_{AB} &= \frac{1}{\langle T_{AB} \rangle_{Cen}} \cdot \frac{dN^h_{AB}}{d\sigma^h_{NN}} \\ &= \frac{1}{\langle N_{\rm Coll} \rangle_{Cen}} \cdot \frac{dN^h_{AB}}{dN^h_{NN}} \end{aligned} \tag{1.6}$$

where $\langle N_{\rm coll} \rangle_{Cen}$ is the average number of inelastic binary nucleon–nucleon collisions, having the inelastic cross section σ_{NN}. $\langle N_{\rm coll} \rangle_{Cen}$ and the average nuclear thickness function is calculated via a Monte Carlo calculation taking into account centrality range selections and is detailed in [28, 30]. R_{AB} is unity in the absence of any medium effects.

One of the presumed signatures of the quark gluon plasma is the suppression of hadron production. As partons lose energy to the medium before they hadronize, the resultant hadron yields will be smaller compared to that expected from a superposition of independent pp collisions. This will give $R_{AA} < 1$[7]. A nuclear modification factor less than unity is a signal for the formation of a quark gluon plasma.

1.4 Photon Production

Direct photons are used as a tool to study the different stages of ultra relativistic heavy ion collisions, and the formation and thermalization of the quark gluon plasma in particular. Because direct photons are not influenced or affected by the strong interaction or the hadronization process, they provide a unique probe of the nuclear matter created in heavy ion collision.

[7]The generic R_{AB} is often replaced with R_{AA} when the colliding species are the same. In the case of this Thesis, Cu+Cu collisions are studied and the colliding ions are indeed the same (copper)

The term "direct photon" denotes those photons which do not originate from a hadronic decay (for example $\pi^0 \rightarrow \gamma\gamma$ or $\eta \rightarrow \gamma\gamma$). Direct photons can be further classified into two categories, prompt photons and thermal photons. Prompt photons are those photons which originate from the initial hard scatterings of the heavy ion collision, while thermal photons come from a thermally equilibrated phase, either the quark–gluon plasma phase or hadron phase. Although prompt and thermal photons cannot be separated experimentally, it is expected that the thermal photon signal is largest at intermediate transverse momenta (1 GeV/c< p_T < 2 GeV/c), and prompt photons dominate the direct photons at larger p_T.

1.4.1 Prompt Photons

As stated above, prompt photons originate from early in the collision process, from the initial hard scattering of partons. To the first order, there are three mechanisms that can produce these photons. Figure 1.9 shows the Feynman diagrams of the processes: Compton scattering of quarks and gluons, quark–antiquark annihilation, and Bremsstrahlung[8]. The first process occurs when a fast quark passing through the interaction region scatters off a gluon in the region, producing a photon. In the second process a quark and antiquark annihilate to produce the photon. The third process, Bremsstrahlung, is the process by which a charged particle emits a photon as it loses energy when traveling near another charged particle. In this early stage of a heavy ion collision, the quarks radiate Bremsstrahlung as they move past one another.

1.4.2 Thermal Photons

The second contribution to the direct photon signal are thermal photons. This type of thermal radiation will dominate the signal in the lower p_T region (around $p_T \simeq$ 1–2 GeV/c). Radiation of this type emanates from an equilibrated system, the quark–gluon plasma or the hadron gas phase of the heavy ion collision reaction. Figure 1.10 shows illustrates examples of processes generating thermal photons from the quark–gluon plasma or from the hadron gas phase of heavy ion collisions. The left panel illustrates Compton scattering of a charged pion and a meson. The middle is pion annihilation ($\pi^+\pi^- \rightarrow \rho^0\gamma$), and the diagram for ρ^0 decay is on the right.

[8]Literally "breaking radiation" in German.

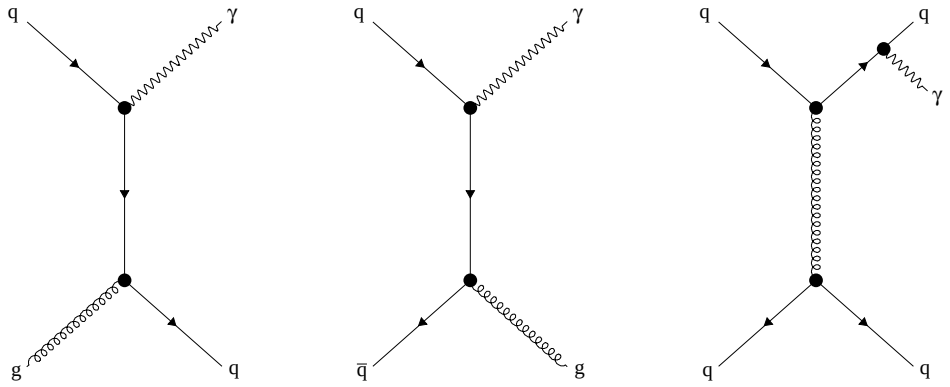

Figure 1.9: Feynman diagrams of direct photon production due to quark and gluon interaction in the early stage of heavy ion collisions. On the left is the Compton scattering of a quark and gluon, the middle panel shows $q\bar{q}$ annihilation. The right most diagram illustrates a Bremsstrahlung radiated photon (γ).

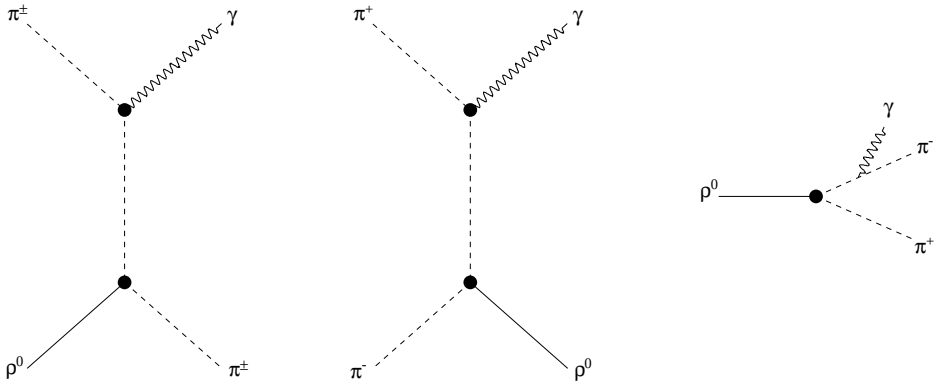

Figure 1.10: Example processes of thermal photon production. On the left is Compton scattering of a charged pion and a rho meson($\pi^{\pm}\rho^0 \to \pi^{\pm}\gamma$). The middle panel shows pion annihilation ($\pi^+\pi^- \to \rho^0\gamma$), and the decay of a ρ meson on the right.

Chapter 2

RHIC and The PHENIX Experiment

Brookhaven National Laboratory (BNL) has a long history of pioneering particle accelerators. In the 1950's and 1960's the cosmotron first observed neutral decay particles [42], followed by the AGS (Alternating Gradient Synchrotron), and later the Relativistic Heavy Ion Collider (RHIC). Figure 2.1 shows a schematic layout of the RHIC complex, including the AGS, boosters, and Tandem van de Graaffs.

2.1 RHIC

The Relativistic Heavy Ion Collider was first proposed in the early 1980s and produced its first collisions in 1999. Originally there were four experiments at RHIC. The data used in the analysis presented here was collected with the PHENIX detector, to be discussed in more detail in the following section.

RHIC[17] can accelerate and collide protons and/or ions over a large range of energies and particle species, making RHIC a versatile and adaptive machine with which to study nuclear and particle physics. Table C.1 in the appendix lists the collision species and corresponding collision energy at RHIC over the first 11 years of operation. Also listed is the RHIC run number and machine luminosity. In the largest scale, RHIC was built for two goals: to study the spin of the proton and to discover and study the QGP. For the study of the origin of the spin of the proton, RHIC collides polarized protons, up to a maximum center–of–mass energy of 500 GeV (250 GeV per proton), with an expected

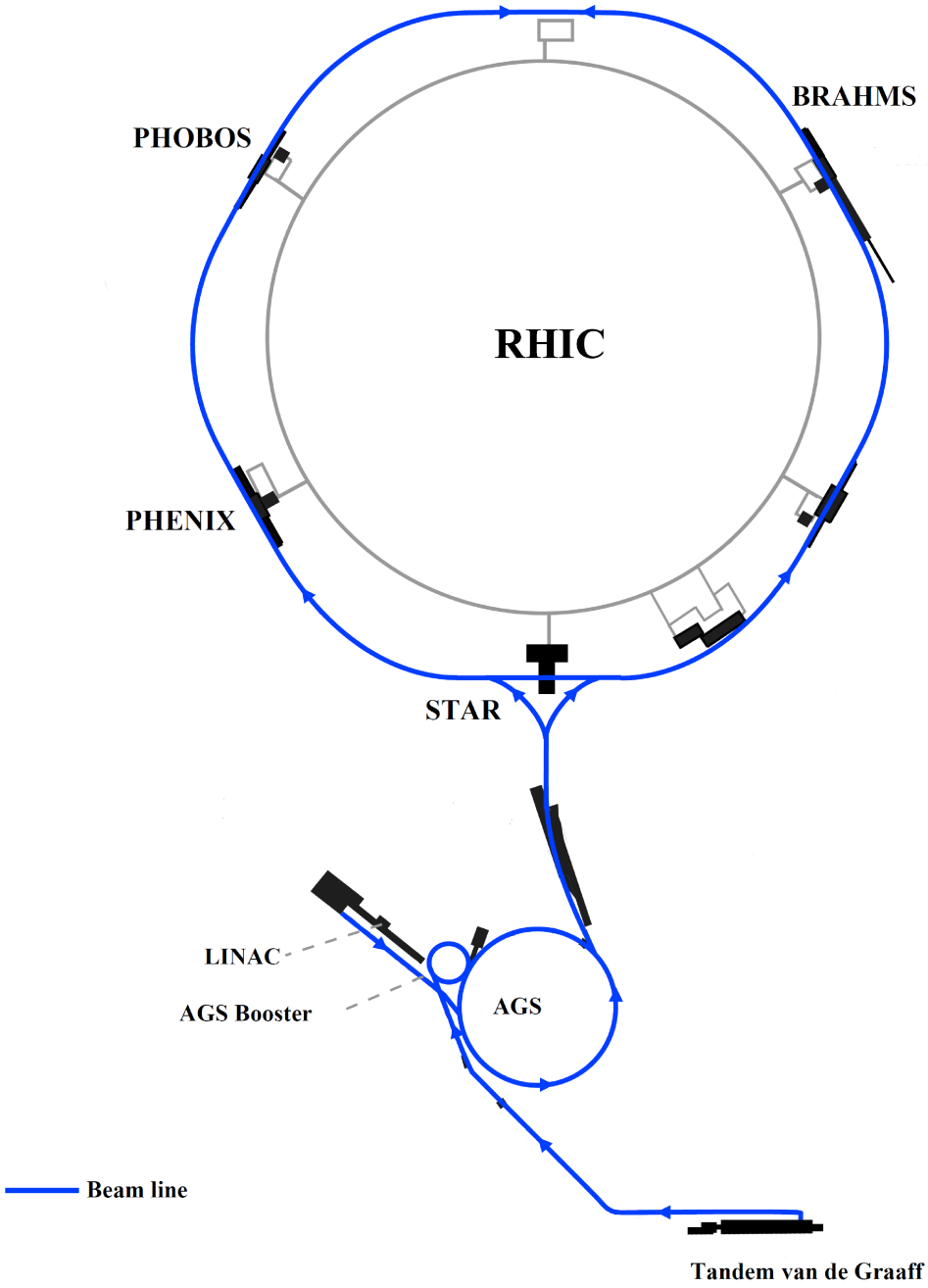

Figure 2.1: Schematic of the RHIC complex, including the original four experiments. The arrows show the direction of travel for heavy ions as they are accelerated. [39]

maximum luminosity of 2×10^{32} cm^{-2}s^{-1}.

In studying the QGP, and of primary interest for this work, RHIC collides ions to study nuclear matter at extreme temperature and density. Heavy ions are accelerated up to the maximum center–of–mass energy of 200 GeV (100 GeV per nucleon) with a luminosity of 2×10^{26} cm^{-2}s^{-1}.

The ions themselves originate from a Vacuum Arc Ion Source [1] [41] and are then alternately accelerated and stripped of electrons as they move through the Tandem Van De Graaffs. The ions are passed through carbon stripper foils to remove electrons until they reach the +31 or +32 (for Au+Au) electric charge state. The ions are then passed to the AGS booster where they are further accelerated and stripped, then passed to the AGS itself. After the ions are accelerated to the maximum AGS energy (9.8 GeV for Au nuclei) the last few electrons are stripped and the ions are injected into the two counter circling RHIC rings. Denoted yellow and blue, the two rings lie on top of each other in the RHIC tunnel. Once there, the ions are brought up to the desired collision energy.

2.1.1 Experiments

PHOBOS[18], one of the smaller experiments on the RHIC ring, was named after one of the moons of the planet Mars[2]. The PHOBOS detector was located at 10 o'clock on the RHIC ring and the PHOBOS collaboration was the first RHIC experiment to publish results. PHOBOS was a collection of silicon pad detectors, with a broad pseudorapidity coverage ($|\eta| < 5.4$), and a spectrometer with small acceptance but high resolution. This large range of acceptances made the detector ideal to study the number of particles, or multiplicity, from RHIC collisions. PHOBOS went offline in 2005, after RHIC run 5.

The other smaller experiment was BRAHMS[19] (*B*road *RA*nge *H*adron *M*agnetic *S*pecrtometers). BRAHMS (2 o'clock on RHIC), had two movable spectrometer arms that allowed placements in the ranges of $2.3^\circ \leq \vartheta_1 \leq 90.0^\circ$ and $30.0^\circ \leq \vartheta_2 \leq 95.0^\circ$. Like PHOBOS, this gave BRAHMS a broad range in rapidity. BRAHMS went offline after RHIC's run 6 in 2006.

STAR[20] (*S*olenoidal *T*racker *A*t *R*HIC) is a larger general purpose detector. The main component, the time projection chamber (TPC) weighs approximately 1200 pounds

[1] The ions are first stripped from a foil with a large electrical arc, and are then extracted with electric fields forming an ion beam.

[2] The original name was to be "Modular Array for RHIC Spectra", or MARS. However after budget issues forced some downsizing, the name was changed.

and has a radius of 2 meters. Covering the pseudo–rapidity range of $|\eta| \leq 1$, the cylindrical TPC is well suited to track the many thousands of particles produced at mid–rapidity in heavy ion collisions at RHIC. Along with PHENIX, STAR continues to collect and analyze data. This detector sits at 6 o'clock on the ring.

2.2 PHENIX

The PHENIX collaboration and experiment[21] has a historical background that provided the detector with a unique make–up, and its name. During the planning and design stage of RHIC, several groups of scientists were vying for the limited number of spaces for detector experiments on the RHIC ring. Three such groups were interested in the same topic of studying rare probes to examine the quark–gluon plasma. In particular, these groups wanted to study probes that were produced early in the collisions, or wanted to study electromagnetic probes that would not be affected by the strongly interacting matter; hadrons, photons, electrons, and muons. Since all three groups had similar proposals, all three were rejected and the groups were told to consolidate their ideas into a single proposal. Thus, PHENIX "rose from the ashes" and the result was a very versatile PHENIX detector with the ability to investigate many different types of physics. The name "Pioneering High Energy Nuclear Interaction eXperiment" was given after the acronym PHENIX[3] was decided upon.

The detector, all its subsystems and magnets, is quite large, the largest at RHIC. PHENIX weighs 4000 tons, and as of this writing has 16 sub–systems. The ones used in this Thesis will be highlighted here.

2.2.1 Beam–Beam Counters

Two of the most important subsystems are the Beam–Beam Counters and Zero Degree Calorimeters, BBC and ZDC respectively. These are used to trigger read–out of all sub–systems, locate the collision vertex, determine the collision centrality, and more. Both the BBC and the ZDC are physically small detectors and are designed to give fast read–out to PHENIX triggers. They each have a North and South section, and each operates as a particle counter. The number of particles hitting each detector is determined by the amount and location of energy deposited in the detectors. The fine timing resolution, 50 ps for the

[3]The missing "O" in PHENIX appears in the official logo as a burst of particles with an austere phoenix perched on top.

BBC and 100 ps for the ZDC, allows each to determine the collision vertex via the time difference of particles hitting the North versus South side. The following examines other properties of the BBC and ZDC.

The two sets of beam–beam counters provide information for four vital measurements:

- Timing information for collisions used in time of flight (ToF) measurements
- Signaling the PHENIX triggers
- Measuring the collision vertex point
- Calculating collision centrality

Figure 2.2 shows the placement of the BBCs within PHENIX. In the pseudorapidity range $3 < |\eta| < 4$, both the North and South sections are a collection of phototubes and each phototube has a corresponding Cherenkov–radiating quartz in front of it. As the BBC is sensitive to all charged particles, independent of momentum, these detectors are ideally suited to detect particles produced in the collision and serve as an efficient trigger. As these particles are predominantly low momentum, the signal recorded is dependent on the number of nucleons involved in the collision, N_{part}, which is ideal for determining the centrality of the collision. Finally, the BBC timing is used by all other PHENIX subsystems as the signal for the start time of an event.

2.2.2 Zero Degree Calorimeter

Figure 2.2 also shows the location of the ZDCs. The "Zero Degree Calorimeters" sits very forward in η, at "zero degrees" behind the dipoles magnets, which steer the beam into collisions at PHENIX. At the same time, those magnets also bend charged particles away from the ZDCs, such that the ZDC only detects neutral particles. Because of its very forward position, these particles are typically neutrons not involved in the collision, the spectator particles, N_{spec}. Since the BBCs are sensitive to N_{part} and the ZDCs to N_{spec}, the energy in the ZDC should be large when the charge in the BBC is small, and vice–versa. Figure 2.3 illustrates this with measured ZDC energy correlated against the BBC charge in Cu+Cu collisions (at $\sqrt{s} = 62.4$ GeV).

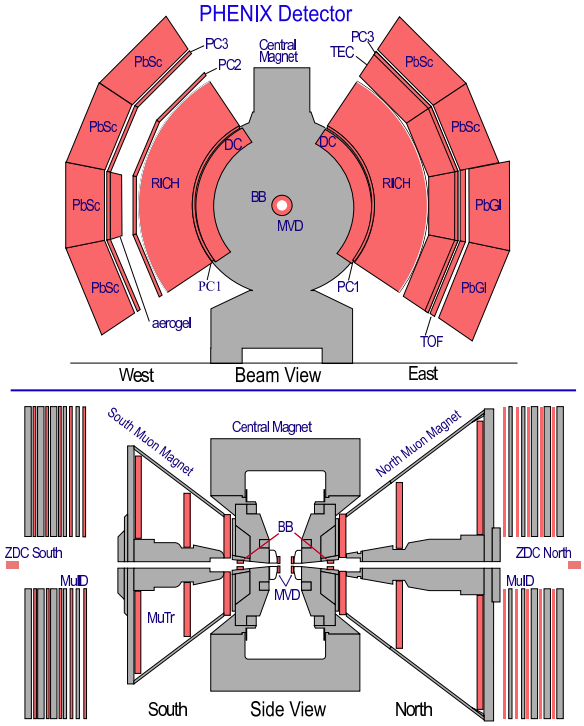

Figure 2.2: Top: Beam line view of PHENIX. The EMCal sectors are located on the outside of the East and West arms (PbSc and PbGl on the East, PbSc only on the West. Bottom: Side view of PHENIX, showing the locations of the BBCs (labeled "BB"), and the ZDCs.

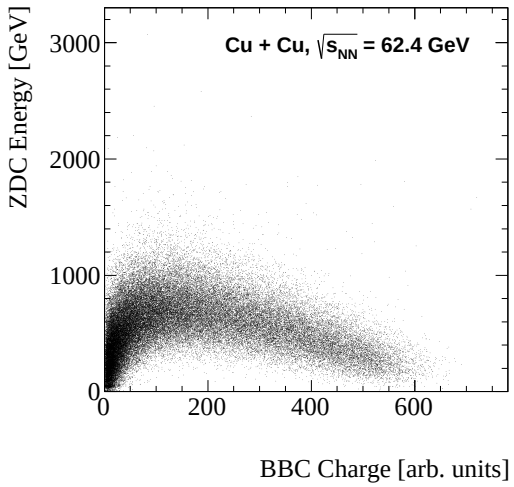

Figure 2.3: The correlation between ZDC energy and BBC charge in Cu+Cu at $\sqrt{s} = 62.4$ GeV. The large BBC signal observed at low ZDC energy recorded illustrates the correlation between the two detectors.

2.2.3 Electromagnetic Calorimeter

The PHENIX electromagnetic calorimeter (EMCal) consists of two types of calorimeter which form two independent subsystems. As a result, these subsystems produce two completely independent measurements. The EMCal itself is divided into eight sectors, four sectors per detector arm (East and West). The face of each sector is five meters from the beam axis, and each is made up of several modules. Groups of modules combine into supermodules, although the number and type of these differ in the two subsystems. The largest area subsystem is a lead–scintillator (PbSc) electromagnetic calorimeter, which occupies 6 of the 8 sectors. The remaining two sectors are constructed of lead–glass. The EMCal covers the transverse area $\Delta\eta = 0.35$ and $\Delta\phi = 2 \times 90°$ (2 arms of the detector). See Figure 2.2.

2.2.3.1 PbSc

The lead–scintillator portion of the EMCal is a sampling calorimeter as its construction allows only for a portion of the deposited energy to be measured. The PbSc [43] is comprised of alternating layers of lead absorber (passive medium) and plastic scintillator (active region) called towers. This "sandwich type" calorimeter has its towers of lead and scintillating material grouped into modules and supermodules.

A PbSc module (see Figure 2.4) is simply four towers grouped 2×2. The four towers are optically isolated from each other except at the center of the module, where an optical fiber sits and is used for calibration (see below). For ease of assembly and maintenance, a so called "supermodule" consisting of 36 of these modules are grouped together, and 18 of these comprise one PbSc sector. Light is read–out of the active regions using 36 wavelength shifting fibers and passed to photomultiplier tubes (PMTs) at the rear of the towers. Table 2.1 lists additional properties of the PHENIX PbSc.

Before installation the PbSc was calibrated with test beam electrons at known energies as well as with relativistic cosmic muons, and the detector's response to high–energy electromagnetic showers was studied [43]. During operation, monitoring and on–the–fly calibration is done using a high–powered ultraviolet laser [44]. Laser light is brought to the PbSc via a series of mirrors and splitters. At the detector, the light is delivered to each module by optical fibers. These fibers are grated (roughened) in such a manner that the light scatters to simulate a 1 GeV electromagnetic shower.

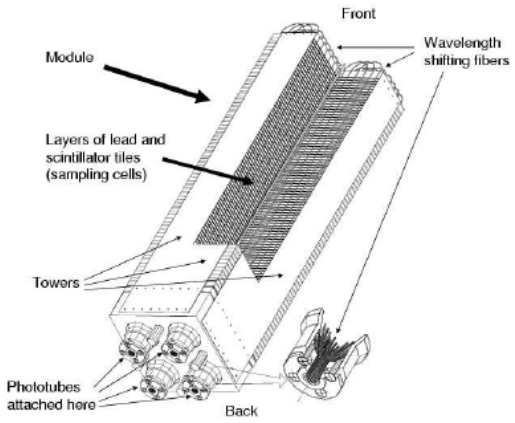

Figure 2.4: Schematic view of a PbSc module[43].

Parameter	Value
Active Cells	66
Scintillator	0.4 cm Polystyrene
Absorber	0.15 cm Pb
Active Depth	37.5 cm
Radiation Length	18 cm
WLS Fibers / Tower	36

Table 2.1: Properties of PHENIX PbSc towers

2.2.3.2 PbGl

Unlike the PbSc, the other EMCal sub–detector, the lead–glass calorimeter (PbGl), is a homogeneous detector. The material of the PbGl is a mixture of lead oxide (PbO) and silicon oxide (SiO_2) and is dense and transparent. Due to the high atomic number (high Z), of the lead–glass, it is a near perfect detector of electromagnetic showers. The high Z means showers evolve quickly and thus, despite its transparency, not an overwhelmingly large amount of the material is needed to fully measure the shower. The lead–glass blocks were previously used in the WA98 experiment[43] at CERN, and before their installation in PHENIX they were calibrated with a 10 GeV electron test beam at CERN.

Like the scintillator, the PbGl detector is segmented. The smallest unit, called a module, is 4 cm×4 cm×40 cm. A supermodule is 24 modules arranged 6×4, Figure 2.5 shows a schematic of a PbGl supermodule (SM). These supermodules allowed the PbGl to be easily reassembled in a different configuration than that of the CERN installation. A sector contains 192 supermodules. Each individual module is wrapped in aluminized mylar

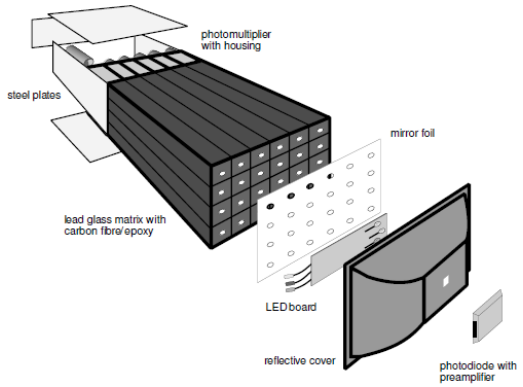

Figure 2.5: Schematic view of a PbGl supermodule.

Property	Value
Lead Oxide Content	51%
PbGl Density	3.86 g/cm^3
Radiation Length	2.8 cm
Interaction Length	38.0 cm
Moliere Radius	3.68 cm
Index of Refraction	1.648
Num. of SM per Sector	192
Num. of Modules per SM	24
Total Number of Modules	9216
Module Surface area	16 cm^2
Module Length	40 cm
Total Weight of PbGl	22,671.36 kg

Table 2.2: Properties of PHENIX PbGl detector

and a shrink tube to optically isolate them from each other. See table 2.2 for more about the properties of the PbGl detector.

A gain monitoring system comes with each PbGl supermodule [43]. This system contains three LEDs which each of the 24 modules in the SM can view. The first LED is an avalanche LED that mimics real electromagnetic showers. The other 2 LEDs have variable amplitudes and can mimic Cherenkov radiation. The light of the LEDs are monitored by a photodiode attached to back of the supermodule (see figure 2.5). This monitors light attenuation in the lead–glass.

2.2.3.3 Electromagnetic and Hadronic Showers

Electromagnetic Showers The primary method of interaction of high energy photons striking the PbGl is via electron–positron production (e^-e^+). Processes such as Compton scattering or the photoelectric effect give only a minor contribution. The produced e^-s and e^+s immediately begin radiating Bremsstrahlung, energy loss via photon radiation due to the electric fields of the atoms of the detector. These photons then produce electron–positron pairs and the process repeats. This is how an electromagnetic shower is formed, and the shower will continue until the energy of the produced particles falls beneath a critical energy, E_c. The distance an electron travels over which its energy decreases by a factor e is called the radiation length (X_0). The radiation length determines the probability that a photon converts into an e^-e^+ pair within the distance X:

$$p_{conv} = 1 - e^{-\frac{7}{9}\cdot\frac{X}{X_0}} \tag{2.1}$$

The depth that the shower descends into the detector depends on the energy of the initial particle, E_0, and can also be expressed in terms of the radiation length:

$$X_{max} \approx X_0 \cdot ln(\frac{E_0}{E_c}) + t \tag{2.2}$$

where t is (0.5) for photons and (-0.5) for electrons. The multiple scatterings of the particles as the shower progresses results in a "spread" or lateral extension of the shower. This extension is characterized by the Moliére Radius (R_M):

$$R_M \approx \frac{21\ \text{MeV} \cdot \text{X}_0}{E_c} \tag{2.3}$$

Hadronic Showers Another type of shower may form in the detector if a strongly interacting particle (for example a proton or charged pion) strikes it. Hadronic showers are characterized by the distance where 63% of the hadrons will suffer inelastic collisions and form new hadrons, usually pions, and begin showering. This distance, is the nuclear interaction length. Charged hadrons that do not form showers (do not suffer the inelastic reaction) deposit only a small amount of their energy in the detector are called "minimum ionizing particles" (MIPs). Their energy loss is constant over a wide range transversed in the material.

2.2.4 Pad Chamber

The Multi–Wire Proportional Chamber (MWPC), or Pad Chamber (PC), is a detector used to track charged particles. These type of detectors contain cathodes panels segmented on pads, and are permeated with anode wires [34]. The chamber between the cathodes is filled with an active gas. A charged particle passing through this volume of gas will produce ionization (resulting in freed electrons and positive ions) along its path of travel. The ionized electrons will move to the nearest anode wire causing avalanche to take place, while the gas ions induce a charge on the cathodes. A detailed discussion of MWPC detectors can be found in [10].

The PHENIX Pad Chamber is divided into three layers (PC1, PC2, and PC3, see Figure 2.2) and covers a total area of 88 m^2 [35]. Figure 2.6 shows a schematic of the PHENIX PC1. It provides space point locations along each charged track in the central arms. The electronics read–out for the PHENIX PC employ new techniques to handle the very high multiplicity environment of Au+Au collisions[34]. The analysis presented in this Thesis makes use of the PC3 layer of the Pad Chamber only. The PC3 lies directly in front of the EMCal, and provides an excellent tool for tagging charged particles as the impinge on the surface of the calorimeter. This is needed to remove charged particle contamination from the photon branch of the analysis (see Section 3.6.2.4).

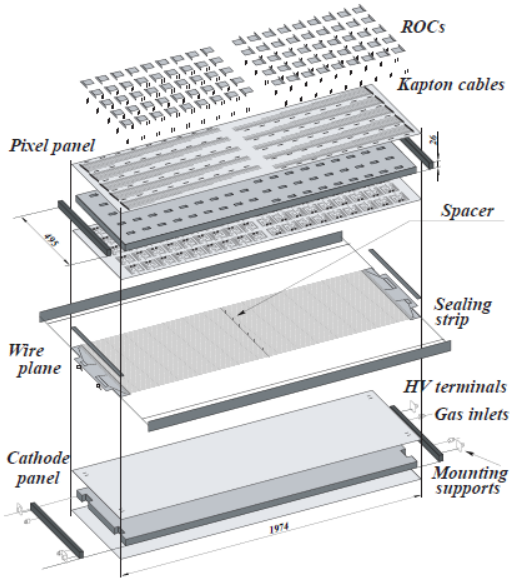

Figure 2.6: An expanded view of a chamber of the PC1, the PHENIX Pad Chamber [35].

Chapter 3

Analysis

The details of the analysis are presented in this chapter. The collision energy and species of the data set will be discussed as well as the criteria for selecting events and determining their collision centrality. Corrections applied to the data and the associated systematic uncertainties will be described.

3.1 Au+Au versus Cu+Cu Collisions

In planning for the fifth RHIC run, a good deal of Au+Au data had been analyzed, and hadron suppression had been confirmed [8, 45, 46, 47]. The natural question was: Where does this suppression turn–on? That is, is there some point where hot nuclear matter effects would be absent. For example, is there some smaller collision energy or some smaller collision species (or some combination of the two) where the quark–gluon plasma would not form? To help answer this question copper ions were collided at the center–of–mass energy of 62.4 GeV, as part of an energy scan in Cu+Cu collisions.

The size of the copper nucleus is much smaller compared to gold ($A^{Cu} = 63$ versus $A^{Au} = 197$), which means the maximum number of nucleons is less in that collision system. Results from 62.4 GeV Au+Au collisions exhibited suppression similar to that in the 200 GeV Au+Au collisions [32]. By colliding ions at a lower energy (62.4 GeV), the particle multiplicities are lower, and thus the energy density is reduced considerably. This allows one to probe in a detailed way the turn–on of the suppression effects seen in the heavier, more energetic systems. Measuring the same particle production properties in the Cu+Cu system is also very important. Hadron suppression is observed in peripheral Au+Au collisions [36], where $N_{\rm part} \sim 50$–100. Collisions of smaller copper ions (A = 63)

allows the study of this N_{part} range in a more controlled way and with reduced uncertainties in N_{coll}.

3.2 Event Selection

The data used for this analysis were collected in 2005 during RHIC's Run5. All data here are from Cu+Cu collisions at the center–of–mass energy 62.4 GeV. All events were recorded using the minimum bias trigger. In total, more than 126 million events were analyzed.

3.2.1 Minimum Bias Trigger

Inelastic collisions were accepted under the condition that at least one PMT in the North BBC and one in the South BBC fire (see Section 2.2). This minimum bias trigger condition is estimated to accept 88%±4% [30] of the total inelastic cross section for Cu+Cu collisions.

3.2.2 Centrality

The method to determine the centrality in PHENIX varies depending on the species and energies of data givien set. The centrality for this data set was calculated based on the charge in the BBC detectors. The impact parameter of the collisions is inversely proportional to the charge deposited in the BBCs. A Monte Carlo simulation is used to determine the proper correlation between the charge in these detectors and the corresponding number of participants in the collisions (N_{part}). A full GEANT discription of the PHENIX detector, PISA[1], is used to simulate the passage of particles through each subsystem. Using this software, the efficiency of the Beam–Beam Counters is calculated. A Glauber Model is then employed along with a Negative Binomial Distrubition (NBD), whose parameters are adjusted to fit the BBC charge distribution in the real data. The top panel in Figure 3.1 shows the data (blue) and the result of the NBD method (red). Note the inefficiency as the difference in the data at the BBC charge. The lower panel shows the ratio of $\frac{\text{real data}}{\text{NBD}}$.

Once the functional form of the BBC charge is obtained, the distribution can be divided into percentages, thus defining centrality classes. For this analysis, the data are

[1] PISA is "PHENIX Integrated Simulation Application".

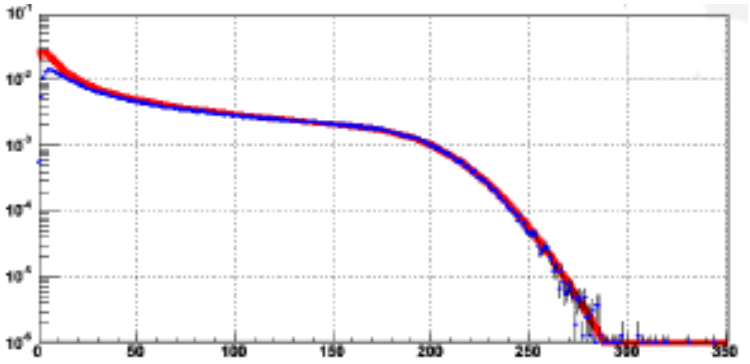

Figure 3.1: BBC charge distribution in the data (blue) and the result of the Glauber calculation employing the NBD method (red).

Label	Fractional Cross Section	N_{part}	N_{coll}
"Cc01"	60–88%	7.0 ± 0.7	5.5 ± 0.8
"Cc02"	50–60%	16.1 ± 0.9	15.0 ± 1.7
"Cc03"	40–50%	24.9 ± 1.5	26.2 ± 3.5
"Cc04"	30–40%	36.2 ± 1.8	42.6 ± 5.4
"Cc05"	20–30%	51.3 ± 2.0	67.8 ± 8.4
"Cc06"	10–20%	71.1 ± 2.4	105.5 ± 12.2
"Cc07"	0–10%	93.3 ± 2.6	152.3 ± 17.6
"Peri"	60–88%	7.0 ± 0.7	5.5 ± 0.8
"Midd"	30–60%	25.4 ± 1.6	27.5 ± 3.7
"Cent"	0–30%	71.8 ± 2.4	108.5 ± 12.9
"Minb"	0–88%	35.3 ± 1.8	47.9 ± 5.7

Table 3.1: Centrality classes used in this analysis, as determined from the BBC charge.

separated into seven centrality bins, three combined bins; and a Minimum Bias bin (all centralities included in one bin). See Table 3.1. As mentioned above, the final range (60–88%) does not reach 100%. This is due to the multiplicity of the Cu+Cu collisions, the number of created particles allows for, at most, 88% central collisions to be recorded, any more peripheral collisions might not produce enough particles to satisfy the mimimum bias condition (one PMT to fire in both the north and south BBC). The BBC fires on 88% ± 4% of the inelastic cross–section of Cu+Cu reactions at 62.4 GeV [30].

3.3 Dead and Warn Maps

Non–functional EMCal channels need to be accounted for and removed from the analysis. A map of all non–functioning channels is created using the data itself. Each individual module is flagged as non–functional if it consistently fires at a higher energy than surronding towers. Additionally, those modules which do not register any signal, or fire at a consistently lower energy than their neighbors, were marked. Figure 3.2 shows the bad module map for each sector of the EMCal. Here, the green areas denote good modules, white denote bad modules, and the dark (light) brown are the first (second) neighboring towers to the bad towers. In this analysis, only the bad towers (white) and their first–neighbor–towers (dark brown) were excluded as central or seed towers, allowing fully operational 3×3 sections without energy loss due to non–functioning modules. Similarly, all edge towers were considered as first neighbors, and thus also excluded as seed towers, to prevent energy loss at the edge of the detector. This loss of towers needs to be corrected for in the analysis (see Section 3.5.4.1).

3.4 Criteria for Photon Candidate Selection

The method by which π^0s are measured is through the reconstruction of their mass via photon pairs, see Section 3.5.3 below. This means that photons must be identified in the EMCal, seperating them from other (charged) particles hitting the detector. Photon candidates in the EMCal are subjected to a minimum energy requirement, E, of 0.2 GeV, which reduces the effects of noise contaminating the sample.

Variables associated with each EMCal cluster are computed in order to measure photons. The main experimental tool used in this process is a cut on the shower shape, as hadron showers are more broad and spread out over more towers compared to a typical photon shower. Additional cuts on cluster candidates are made independently for each sub–detector of the EMCal. For the PbSc a shower–shape cut of $\chi^2 < 3.0$ is made to reduce the effect of charged hadron contamination in the detector. This chi–squared cut is based on a comparison of the deposited energy in the modules of the cluster to that expected from an electromagnetic shower at the same energy. Similarly, a dispersion cut of $D > 0.45$ is used for the PbGl. Despersion of a cluster is a measure of the extent to which the shower spreads: the shower's width. Because a shower will encompass more towers with increasing angle of incidence θ, see Figure 3.3, this cut must be dependent on θ.

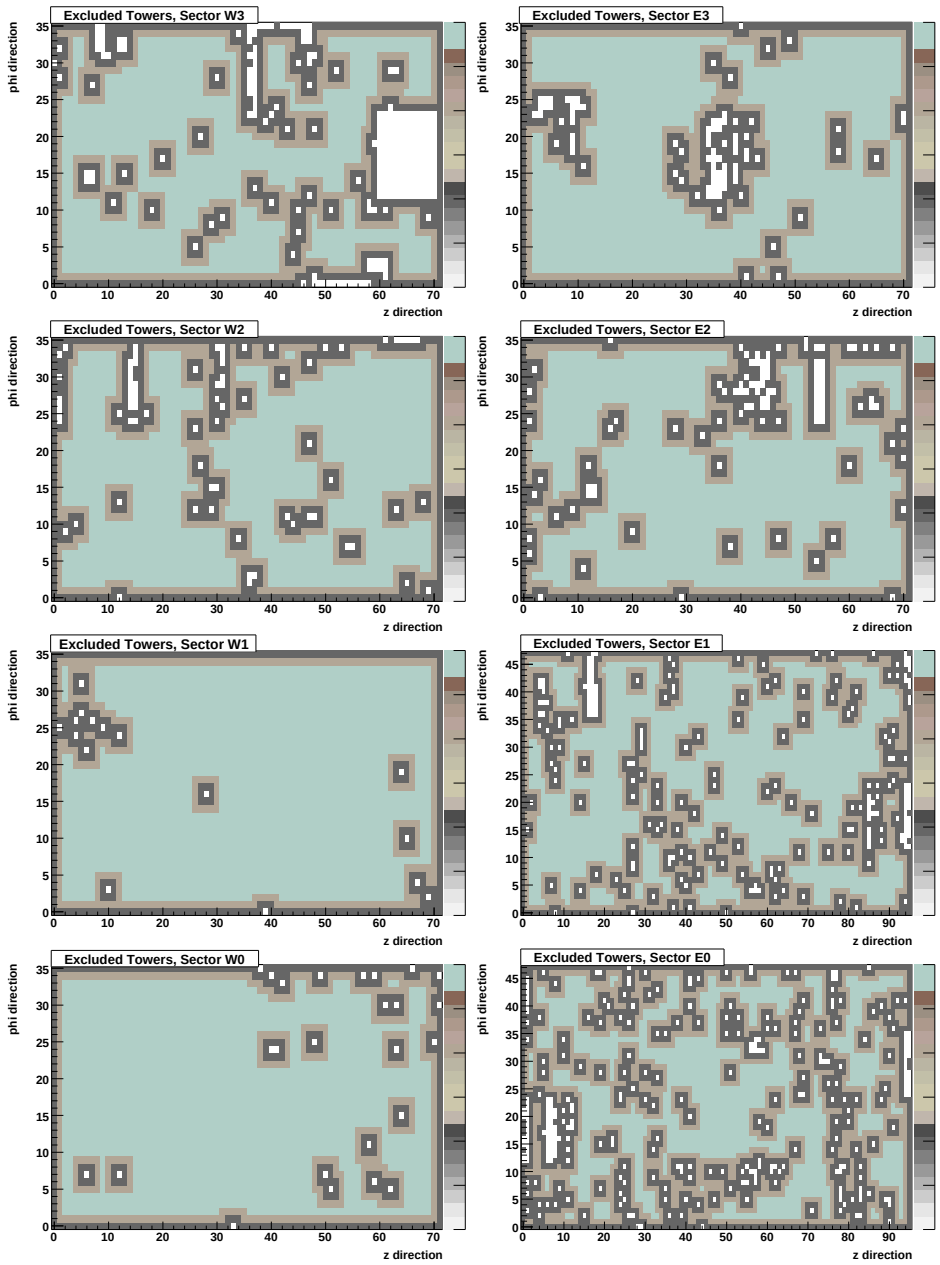

Figure 3.2: Map for non–functioning modules in the eight EMCal sectors. Green denotes good towers, white denotes bad towers. Dark and light brown denote the first and second neighboring towers, respectively.

These cuts, along with the mimimum energy requirement, are grouped into four photon identification catagories, or PIDs, as follows.

3.4.0.1 Photon Identification

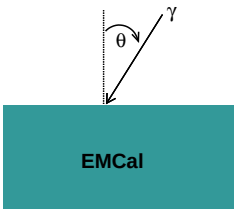

Figure 3.3: Angle of incidence θ onto the PbSc.

- PID0: no cut
- PID1: energy cut only
- PID2: PbSc: chi–square ($\chi^2 < 3$) or PbGl: dispersion ($D > 0.45$) cut
- PID3: PID1 + PID2

All PID catagories are used in the analysis for systematic checks. In principal, if all corrections are calculated correctly, all should result in the same measured yields. The resultant yields are compared and the difference is incorporated in the systematic errors (see Section 3.5.6).

3.5 π^0 Reconstruction

The neutral pion spectra are obtained by reconstructing EMCal cluster pairs. A π^0 will almost always decay electromagnetically into two photons; 98.823% of π^0 decays are via this channel [29]. This is advantageous as it allows for a statistical analysis by pairing clusters indentified as photons and calculating the invariant mass of the pair. Also, random photon pairs may accidently reconstruct close to the π^0 mass, which forms a combinatorial background, see Section 3.5.3. The number of π^0s created in the event can be discerned after considering the combinatorial background pairs, and the raw π^0 spectra are obtained. Once these spectra are obtained, the spectra of decay photons, which is a major background

source to the direct photons is calculated. The first step in this analysis is to reconstruct π^0s and measure their yields as a function of transverse momentum (p_T), which is detailed in this section.

3.5.1 Kinematic Requirements

To begin, EMCal clusters that are candidate photon pairs must follow an energy asymmetry requirement (α) of:

$$\alpha = \frac{|E_1 - E_2|}{E_1 + E_2} < 0.7$$

where E_1 (E_2) is the energy of the first (second) decay photon. The energy asymmetry cut on photon cluster candidates cuts down the large number of photon pairs which do not originate from π^0s(π^0s that decay with a large asymetry have a large opening angle, increasing the likelyhood that one decay photon will miss the detector). The energy spectra of detected particles are very steep. This leads to an increase in photon pairs with a large asymmetry, as a pair with one photon having low energy becomes more likely as compared to the case of a flat energy spectrum.

3.5.2 Mass Peak Calibration

A Monte Carlo simulation is used to estimate the detector acceptance and reconstruction efficiency (see Section 3.5.4.2). As this simulation does not precisely reproduce the signal observed in the detector, a two step calibration is used. First, an overall energy calibration is made to better describe the widths of the π^0 detected in each p_T bin. Secondly, the simulation was tuned so that the π^0 peak positions matched that observed in the raw data.

The simulated π^0 peak widths, versus p_T, were compared to those found in the analyzed data, see Figure 3.4. A small correction factor (0.39%) was found and applied to the simulated data. Once the simulation was tuned, the π^0 peak positions in the data and simulation (Fig. 3.5, top row) were checked for agreement (Fig. 3.5, bottom row).[2]

[2]Initial calibration factors were taken from PHENIX internal analysis note 543 (previous π^0 analysis) and then were adjusted to match simulation and data.

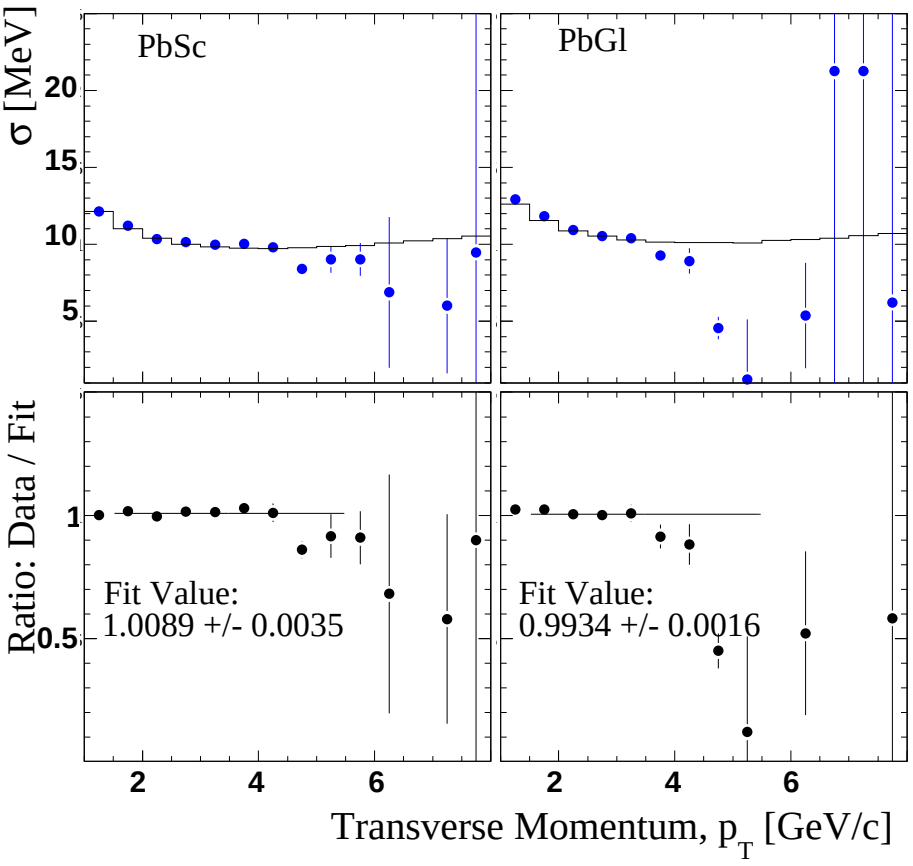

Figure 3.4: Top row: π^0 peak widths in the PbSc (right) and PbGl (left) in the data (blue) and simulation (black) in the 0–10% centrality bin. Bottom row: Ratio of widths, data / simulation, the line shows a fit to a constant from $p_T = 1.5$ to $p_T = 5.5$ GeV/c in PbSc (left) and PbGl (right).

3.5.3 Invariant Mass Reconstruction

Neutral pions decay via the electromagnetic interaction with a short lifetime (10^{-16}s) which prevent their direct detection in PHENIX. Thus π^0s must be reconstructed via an invariant mass technique using their decay daughter photons. For each candidate pair, the invariant mass is calculated from the absolute value of the sum of the particles' 4–momenta $P_{12} = |P_1 + P_2|$. As decay photons are massless the reconstructed invariant mass of the pair simplifies to:

$$m_{\gamma\gamma} = \sqrt{(P_{\gamma_1} + P_{\gamma_2})^2} = \sqrt{E_{\gamma_1} \cdot E_{\gamma_2} \cdot (1 - \cos(\theta_{12}))} \tag{3.1}$$

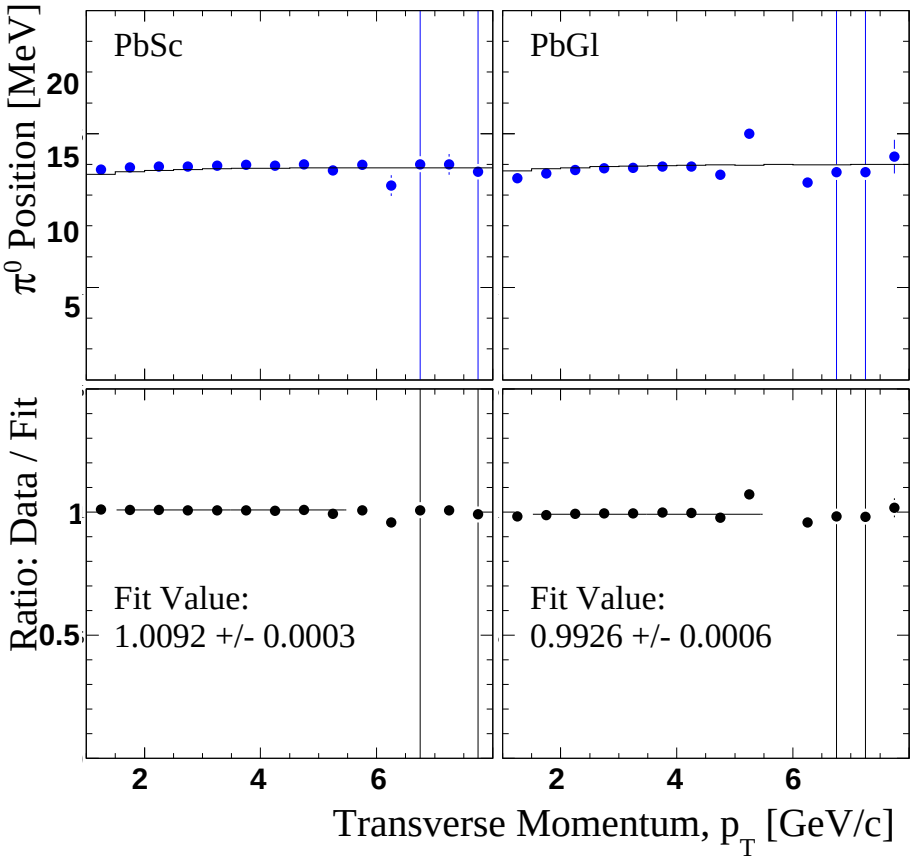

Figure 3.5: Top row: π^0 peak positions in the PbSc (left) and PbGl (right) in the data (blue) and simulation (black) for the 0–10% centrality bin. Bottom row: Ratio of positions, data / simulation, the line shows a fit to a constant from $p_T = 1.5$ to $p_T = 5.5$ GeV/c in PbSc (left) and PbGl (right).

where P_{γ_1} and P_{γ_2} are the 4–momenta of the two decay photons, E_{γ_1} and E_{γ_2} their energies, and θ_{12} is the angle between the two direction vectors (opening angle).

3.5.3.1 Combinatorial Background Subtraction

A photon candidate can come from different sources (for example a candidate could be a decay photon from a π^0, from an η or other meson, a direct photon, a misidentified charged hadron, etc.). Some come from real pairs, others are singletons and one must account for these sources statistically from the ensemble of all photon candidate pairs. To do this an "event mixing" technique is used. The invariant mass of all candidate photons are

reconstructed and those which form a mass close to that of a π^0 are considered π^0 candidates. This cut on the mass allows both real π^0s as well as random combinatorial background pairs into the sample, see Figure 3.6. A mixed event method is used to describe this combintorial background, by pairing photons from different events. Because all correlations in these mixed event photons are necessarily broken (including decay pairs), this mixed event spectrum describes the combinatorial background.

Figure 3.6 shows the method used to account for the combinatorial background. In the top panel, the ratio of real photon pairs to photon pairs from different (mixed) events is shown. This ratio is fit to a Gaussian plus a constant function. The constant value is used to normalize the mixed event photon pairs to match the real pair distribution. The normalized distribution can be seen in the middle panel of Figure 3.6, the scaled mixed events (red) now match the data (black) well in the areas not under the π^0 mass peak (also note the η mass peak around 0.55 GeV/c^2 on the figure). The lower panel in the figure shows the π^0 peak (blue) after the combinatorial background is subtracted; the line shows a Gaussian fit to the data. Figure 3.6 illustrates the event mixing technique using the PbSc in the transverse momentum range $1.0 < p_T < 1.5$ GeV/c. The same technique is used for all p_T bins for the PbGl sub–detector as well.

The raw π^0 yields are calculated as the integral of the Gaussian in the lower panel of Figure 3.6. The analysis is performed independently for each detector, p_T bin, centrality bin, and is repeated for each PID set.

3.5.4 Corrections

Once the raw π^0 spectrum is obtained corrections need to be applied to account for detector effects (for example acceptance) and effects due to analyzing techniques (i.e. different PIDs). These corrections are discussed in this section.

3.5.4.1 Geometrical Acceptance

The geometrical acceptance is a correction that accounts for the fact that the PHENIX EMCal does not cover a full 4π in solid angle. First, the electromagnetic detector covers only $|\eta| < 0.35$ and $\Delta\phi = 2 \times 90°$ (90° for each arm). Each sub–detector covers only a portion of that. This acceptance issue is well defined, and can be corrected for in the analysis. A second order acceptance correction takes into account the bad channels in the eight sectors of the EMCal (see Section 3.3). The geometrical acceptance is calculated using

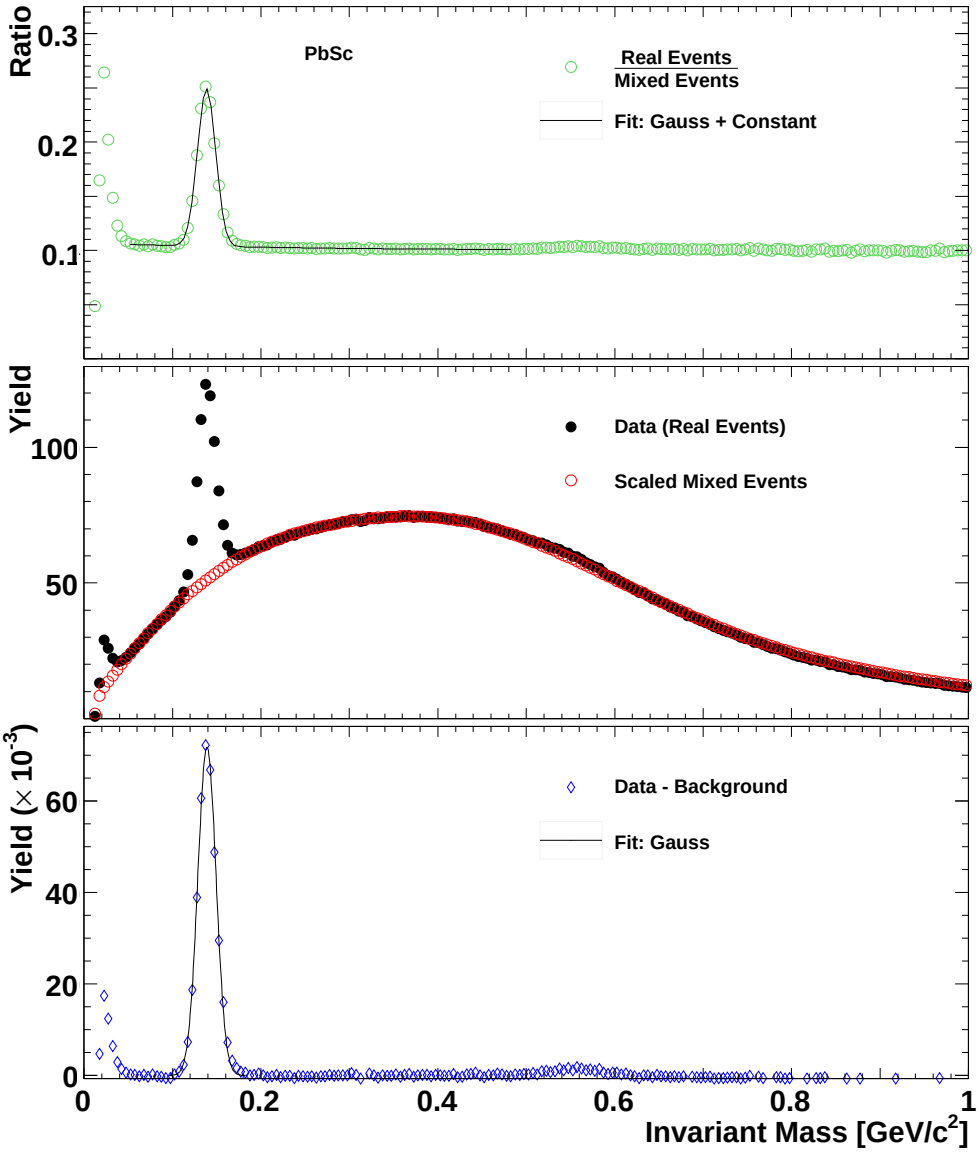

Figure 3.6: Method used to account for the combinatorial background in the invariant mass distribution. The top panel shows the ratio of real events to mixed events (green). This ratio is fit to a Gaussian plus a constant (black line), the constant is then used to normalize the mixed event spectrum. The middle panel shows real events (black) and the scaled mixed events (red). The bottom plot shows the mass peak after the scaled mixed events are subtracted from the real events. Note the rise in the very low mass region in the real events, possibly due to late electron conversion, and the slight rise around 0.547 GeV/c^2, the η meson.

a Monte Carlo simulation in which π^0s are thrown flat in z ($|z| < 30$ cm), in p_T, and with a Gaussian distribution in rapidty ($|\eta| < 0.45$). The geometrical acceptance curves are shown in Figure 3.7 for both the PbSc and PbGl. When a π^0 decays to photons, the opening angle between these two photons is inversely proportional to the p_T of the pion; the lower the energy of the π^0, the larger the angle. A very low p_T π^0 produces near back–to–back decay photons, one of which will miss the detector. Figure 3.7 shows this, as both acceptance curves go to zero as $p_T \rightarrow 0$.

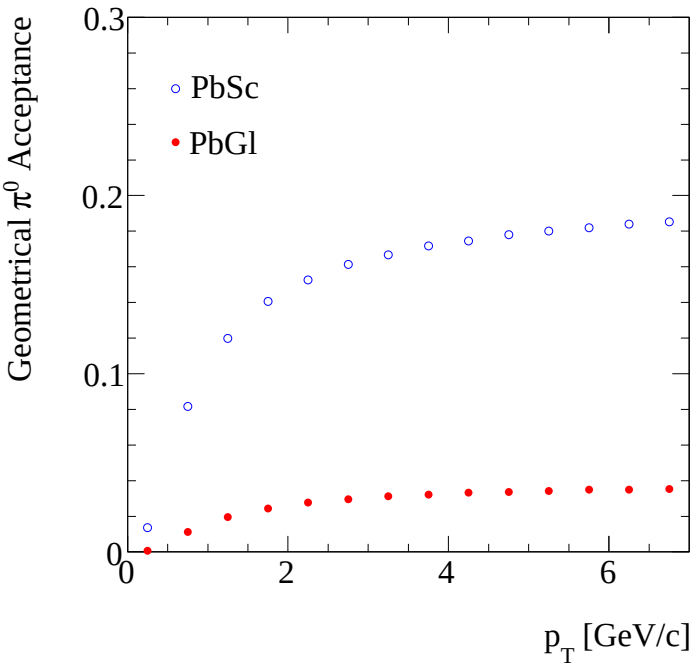

Figure 3.7: The geometrical acceptance of π^0s in the EMCal. The PbGl sub–detector (squares) and PbSc (circles) acceptance is calculated using a fast Monte Carlo.

The simulation is then weighted according to an input spectrum. This input spectrum is based on the raw π^0 data, which has an exponential behavior at lower transverse momentum and power law behavior at higher p_T. Figure 3.8 illustrates the function (black curve) as well as pure exponentional and power law curves for comparison.

3.5.4.2 Reconstruction Efficiency

The reconstruction efficiency correction is used to correct raw spectra for detector specific effects and analysis cuts that modify the true spectra. The reconstruction efficiency

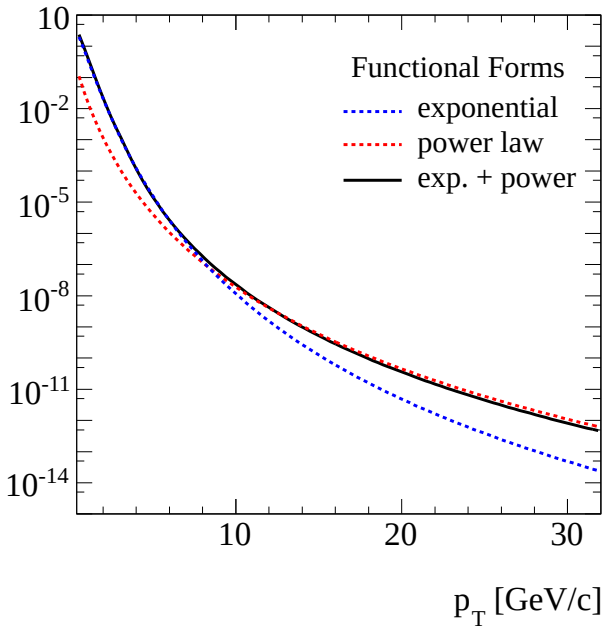

Figure 3.8: Input raw π^0 functional form used to weight the simulation (black curve). The pure exponential (power law) function is shown in blue (red) for comparison.

is defined in Equation 3.2 as a ratio of the resultant π^0 spectra after reconstruction ($f(p_T)_{out}$) and the input spectra ($f(p_T)_{in}$).

$$\epsilon(p_T) = \frac{f(p_{T_{out}})}{f(p_{T_{in}})} \tag{3.2}$$

The output spectrum (and hence the efficiency) is influenced by the position and energy (p_T) resolution of the detector, as well as the various PID and analysis cuts. Also, in the case of the π^0, the efficiency depends on the determination of the yield via the invariant mass technique.

A part of the reconstruction efficiency is speciffically due to the intrinsic resolution of the EMCal. Figure 3.9 illustrates this in two cases. First (in panel a), a simple flat distribution is used to show that the measured energy in the EMCal can be shifted to neighboring bins as the resoultion is larger than the bin width. Averging over many events, the in–flow and out–flow of a particular bin will balence out, and hte original distrubution will be reconstructed. However, if, as panel b of the figure illustrates, the spectra has a steep slope, the change in yield is dominated by the increase from the lower p_T bin. This is

due to an exponentially (or power law) lower value of the higher p_T bin. This leads to an overall shift of the yield to higher p_T, which is corrected for by $\epsilon(p_T)$.

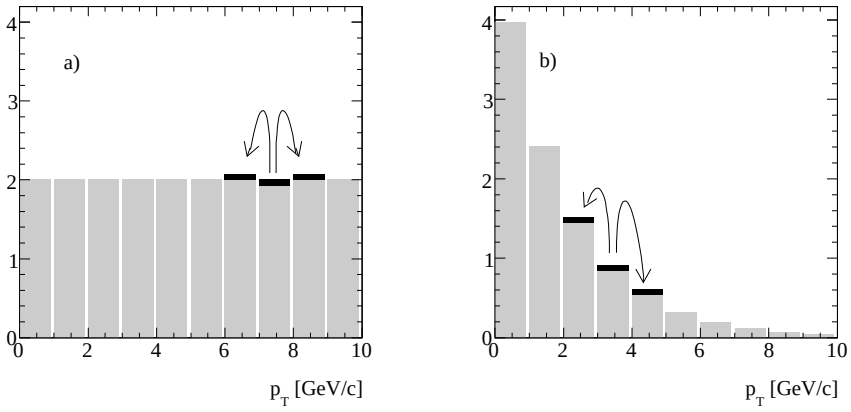

Figure 3.9: Schematic illustration of the need for the efficiency correction. In (a), it can be seen that a smeared photon will contribute equally to a neighboring p_T bin higher or lower than the true bin while in (b), due to the steeply falling slope, a photon smeared to lower p_T will not contribut significantly to the much higher statistics of that bin, while smearing to a higher p_T bin makes a significant contribution.

The π^0 reconstruction efficiency curves are shown in Figure 3.10. Here, the efficiencies are shown for both the PbSc (triangles) and PbGl (squares), as well as for central collisions (open symbols) and peripheral collisions (closed symbols).

Figure 3.10 illustrates a small efficiency loss in central collisions, compared to peripheral. This is due to the higher multiplicity in central collisions, which leads to a higher chance of cluster overlap. This overlap alters the the energy of a single decay photon, causing its mass to be reconstructed outside the π^0 invariant mass window. This effect is smaller in the PbGl than in the PbSc, as the smaller lead – glass towers allow for better hit seperation (better resoultion).

3.5.4.3 Bin Shift Correction

Another consequence of the steeply falling particle yields gives an error when plotting them. The data points should not be located at the center of the p_T bin, as this is not the gravitational center of the bin. For example, consider a p_T range spanning 2 - 3 GeV/c. If the spectra were flat, the data point for this bin shuld be placed at p_T = 2.5 GeV/c. However, in the case of a steep slope, the average of the bin contents is closer to 2

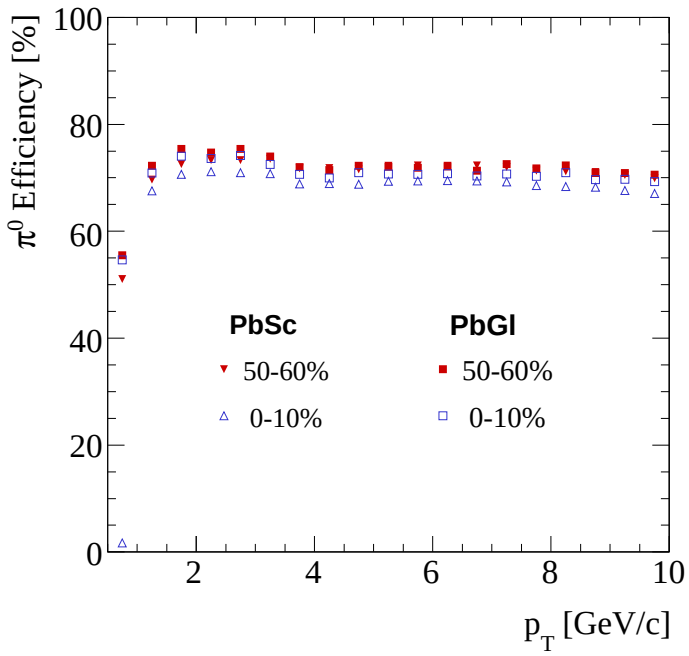

Figure 3.10: Neutral pion reconstruction efficiencies in peripheral (closed points) and central (open points) collisions. The triangles represent the PbSc and squares the PbGl detectors. Reconstruction is slightly less efficient in central collisions due to the possibility of cluster overlap in central collisions.

GeV/c than it is to 3 GeV/c. The bin shift correction accounts for this and places the point at the correct average for the counts in the trasverse momentum bin. It should be noted that there are two ways of making this correction, one is to shift the point horizontally (i.e. shift in p_T) so that the point represents the true center–of–gravity of the bin. The other is to shift the point vertically (i.e. shift in yield itself) such that the point represents the the true value of the yield at the bin's center. Because it is advantageous to compare spectra with other data (compare Cu+Cu data with pp data as in the R_{AA} calculation), the latter method is employed in this analysis. To calculate this bin shift correction, the spectrum is fit with function $f(p_T)$, which is taken as an approximation of the true spectrum. For a given p_T bin with center p_T^{cent} and width $2\Delta p_T$, the average yield ($f(p_T^{avg})$) is then calculated as

$$f(p_T^{avg}) = \frac{1}{2\Delta p_T} \int_{p_T^{cent}-\Delta p_T}^{p_T^{cent}+\Delta p_T} f(p_T)\, dp_T. \tag{3.3}$$

This average value is then compared to the functional value at the bin's center, $f(p_T^{cent})$:

$$r = \frac{f(p_T^{avg})}{f(p_T^{cent})} \tag{3.4}$$

and the bin shift corrected yield is

$$\frac{dN}{dp_T}|_{corrected} = \frac{\frac{dN}{dp_T}|_{uncorrected}}{r} \tag{3.5}$$

As the shifted data give new yields, thus new fits, the fitting and bin–shifting is repeated until negligible changes are seen. This process takes only two or three iterations.

3.5.5 Final Spectra

For completeness, the π^0 spectra are shown here. These will be presented formally and discussed in the next chapter.

Invariant Yields Figure 3.11 shows the neutral pion spectra for the PbSc (left) and the PbGl (right). The error bars in Figure 3.11 represent the total error; the statistical and systematic error added in quadrature. Both plots have the Minimum Bias centrality unscaled in black, and each individual centrality scaled by decades beneath.

3.5.6 Systematic Error

The sources of sytematic error are discussed in this Section, and are summarized in Table 3.2.

3.5.6.1 Energy Scale Uncertainty

One of the main contributions to the systematic error in the π^0 and direct photon analysis is the uncertainty in the determination of the overall energy scale. Comparing the π^0 peak positions (Figures 3.4 and 3.5), a 2% difference between the data and simulation is seen when the energy scale used in the simulation was varied by $\pm$ 2%. The resulting invariant yields differ from those calculated from the default scale by as much as 21% in PbSc and 20% in PbGl (Fig. 3.12). This constitutes the single largest uncertainity in the analysis.

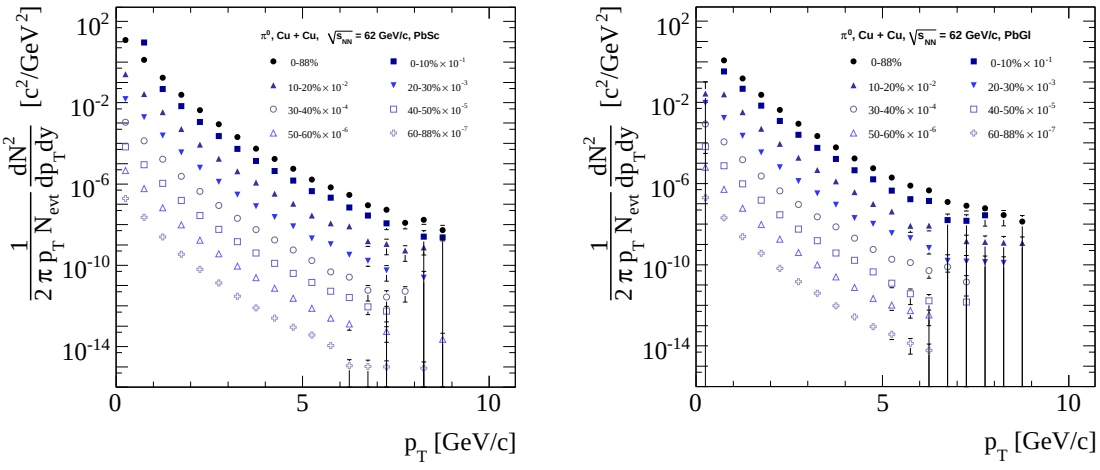

Figure 3.11: Fully corrected inclusive neutral pion invariant yields in PbSc (left) and PbGl (right). The Minimum Bias bin is in black and individual centralities are scaled by decades below, for ease of viewing. The error bars denote statistical and systematic errors added in quadrature.

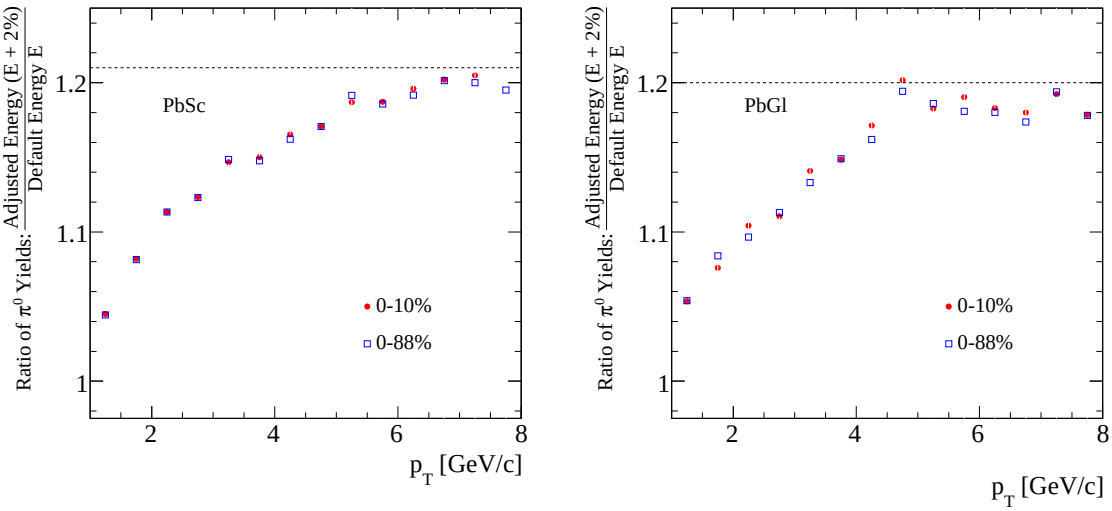

Figure 3.12: The ratio of π^0 yields calculated with the default energy scale and with the energy scale adjusted by 2%, for the most central and minimum bias centrality classes. The introduced error is up to 21% in PbSc and 20% in PbGl.

3.5.6.2 Background Scale Uncertainty

The first source of error due to the π^0 peak extraction comes from the fitting of the ratio of real to mixed events (see Section 3.5.3.1). This ratio was fit with different functional

forms (polynomials of different degrees) and the resulting π^0 yields were compared, see Figure 3.13. The maximum contribution to the error is 4.0%.

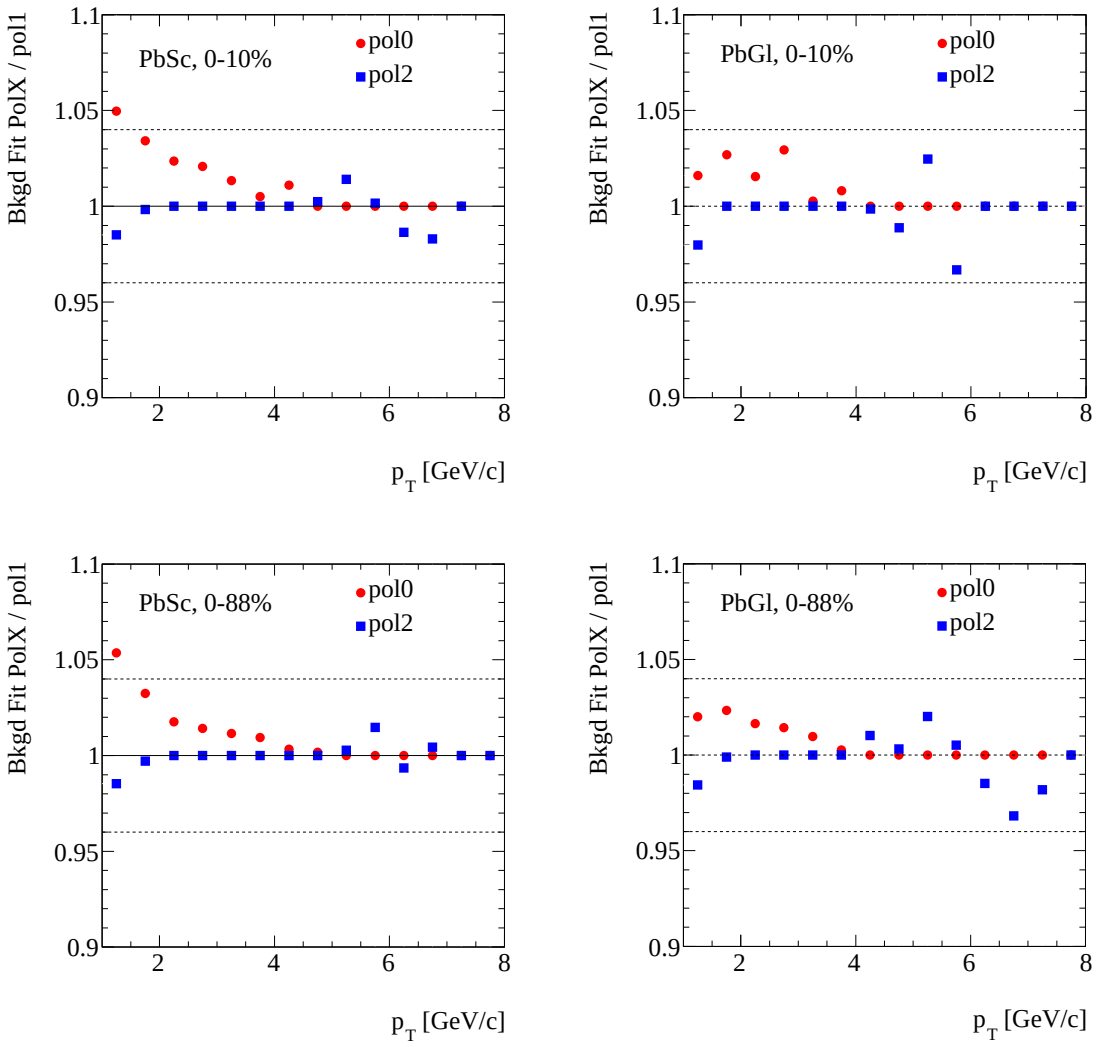

Figure 3.13: Comparison of π^0 yields estimated using different residual background forms. Data are shown relative to the default method (first order polynomial) with different fits (zero and second order polynomials) to the ratio of real / mixed events, for different centrality classes in both PbSc and PbGl. This contribution to the error is estimated to be no larger than ± 4%.

3.5.6.3 Peak Integration Uncertainty

The second contribution to the systematic error due to the π^0 peak extraction is the integration region used in counting the number of π^0s. By varying the width of this

Systematic Error	$p_T < 2$ GeV/c		$2 < p_T < 5$ GeV/c		$p_T > 5$ GeV/c	
(detector)	*PbSc*	*PbGl*	*PbSc*	*PbGl*	*PbSc*	*PbGl*
Energy Scale	8.0%	9.0%	14.0%	15.0%	18.0%	19.0%
Scale on Background	4.0%	4.0%	4.0%	4.0%	4.0%	4.0%
Integration Window	2.0%	4.0%	2.0%	4.0%	2.0%	4.0%
PIDs	4.0%	2.0%	3.0%	2.0%	8.0%	8.0%
Total	10.0%	10.8%	15.0%	16.2%	20.2%	21.4%

Table 3.2: Breakdown of the total systematic uncertainty for the π^0 yields. This is dominated by the energy scale uncertainty. The totals are the individual uncertainity added in quadrature.

window and examining the resulting yields, an error of no more than ±6% (±5%) is assigned for PbSc (PbGl). See Fig. 3.14.

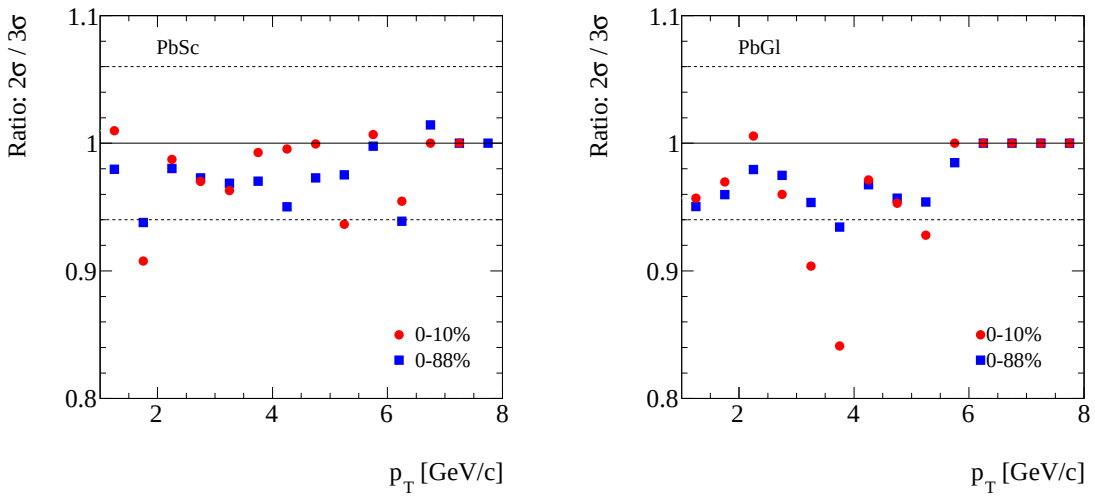

Figure 3.14: The estimated contribution to the systematic uncertainty from π^0 peak integration window. Plotted is the ratio of yields calculated with a two sigma window to the yields calculated with a 3 sigma window. Using a 3σ window rather than a 2σ window results in 6% difference in PbSc and 5% in PbGl.

3.5.6.4 PIDs Method Uncertainty

The π^0 yields calculated using the various PID methods (see section 3.4.0.1) are compared in figure 3.15. There is a 6% error contribution.

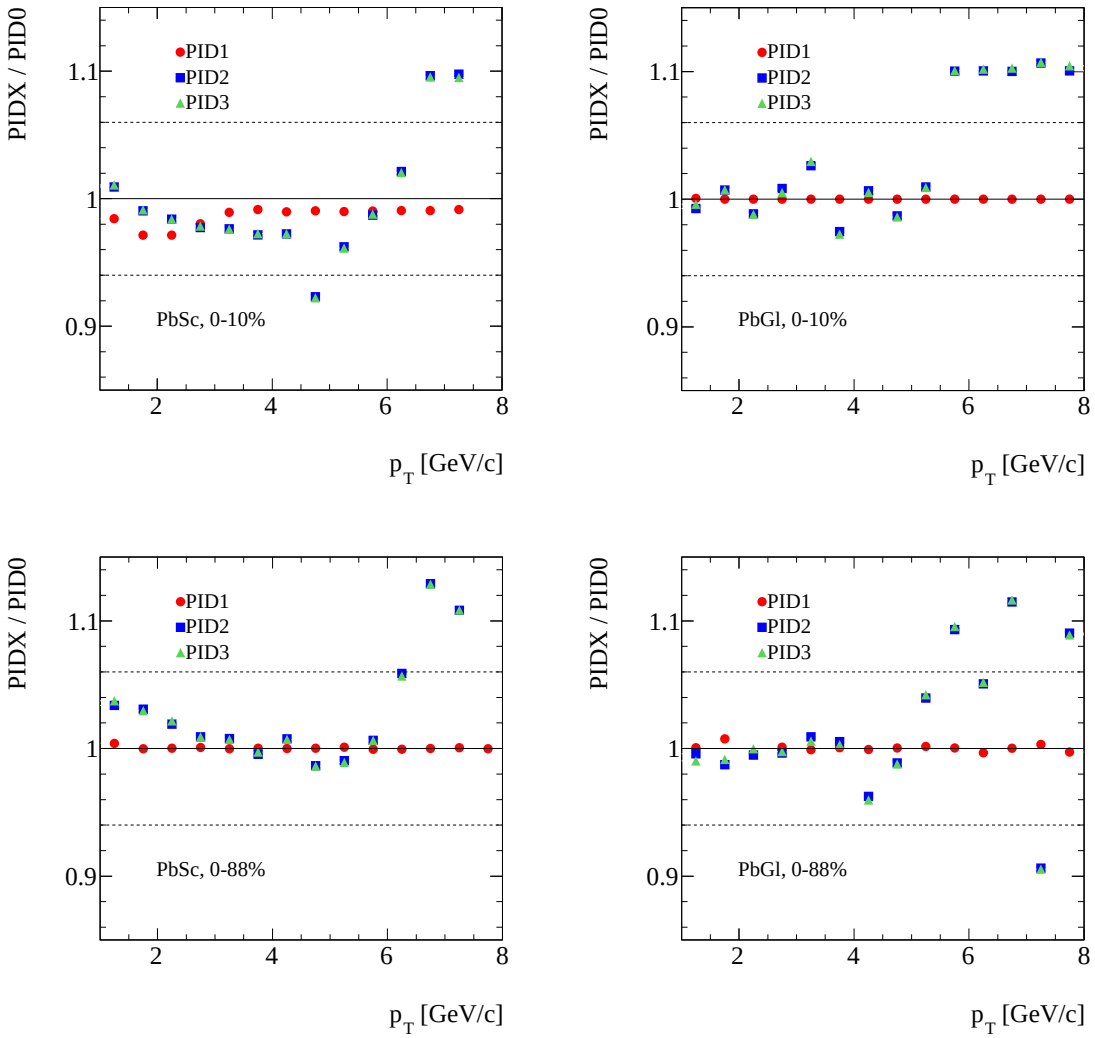

Figure 3.15: π^0 yields estimated for each set of PID cuts (or selections), as calculated in the most central (top panels) and Minimum Bias (bottom panels) centrality bins for each detector.

3.6 Photon Reconstruction

3.6.1 Inclusive Photons

The ultimate goal of this analysis is to measure direct photons and the direct photon nuclear modification factor, R_{AA}, in Cu+Cu collisions at $\sqrt{s} = 62.4$ GeV. The direct photon spectrum is obtained via a well–established procedure which compares the measured inclusive photon spectrum (γ_{inc}) to that of the π^0s. A ratio of the number of

measured inclusive photons to the number of measured neutral pions (π^0s) is used in order to cancel many of the associated systematic uncertainties. The same ratio is also formed from a fast simulation of photons resultant from decays only ($\pi^0 \to \gamma\gamma$, $\eta \to \gamma\gamma$ etc.). A ratio is formed between the γ/π^0 from data to that in the simulation (see Equation 3.6.)

$$R_D = \frac{(\frac{\gamma}{\pi^0})_{meas}}{(\frac{\gamma}{\pi^0})_{sim}} \tag{3.6}$$

Here $(\frac{\gamma}{\pi^0})_m$ and $(\frac{\gamma}{\pi^0})_s$ denote the γ/π^0 from data and simulation, respectively, and any excess (i.e. above unity) in this ratio is considered to be the direct photon signal. This is further described in Section 4.2.

In order to calculate the double ratio, one must first obtain the corrected inclusive photon spectra. The γ_{inc} spectra are calculated as:

$$\frac{dN_{\gamma_{inc}}}{dp_T} = \frac{1}{a_\gamma \cdot \epsilon_\gamma} \cdot (1 - X_{ch}) \cdot (1 - X_{nn}) \frac{dN_{cluster}}{dp_T} \tag{3.7}$$

where $\frac{dN_{cluster}}{dp_T}$ is the raw EMCal cluster p_T distribution, a_γ is the geometrical acceptance of the EMCal (including the reduction due to bad channels), and ϵ_γ is the reconstruction efficiency. Two additional correction factors account for mis–identified charged hadrons $(1 - X_{ch})$ and neutrons and anti–neutrons $(1 - X_{nn})$. These will be discussed later. The corrections applied to the data (detailed below) are derived from Monte Carlo studies of the detector response, as well as from the data itself.

3.6.2 Corrections

3.6.2.1 Geometrical Acceptance

The geometrical acceptance describes the physical coverage of the detector. As the PHENIX EMCal does not cover the full azimuth (approximately half is covered, in the region $|\eta| < 0.35$), a global factor is calculated for the acceptance, which is approximatly 25% for the PbSc and 6% for the PbSc (see below for details). A more detailed consideration of non–functioning detector channels further reduces the acceptance, thus a still larger correction factor is needed. The acceptance is calculated in the same way as for the neutral pions using a fast Monte Carlo simulation. From that simulation, the fraction of single photons hitting the detector's surface is calculated relative to the input spectrum. In order to study the acceptance the input Mote Carlo spectrum has the following characteristics:

- Flat transverse momentum distribution: $0 < p_T \leq 32$ GeV/c.
- Uniform vertex distribution: $|z_{vtx}| \leq 30$cm.
- Rapidity distribution: Gaussian centered at zero with $\sigma = 3$ and $|y| \leq 0.45$.
- Uniform ϕ distribution with $\Delta\phi = 2\pi$.

The resulting acceptance corrections are shown, for PbSc and PbGl, in Figure 3.16. Note the PbGl acceptance is significantly smaller with respect to the PbSc, due to the former making up three quarters of the EMCal. There is also a slight p_T dependence, particularly in the PbSc. The acceptance of both detectors is, of course, centrality independent.

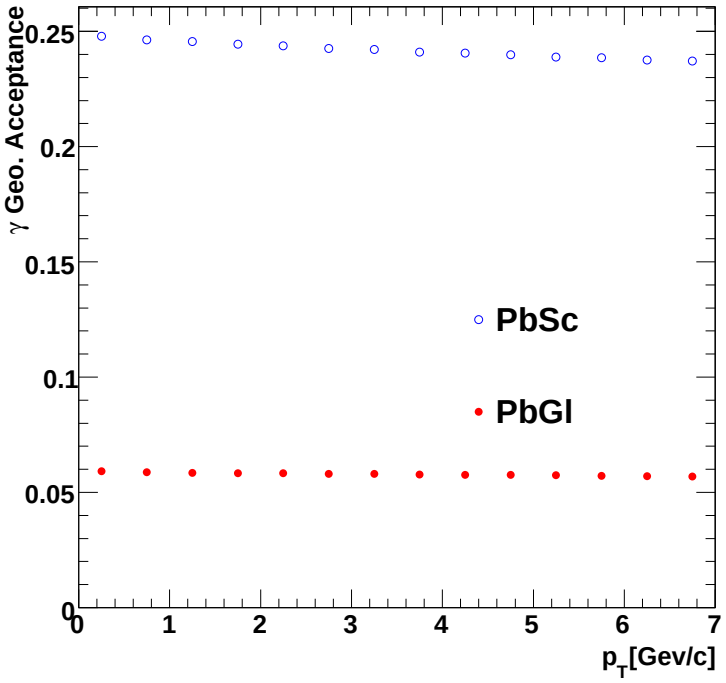

Figure 3.16: Geometrical acceptance for the two sub–detectors, PbSc (open circles) and PbGl (closed circles). The nominal acceptance is $\sim 25\%$ for PbSc and $\sim 6\%$ for PbGl.

3.6.2.2 Reconstruction Efficiency

The efficiency of reconstructing single photons is estimated using an algorithm similar to that for the π^0 analysis. Events with a single cluster on an active portion of the detector are taken into account. Any bad towers in the detector are excluded here, along

with edge towers to avoid energy loss outside the EMCal acceptance. The efficiency does not include the detector's geometrical acceptance. Figure 3.17 shows these corrections for the PbSc and PbGl, for the Minimum Bias centrality class. The efficiency in both detectors is seen to lie flat in transverse momentum $p_T > 2$ GeV/c. The fall off at low p_T is representive of the fact that photons with zero transverse momentum are not reconstructed due to the physical location of the detector, hence reconstruction efficiency must be zero at $p_T = 0$. In addition, the efficiency includes a correction for photon smearing, a detector effect resulting from the finite dimensions of the EMCal towers (see Sections 2.2.3.1 and 2.2.3.2). The smearing of the cluster energy has the effect of pushing the entire spectra to a larger p_T, thus requiring a correction to return the γ_{inc} data to the true values, which leads to a value larger than 100% for the total correction.

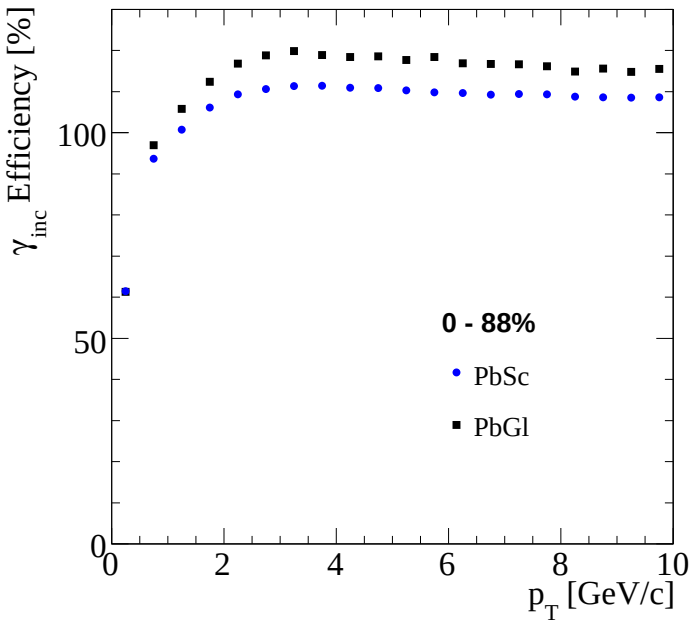

Figure 3.17: Photon reconstruction efficiency versus p_T for the two sub–detectors in minimum bias collisions. This efficiency excludes the geometrical acceptance.

3.6.2.3 Bin Shift Correction

The inclusive photon spectra were bin–shift–corrected in the same manner as the neutral pions. It is important to note that the same functional form was used in the bin

shift corrections for both the π^0s and the photons (although different function parameters were used). This functional form represents the dual shape of the spectra, exponential in lower p_T, and power law at higher p_T.

3.6.2.4 Charged Hadron Contribution

For the inclusive photon measurement, mis–identified charged particles in the EMCal are a large source of background. A significant fraction of this charged particle contamination can be removed from the inclusive photon spectrum by employing the PHENIX PC3 (see Section 2.2.4). This correction is not absolutely necessary in the π^0 analysis as these only contribute to the combinatorial background and not to the signal peak. In this analysis, the charged–hadron contamination is removed statistically by considering the distribution of distances between straight line tracks from the event vertex, through the PC3 hits and extrapolated to the EMCal surface (r_{CPV}). As photons do not leave any track through the Pad Chamber (PC3), a random association is made for those. For charged–hadrons, a track is formed prior to impinging on the EMCal. Thus, a correlated distribution is formed. Figure 3.18 shows the distance r_{CPV} to the nearest PC3 hit. The real distribution shows the $r_{CPV} \geq 0$ peak for charged–hadrons and random associations. The mixed sample (shaded region) only shows random associations. However, as the mixed events and the real data do not match precisely[3], a fit to the real data is made in the region away from the charged–hadrons. The background is fit in the region $r_{CPV} > 20$ cm (to exclude any effects from the charged–hadron signal region) and the fit is extrapolated back to $r_{CPV} = 0$ cm as motivated from the mixed events. The fit is then used to subtract the random associations. Figure 3.18 (left panel) shows the r_{CPV} distribution and the (extrapolated) fit to the random associations for the PbGl in the transverse momentum range $2.5 < p_T < 3.0$ GeV/c (along with the mixed event associations). The right of Figure 3.18 shows the result of the subtraction. Note that the correlated peak close to $r_{CPV} \sim 0$ is the background that should be removed.

The final correction applied to the data is $(1 - X_{ch})$ where X_{ch} is the fraction of candidates which are charged (see Equation 3.8). Figure 3.19 shows the charged particle correction, X_{ch}, for minimum bias events. X_{ch} is calculated as:

$$X_{ch} = (1/\epsilon) \cdot (N_{chgd}/\gamma_{tot}) \tag{3.8}$$

[3]This mismatch is incorporated into the systematic uncertainty.

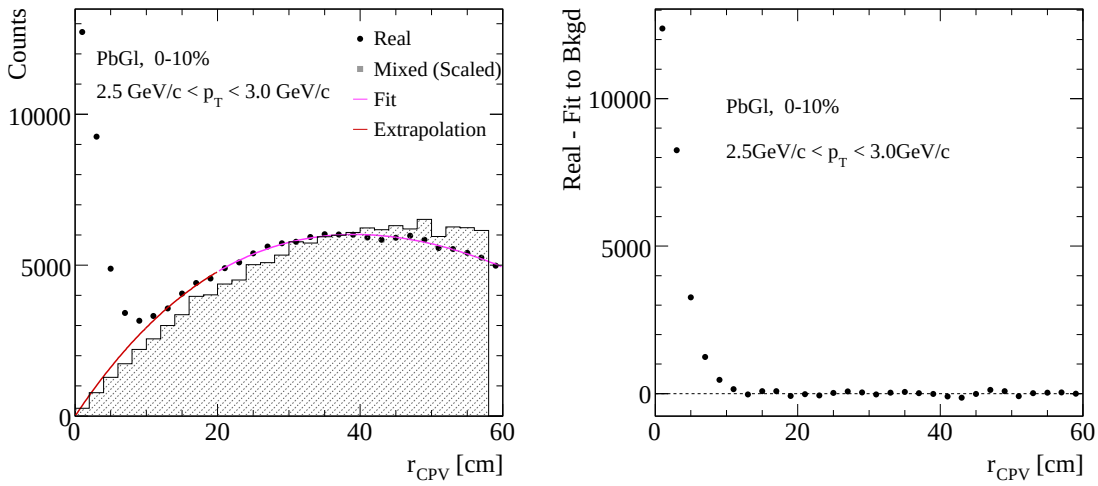

Figure 3.18: The left panel shows the distance between EMCal cluster positions and projected PC3 hits for real (closed circles) and scaled mixed events (shaded region). The mixed event spectrum is also shown, and illustrates that this technique cannot be employed to precisely represent the random associations as it does not describe the data perfectly. The right panel shows the resulting background–subtracted peak.

where ε is the hit efficiency in the PC3 (taking into consideration dead areas in the detector), γ_{tot} is the total number of EMCal clusters in a given p_T range, and N_{chgd} is the number of charged tracks in the extracted peak, see Figure 3.19. In the figure it is seen that the charged hadron contamination is largest at low transverse momentum (at $p_T <\sim 1$ GeV/c), and nearly negligible beyond: the correction is flat in that range. Also, the figure shows the difference in the correction when calculated with the fit method describe above, than that calculated with the mixed event method, which yields an estimate of the associated systematic uncertainties. Those are then incorperated into the overall uncertainity in the measurement.

3.6.3 Systematic Error

As for the π^0s, each correction, or choice made, to the inclusive photon spectra is a potential source of systematic uncertainity. These errors are discussed in this section and are summarized in Table 3.3.

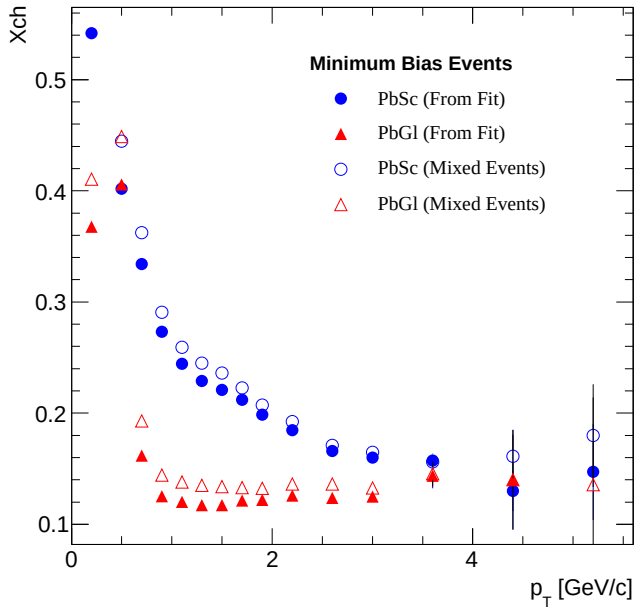

Figure 3.19: Estimated fraction of EMCal clusters which were due to charged particles, in PbSc (circles) and PbGl (triangles). The closed points are the charged correction as calculated with the fit to the distance distributions (r_{CPV}). The open points are the correction calculated with the mixed event technique (see text). The difference in the two calculations is incorporated in the systematic error.

3.6.3.1 Energy Scale

The uncertainty on the energy scale is estimated to be 2%, and, as discussed in Section 3.5.6, the resulting errors are 21% in PbSc and 20% in PbGl.

3.6.3.2 Efficiency Calculation

The uncertainty resulting from the efficiency calculation can be estimated by examining the effect of the different PIDs on the yields [38]. If all corrections estimated were perfect, the resulting spectra from each PID would give the same result. The default photon identification set used is PID3, and the resultant yields from each PID is compared to that, see Figure 3.20. The maximum uncertainty due to this is estimated to be 15% in the PbSc and 10% in the PbGl.

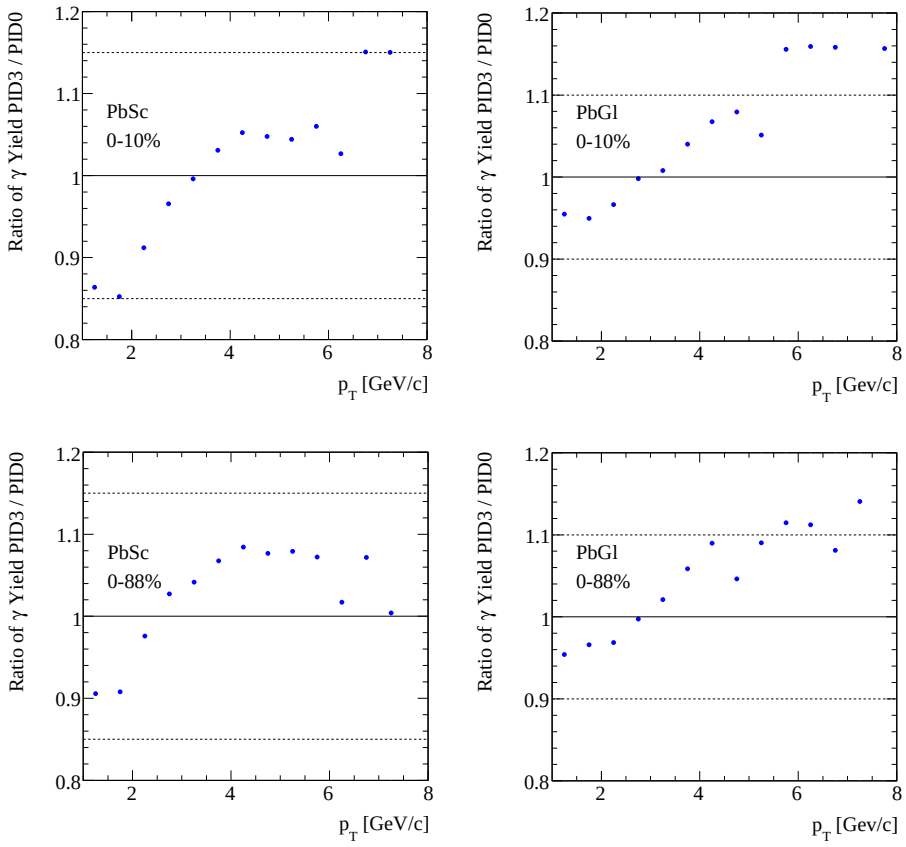

Figure 3.20: Ratio of the yields as calculated with different PIDs, for PbSc and PbGl, in the most central bin and the Minimum Bias bin. The dashed lines represent a conservative estimation of the errors due the identification cut set used.

3.6.3.3 Conversions

The material budget between the collision vertex and the EMCal for the Run05 Cu+Cu is described in Reference [38]. This material causes photon conversions that must be corrected for (9.6 % in the PbSc and 9.1% in the PbGl [38]), with an associated 2.0% uncertainity introduced to the measured spectra.

3.6.3.4 Charged and Neutral Particles

The final systematic uncertainties on the inclusive photon spectra are due to the removal of charges and neutral particle contamination. For the charged hadron contribution the source of the error is due to the background fit uncertainity, see Figures 3.18 and

Systematic Error Source	p_T< 2 GeV/c		2 < p_T< 5 GeV/c		p_T> 5 GeV/c	
(detector)	*PbSc*	*PbGl*	*PbSc*	*PbGl*	*PbSc*	*PbGl*
Energy Scale	7.80%	8.10%	20.70%	20.00%	21.30%	21.30%
Efficiency	15.00%	5.00%	7.70%	5.00%	5.00%	14.00%
Conversions	2.00%	2.00%	2.00%	2.00%	2.00%	2.00%
Charged Particles	2.00%	2.00%	4.00%	4.00%	2.00%	2.00%
Neutral Particles	0.48%	0.48%	0.01%	0.01%	<0.01%	<0.01%
Total	17.88%	10.16%	22.43%	20.81%	22.09%	25.66%

Table 3.3: Systematic errors estimated for the inclusive photon yields.

3.19. This uncertainity is p_T dependent, and estimated to be 2% in the ranges $p_T < 2$ GeV/c and $p_T > 5$ GeV/c, and 4% for $2 \leq p_T \leq 5$ GeV/c. Because the error due to neutron contamination is estimated from proton and anti–proton spectra [39] it has a larger associated error, which is estimated to be 40%[39]. However, the yield of neutrons is small. The neutron contamination is present only for $p_T <\approx 2$ GeV/c [38], and for $p_T > 2$ GeV/c, this error is negiligable (see Table 3.3).

3.6.3.5 γ and π^0 Ratios

The first step in the double ratio method is to calculate the γ/π^0 with both the data and the simulation. The ratio of π^0 spectra to the γ_{inc} spectra are calculated in both the data and simulation, for each centrality. These are shown in Figure 3.21 for the PbSc (left) and PbGl (right), where the black symbols represent the data, and the red is the expected decay background from the simulation. The simulation does not contain any information on direct photons, thus, the simulated photon spectra contain only photons due to decays (decays of π^0, η, ω, η', and K^0 mesons).

3.6.3.6 Double Ratio

After the γ_{inc} to π^0 ratio(s) are calculated (see Section 3.6.1, Equation 3.6), the double ratio can be formed. The ratio of the two quantities in Figure 3.21 are shown for the PbSc (left) and PbGl (right) in Figure 3.22 for the Minimum Bias centrality class. These ratios and their use in calculating the direct photon R_{AA} will be examined in the following chapter.

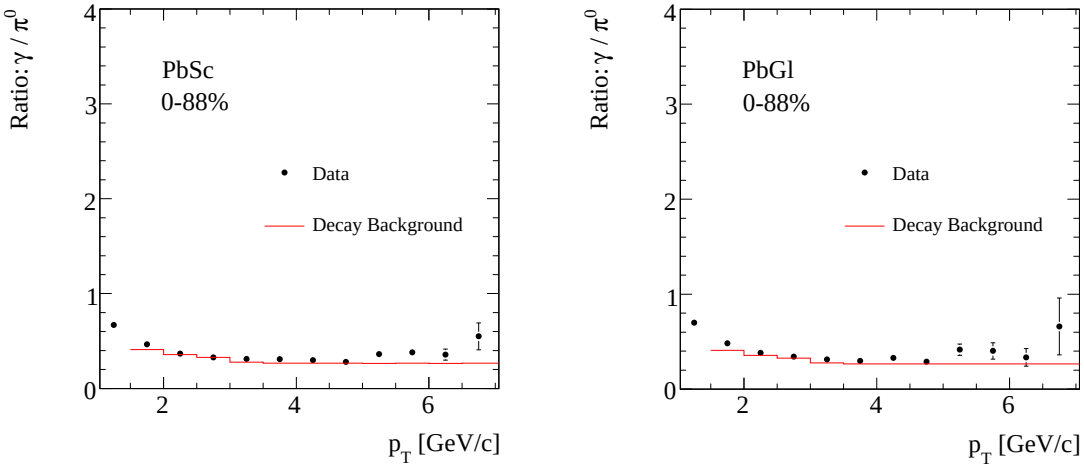

Figure 3.21: γ/π^0 ratios in the PbSc (left) and the PbGl (right). The ratios in data are shown in black. The red is the expected decay photon background. Both panels represent the Minimum Bias centrality class.

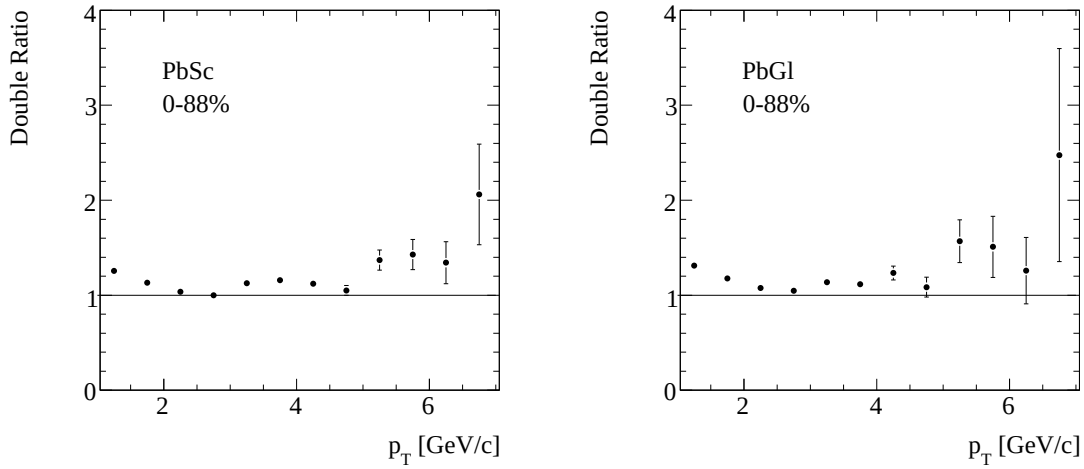

Figure 3.22: Double Ratio in PbSc (left) and PbGl (right) for the 0–88% centrality class. The excess photon signal can be seen here as the value of the ratio moves above unity with p_T.

3.6.4 Final Spectra

For completeness, the γ_{inc} spectra are shown here. These will be presented formally and discussed in the next chapter.

3.6.4.1 Invariant Yields

The inclusive photon invariant yields are shown in Figure 3.23 for PbSc (left) and PbGl (right). In the figure, as with the π^0 spectra, the centralities are offset by one order of magnitude from one another, for clarity in viewing. The error bars denote the statistical and systematic errors added in quadrature.

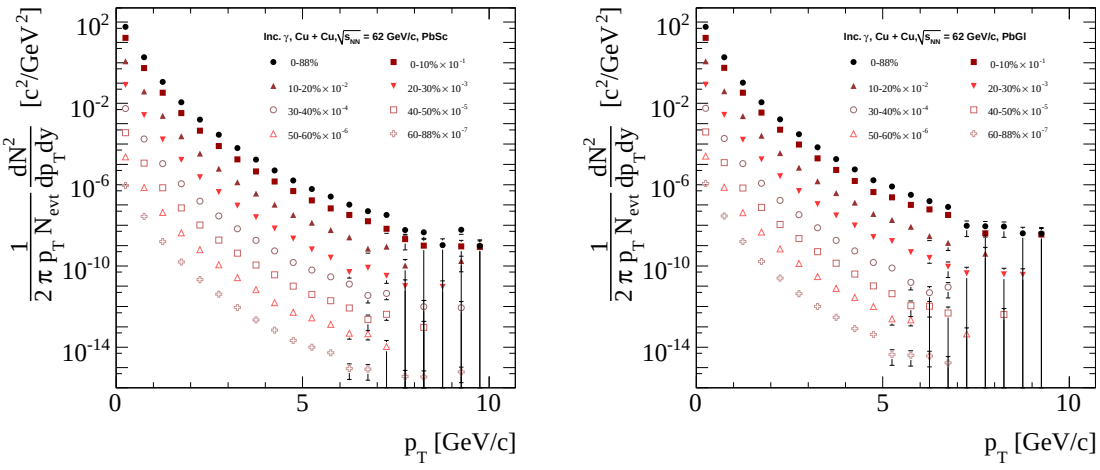

Figure 3.23: Fully corrected inclusive γ yields for PbSc (left) and PbGl (right). The Minimum Bias bin is shown in black and individual centralities are scaled by decades below, for clarity. The error bars denote statistical and systematic errors added in quadrature.

Chapter 4

Results and Discussion

The neutral pion, inclusive photon and direct photon results are presented in this chapter. Discussion and comparisons will be made to other results and to theoretical predictions as well.

4.1 Neutral Pion Spectra

The Lorentz invariant cross–section for particle production in heavy ion collisions is expressed as:

$$E\frac{d^3\sigma}{d\vec{p}^3} = \frac{1}{2\pi p_T N_{\rm in}} \cdot \frac{d^2N^X}{dp_T dy} \cdot \sigma_{\rm in}, \tag{4.1}$$

where N^X is the total number of particles produced in $N_{\rm in}$ number of inelastic reactions with total inelastic cross–section $\sigma_{\rm in}$. Because the calculation of the total cross–section ($\sigma_{\rm in}$) involves the beam luminosity, which is only studied in detail for pp collisions, [39], particle spectra are instead expressed as the Lorentz invariant form of the differential particle yield:

$$\frac{1}{2\pi p_T N_{\rm in}} \cdot \frac{d^2N^{\pi^0}}{dp_T dy} = \frac{1}{2\pi p_T N_{\rm in}} \cdot \frac{dN^{\pi^0}}{dp_T dy}. \tag{4.2}$$

Here, dN^{π^0} represents the number of π^0s produced (in $N_{\rm in}$ reactions) inside the transverse momentum range dp_T and the rapidity window dy. The raw yields ($N^{\pi^0}_{\rm raw}$) obtained using the PHENIX EMCal must be corrected for the detector's acceptance, efficiency, etc., as discussed in Section 3.5.4. By applying these corrections to $N^{\pi^0}_{\rm raw}$, Equation 4.2 becomes

$$\frac{1}{2\pi p_T N_{\rm in}} \cdot \frac{d^2N^{\pi^0}}{dp_T dy} = \frac{1}{2\pi p_T N_{\rm evt}} \cdot \frac{1}{a(p_T) \cdot \varepsilon(p_T) \cdot c_{\rm conv} \cdot c_{\rm channel}} \frac{d^2N^{\pi^0}_{\rm raw}}{dp_T dy}. \quad (4.3)$$

which represents the fully corrected yields. The terms in Eqn. 4.3 are described in Section 3.5.4 and are as follows:

- $N_{\rm evt}$: Number of events
- $a(p_T)$: Geometrical acceptance of the detector
- $\varepsilon(p_T)$: π^0 reconstruction efficiency
- $c_{\rm conv}$: Correction for conversions of decay photons
- $c_{\rm channel}$: Decay channel correction. This number is: $c_{\rm channel} = 0.98798 \pm 0.00032$[29]
- $N^{\pi^0}_{\rm raw}$: Number of raw π^0s detected in the EMCal

The fully corrected spectra are shown in Figure 4.1 for the PbSc and PbGl. The spectra fall–off steeply with p_T, as expected. This fall–off lessens toward higher p_T, as the transition from an exponential shape to a power law takes place as described in Section 1.2. Power law fits proportional to $\frac{1}{p_T^n}$ to these spectra for $p_T > 3.75$ GeV/c give an n value of ~ 10.1. (10.0 ± 0.3 in the most central bin, 10.2 ± 0.21 in the minimum bias bin).

The error bars in Figure 4.1 denote the statistical errors and the systematic errors combined in quadrature. The centralities and systematics were calculated as described in the analysis chapter, Sections 3.2.2, and 3.5.6 respectively. Errors which descend through the x–axis represent upper limits only on the respective data point.

Figure 4.2 shows the ratio of π^0 spectra in PbSc to those in the PbGl, for each centrality bin.
The spectra agree within 2σ in all centralities, and justify combining PbSc and PbGl into a single spectrum. The reason for combining PbSc and PbGl is to reduce the statistical uncertainties in the result. For the remainder of this Thesis, data shown are combined for an average EMCal result.

Figure 4.3 shows the final (combined) π^0 spectra. In the figure, the minimum bias bin represents more than 126 million events. The individual centrality bins that form the minimum bias bin have been offset from one another by one order of magnitude, to make them clearly visible.

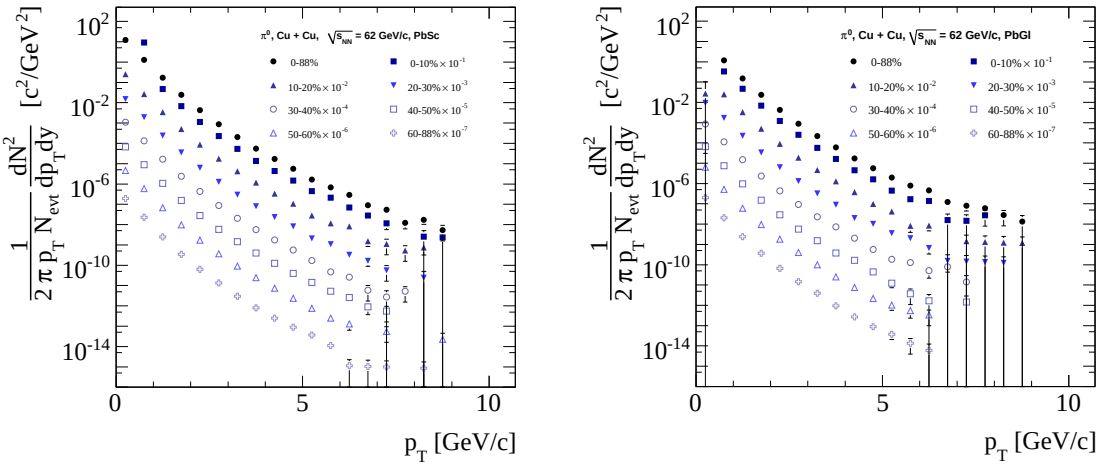

Figure 4.1: Neutral pion yields in Cu+Cu at $\sqrt{s_{NN}}$ = 62.4 GeV, for all centrality classes as measured by PbSc (left) and the PbGl (right). The different centrality bins have been offset below the Minimum Bias spectrum by decades for clarity.

Suppression The suppression of particle production in Au+Au collisions, when compared to *pp* is well established [8, 45, 47]. As noted in the introduction, the goal of this analysis and Thesis is to examine whether this suppression is also seen in the smaller Cu+Cu system at smaller collision energy. The nuclear modification factor R_{AA} is used to compare particle production in heavy ion collisions to that in *pp*. Figure 4.4 shows the R_{AA} calculated in Cu+Cu collisions at $\sqrt{s_{NN}}$ = 62.4 GeV. In the Figure, R_{AA} is plotted for the most peripheral, most central, and minimum bias bins (60–88%, 0–10%, and 0–88% repectively). At high–p_T ($p_T > 2$ GeV/c), the peripheral bin is roughly unity; R_{AA} is $\sim$ one, corresponding to no nuclear modification. However the central bin is clearly below unity, illustrating π^0 suppression. The Mininmum Bias bin lies between the two, reflecting the fact that it contains both peripherial and central collisions, though dominated by central collisions. Due to this dominance, the Minimum Bias bin more closely resembles the central bin than the peripheral bin. The suppression in the central bin is thought to be a result of the formation of the quark gluon plasma. A scattered quark resultant from a hard collision interacts with the produced medium which reduces its energy (energy loss). Upon fragmentation (the quark fragments into hadrons), which is thought to occur after the quark exists the medium, the π^0 is at a lower transverse momentum than it would have been in the absense of the medium.

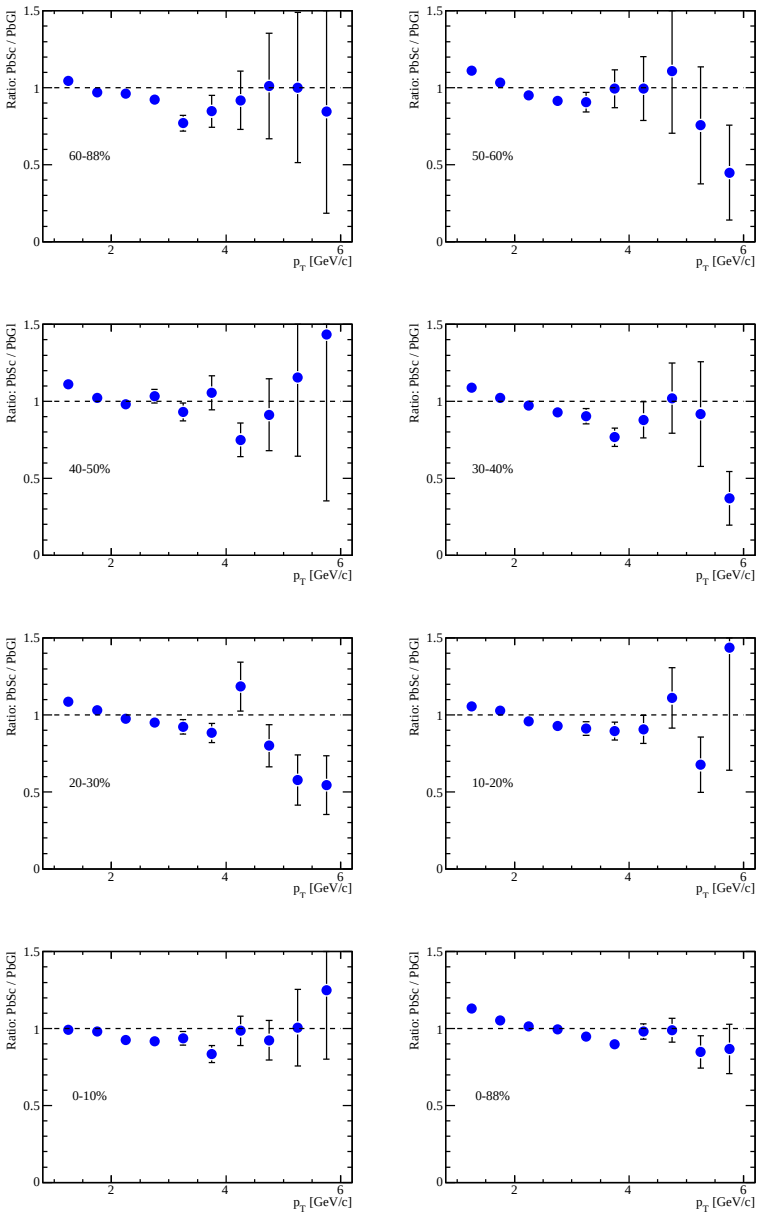

Figure 4.2: The ratio of π^0 yields in PbSc to PbGl. The top left panel is most peripheral, bottom left most central, and the minimum bias centrality bin is the lower right panel. The π^0 spectra in the two sub-detectors agree within 2σ, justifying combining the two results into one.

Integrated R_{AA} Another way to illustrate suppression in heavy ion collisions is to examine the Nuclear Modification Factor as a function of centrality, or $N_{\rm part}$. To do this, the R_{AA} is integrated over a certain p_T range, in separate centrality bins, and plotted at

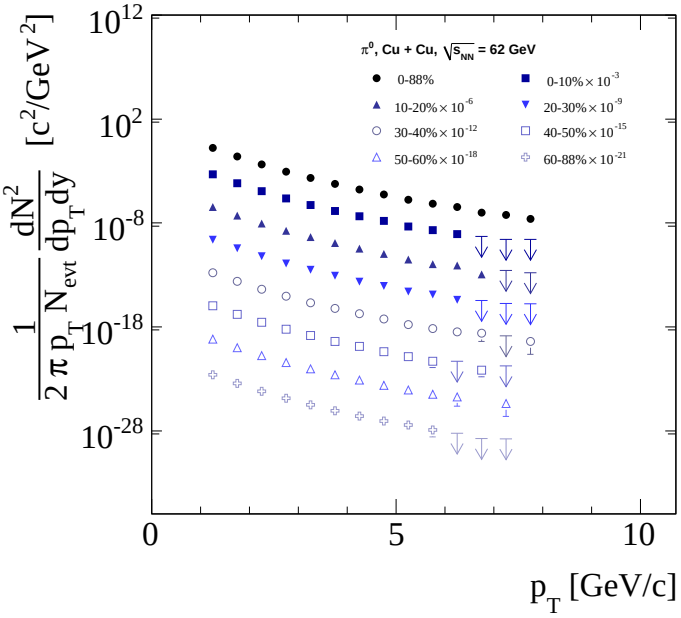

Figure 4.3: Neutral pion yields measured at midrapidity $|y| < 0.35$. The minimum bias spectrum (top, black points) represents more than 126 million events. The individual centralities have been scaled by decades for clarity, and to accommodate the downward point arrows. These arrows represent data points which can only be statistically described as upper limits.

the average $N_{\rm part}$ for that bin. Figure 4.5 shows π^0 R_{AA} versus $N_{\rm part}$, integrated over the transverse momentum range: $2.5 < p_T < 3.5$ GeV/$c$where a steady decrease of R_{AA} with is observed.

4.2 Inclusive and Direct Photon Spectra

4.2.0.2 Inclusive Photon Spectra

As with the neutral pion spectra, the inclusive photon spectra are expressed in terms of the invariant yield (see Section 4.1 above, and Section 3.6.1). The yields are described as:

$$\frac{dN_\gamma}{dp_T}_{incl.} = \frac{1}{a_\gamma(\mathrm{p_T}) \cdot \epsilon_\gamma(\mathrm{p_T}) \cdot \mathrm{c_{conv}}} \cdot (1 - X_{ch}) \cdot (1 - X_{nn}) \frac{dN_{cluster}}{dp_T}. \tag{4.4}$$

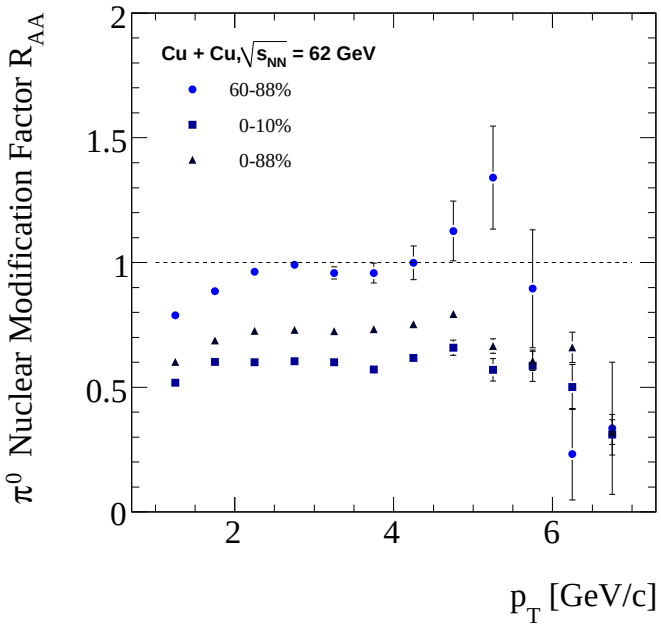

Figure 4.4: Neutral pion Nuclear Modification Factor, R_{AA} in Cu+Cu at $\sqrt{s_{NN}}$ = 62.4 GeV, for three centrality bins of this analysis. R_{AA} can be seen to move away from unity as the centrality increases. The minimum bias bin more closely resembles the central bin, due to it being comprised of mostly central events.

The terms in Equation 4.4, described in Section 3.6.1, are:

- $a_\gamma(\mathrm{p_T})$ is the geometrical acceptance of the EMCal
- $\epsilon_\gamma(\mathrm{p_T})$ is the single–photon reconstruction efficiency
- c_{conv} is the correction for photons which convert to electron pairs before they reach the EMCal (this number is 9.6% for the PbSc and 9.1% for the PbGl) [38]
- X_{ch} is the correction for charged hadrons in the calorimeter
- X_{nn} is the correction for neutron contamination
- $\frac{dN_{cluster}}{dp_T}$ are the raw EMCal clusters

Figure 4.6 shows the fully corrected inclusive photon spectra for the combined EMCal. These spectra represent the total photon production in Cu+Cu at $\sqrt{s_{NN}}$ = 62.4

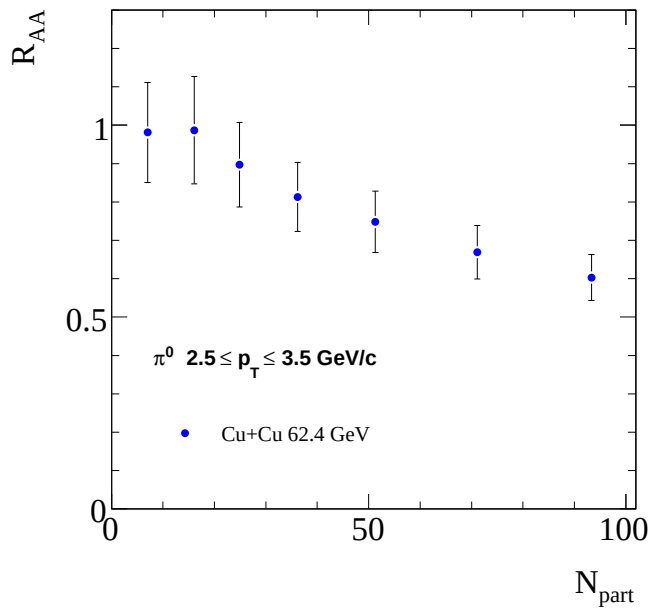

Figure 4.5: Neutral pion R_{AA} plotted versus $N_{\rm part}$ in Cu+Cu at $\sqrt{s_{NN}} = 62.4$ GeV. This integrated R_{AA} illustrates the smooth decline of the nuclear modification with $N_{\rm part}$. Here, R_{AA} was integrated in the p_T region: $2.5 \leq p_T \leq 3.5$ GeV/c.

GeV, including the "feed down" from particles which decay into photons. The minimum bias bin in Figure 4.6 represents more than 126 million events, the seperate centralities are offset by decades from the minimum bias for clarity.

Like the π^0 spectra, the inclusive photons exhibit a steep fall in transverse momentum, with an exponential shape at low p_T and a power law at higher p_T. Power law fits of the type $\frac{1}{p_{\rm T}^n}$ give an n value of ≈ 10.0, similar to that of the π^0. This is as expected, as the inclusive photons are dominated by decay photons from π^0s.

4.2.0.3 Direct Photon Spectra

Following the procedure described in Section 3.6, the direct photon spectra are obtained via the double ratio:

$$R_D = \frac{(\frac{\gamma}{\pi^0})_{meas}}{(\frac{\gamma}{\pi^0})_{sim}}, \tag{4.5}$$

as calculated in Section 3.6.1. The calculation of the direct photon signal (γ_{dir}) is:

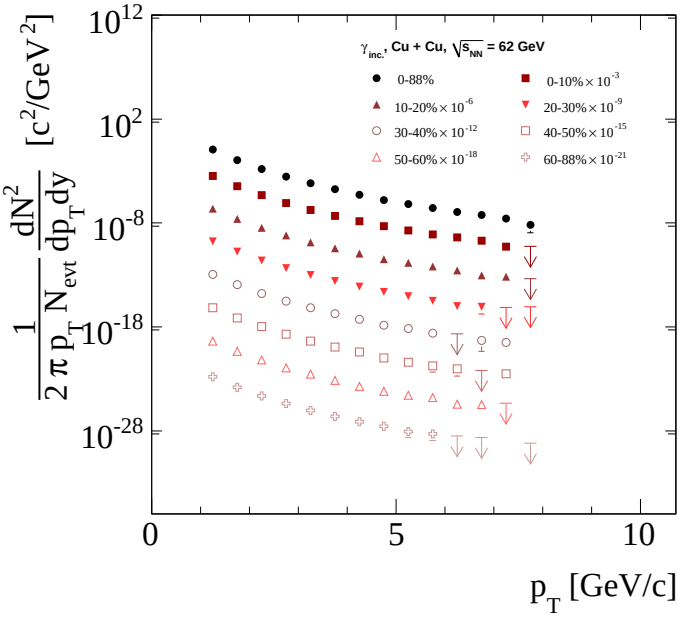

Figure 4.6: Inclusive photon yields in Cu+Cu at $\sqrt{s_{NN}}$ = 62.4 GeV for all centralities in the EMCal. The minimum bias centrality bin represents more than 126 million events. The separate centralities are offset from the minimum bias data by decades for clarity.

$$\gamma_{dir} = (1 - R_D^{-1}) \cdot \gamma_{inc} \tag{4.6}$$

where R_D is the double ratio and γ_{inc} is the inclusive photon yield. The direct photon invariant yields for all centralities are shown in Figure 4.7.

4.2.0.4 Limited Statistics Issue

There is an issue with the analyzed data set that is most apparent in the direct photon spectra presented above. The data suffer from a lack of statistics. In Figure 4.7, the apparent "holes" in the more peripheral centrality bins are the result of the low statistics, though the mininum bias bin does have entries in the transverse momentum range $2.0 \leq p_T \leq 6.0$ GeV/c. The problem is that the statistics begin to run–out right in the region where the direct photon signal starts to appear over the decay photon background. To illustrate this idea, a toy simulation using the ROOT framework was employed. In this "toy" Monte Carlo simulation, π^0s were allowed to decay through their two–photon channel. This decay

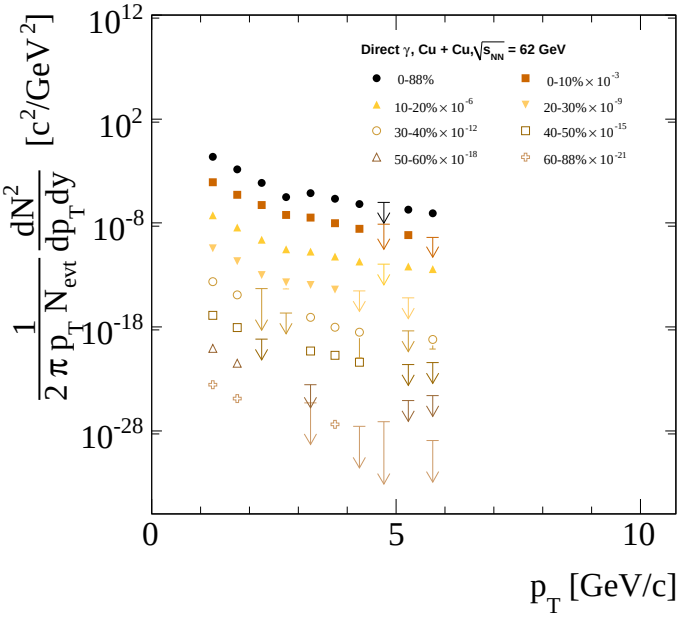

Figure 4.7: Direct photon invariant yields in Cu+Cu at $\sqrt{s_{NN}} = 62.4$ GeV for the combined EMCal. The top spectrum is the minimum bias (all centralities), the individual centralities are offset by decades below for clarity. The error bars represent the statistical and systematic errors summed in quadrature, and the arrows represent data points which can only be statistically described as upper limits.

photon spectrum was then calculated and the ratio $\frac{\gamma}{\pi^0}$ was calculated. This was done for two instances, the first was for a number of events similar to the current data set. The second was done for a number of events three orders of magnitude larger, a similar number that one might find in a typical Au+Au analysis. Figure 4.8 illustrates the results.

It can be seen that the black points fluctuate around the red. This leads to some points falling below the expected decay–only signal. When the double ratio is calculated, the γ to π^0 ratio in the simulation can have as many statistics as the simulation is allowed to run. The data however is another matter. The fluctuating data points in Figure 4.8 lead to instances when the double ratio is near or slightly less than one, and thus the direct photon calculation would give a zero or negative yield, see Equations 4.5 and 4.6. This is what happens in a few centrality and p_T bins, and results in "holes" in the spectra of Figure 4.7.

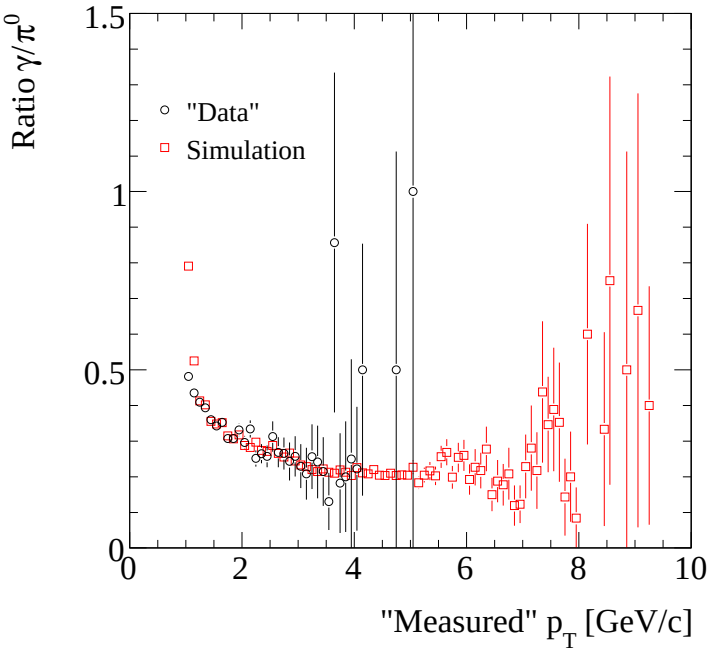

Figure 4.8: illustration of the effect of limited statistics on the double ratio. The limited statistics issue is illustrated here in the black points, representing the number of events in the current analysis. The black points fluctuate around the red.

4.2.0.5 Direct Photon R_{AA}

For the direct photon nuclear modifaction factor R_{AA}, a combined pp reference is used (see the Discussion Section below). Using this reference, R_{AA} was calculated as shown in Figure 4.11, for three different centralities (40–50% (upper left), 30–40% (upper right), 0-10% (lower left), 0-88% (lower right)).

No Suppression While hadron suppression in heavy ion collisions is evident (see above and Figure 4.4 in particular), the direct photon R_{AA} is different. In Figure 4.10, the three centralities shown are all consistent with unity; there is no suppression in even the most central collisions. Photons interact only though the electromagnetic force, and the quark gluon plasma, the medium responsible for hadron suppression, is a strongly interacting medium. Hence photons do not interact with the medium and leave the collision freely. Because the number of participating nucleons in the collision is a good indicator of the geometric volume of the overlap of the ions, plotting R_{AA} against N_{part} nicely illustrates

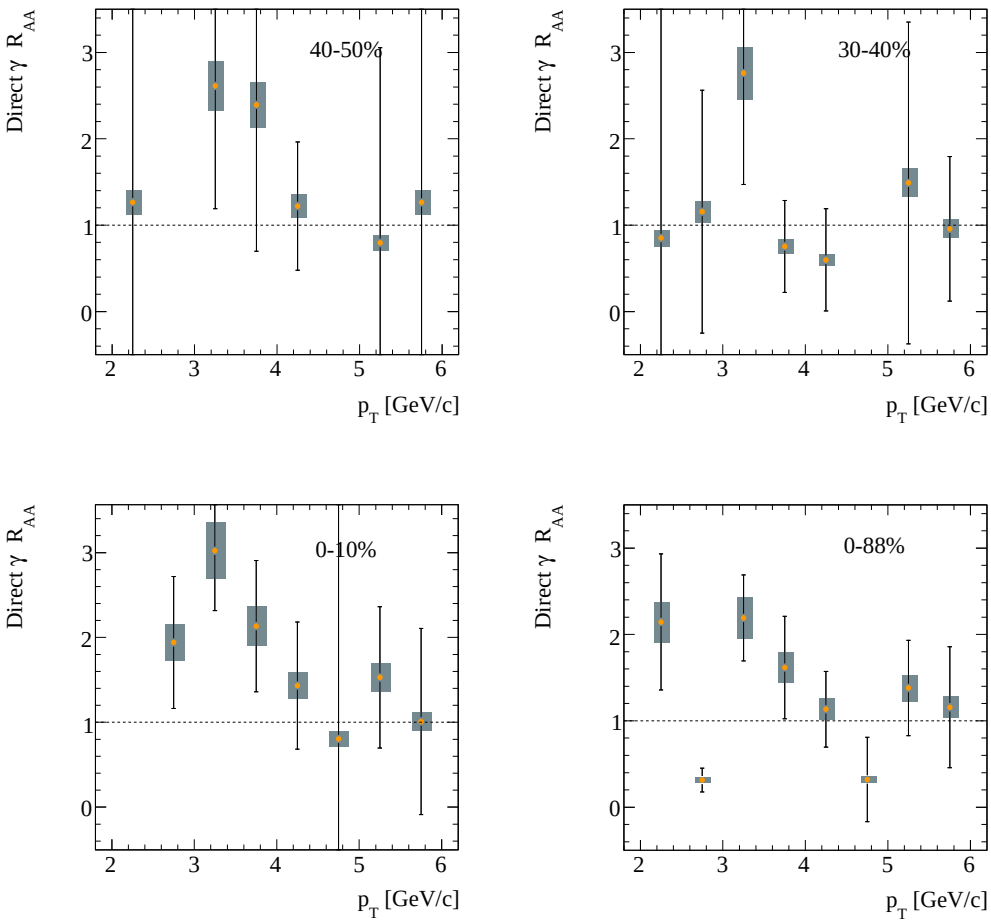

Figure 4.9: Direct photon R_{AA} for three centrality bins 40–50% (upper left), 30–40% (upper right), 0–10% (lower left) and 0-88% (lower right). The error bars denote statistical error and the grey bands represent the systematic error. R_{AA} in all centralities are, within errors, consisitent with unity. Because the photons do not interact with the hot dense medium created in heavy ion collisions, their production is not suppressed, unlike hadrons, for example π^0.

the centrality dependence of the behavior of the nuclear modification factor (see Section 1.2 for a description of the relation of centrality and N_{part}). In Figure 4.11 this dependence is illustrated.

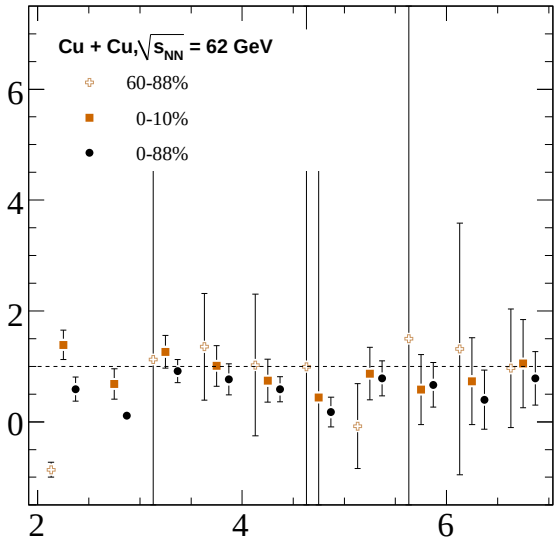

Figure 4.10: Direct photon nuclear modification factor in three centralities, 60–80% (open symbols), 0–10% (squares) and Minimum Bias (circles). Unlike the π^0 R_{AA} , the direct photon R_{AA} does not move away from unity as centrality increases, due to the photons not interacting with the medium created in heavy ion collisions. Note that for clarity, the peripheral points (crosses) have been shifted to slighlty lower p_T and the Minimum Bias points (circles) shifted to higher p_T.

4.3 Discussion

The remainder of the chapter is devoted to how these results compare to other results.

4.3.1 Prior π^0 Results

The π^0 cross–section in this data set has been studied in a previous PHENIX analysis, though not the subsequent inclusive and direct photon production. The comparison of the π^0 results to the previous results provides a cross check of the neutral pion measurement. Figures 4.12 and 4.13 show the ratio of π^0 data: $\frac{former\ analysis}{current\ analysis}$ for cross–section and R_{AA} respectively.

Here the difference between the former and current analysis differs by only 7 %,

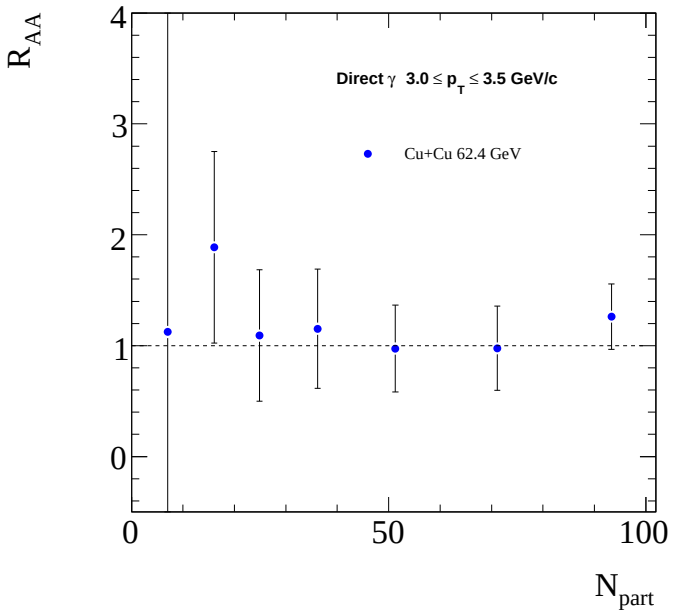

Figure 4.11: Direct photon R_{AA} in Cu+Cu at $\sqrt{s_{NN}}$ = 62.4 GeV plots versus $N_{\rm part}$. R_{AA} agrees with unity for all centralities in copper–copper collisions.

within the systematic uncertainty of the measurements. The comparison can only be made for this central data (0–10%) as this was the only class published (Figure 4.12), whereas all the data are compared for R_{AA} (Figure 4.13), where the previous work is represented as black points and the current as blue points; the red star points are the ratio of the two (see Figure 4.13).

The differences in the two analyses is attributed to a better understanding of photon conversion in the material budget between the collision vertex and the EMCal (hence better π^0 reconstruction) and a fine tuning of the simulation, as compared to the older analysis.

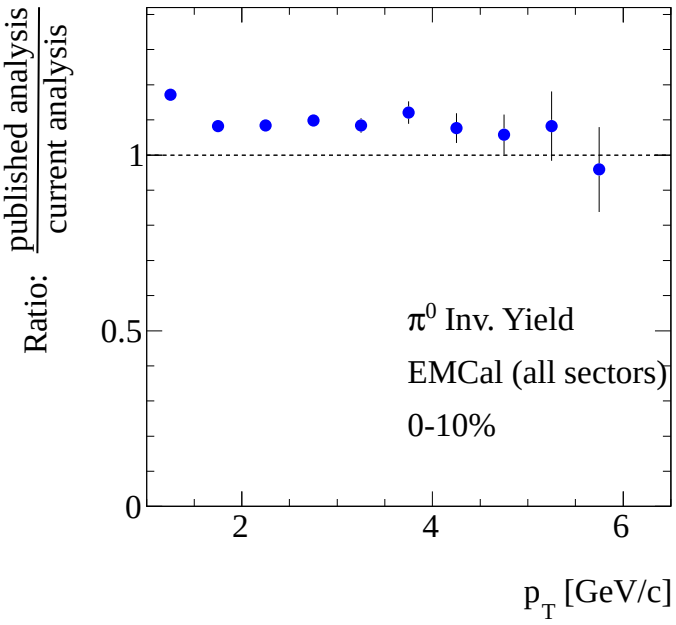

Figure 4.12: Comparison of published π^0 spectra in Cu+Cu at 62.4 GeV to that of the current analysis. Shown is the yield for the combined EMCal in the most central (0–10%) bin. The error bars are statistical only. The two analyses agree to $\sim 7\%$

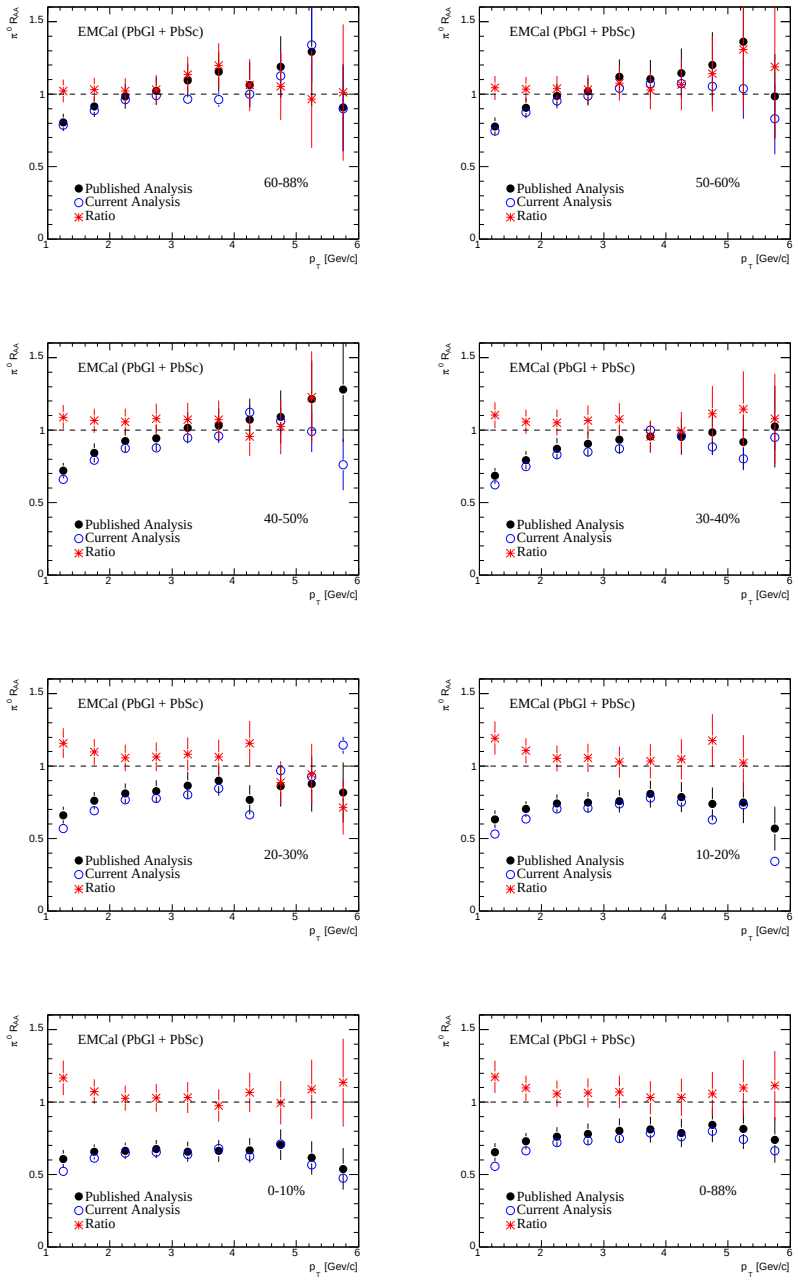

Figure 4.13: A comparison of the published π^0 R_{AA} in Cu+Cu at 62.4 GeV and that calculated in this analysis. In the figure are: published data (black points), current analysis (blue points, and the ratio $\frac{\text{publication}}{\text{current analysis}}$ (red points). The two analyses agree.

4.3.2 System Size dependence of π^0 Cross–Section

The system size dependence is illustrated in Figure 4.14. The Cu+Cu results are shown as red open symbols and the Au+Au are shown as gold closed symbols. Both systems are compared at the same fractional cross–section for 62.4 GeV. The factor of three difference in collision volume ($N_{\rm part}$) of the two systems leads to a remarkably similar shape in the spectra for all centrality classes compared.

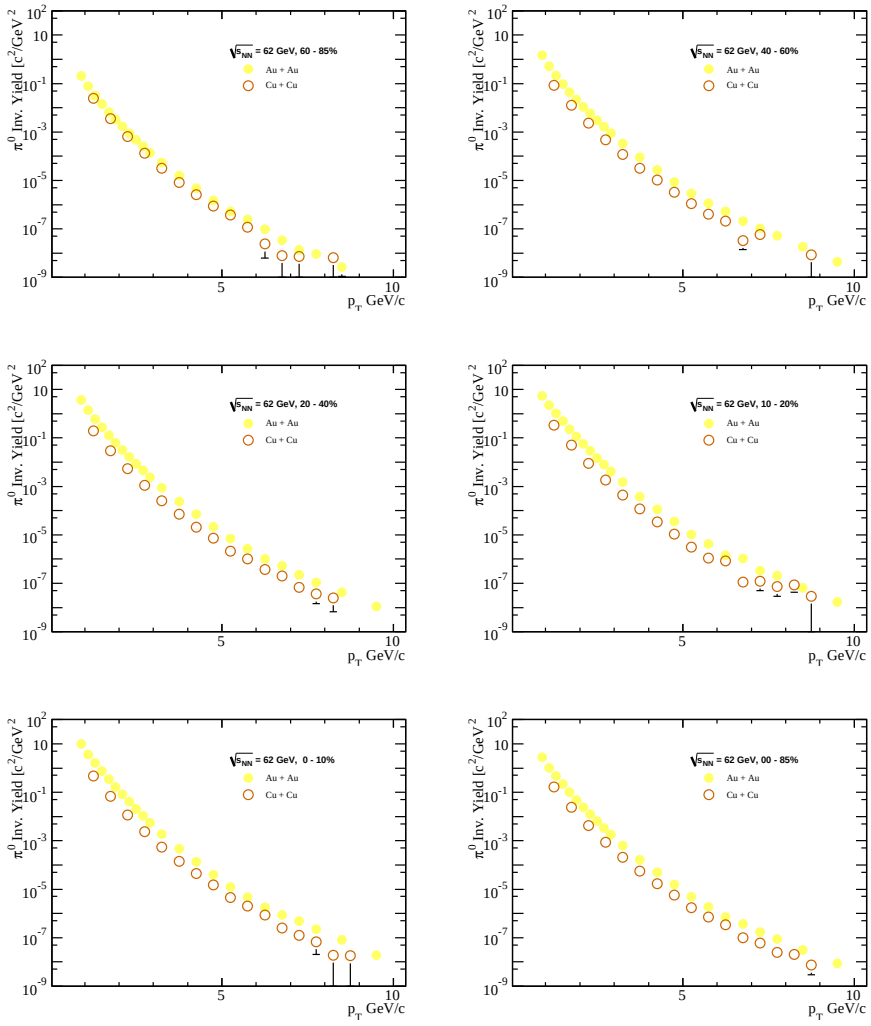

Figure 4.14: π^0 spectra in Cu+Cu and Au+Au, both at $\sqrt{s_{NN}} = 62$ GeV. The centrality bins are, starting on the top/left panel, 60-88%, 40-60%, 20-40%, 10-20%, 0-10%, and the Minimum Bias (0-88%) bin on the bottom right. The Cu+Cu spectra sit slightly below the Au+Au.

As expected, the larger Au+Au system, with more nucleons available to collide, produces more π^0s. It is interesting to note that the shape of the spectra in both systems is roughly the same, particularly in the high p_T region. The power law portions of the spectra have the same shape, suggesting the hard scattering process in Cu+Cu and Au+Au are similar at the same collision energy (see Section 1.2.2).

Another (more precise) way to compare the cross–section is to form ratios. First, we compare the Cu+Cu cross–section to that expected from more elementary collisions (pp) scaled by the expected number of binary nucleon–nucleon collisions in the heavy ion collision (R_{AA}). This nuclear modification factor for neutral pions for different collision species or different collision energies can give insight to the type of matter created in RHIC collisions. That is, the extent to which hadron production is modified depends on the medium in which they are formed. Figure 4.15 shows the p_T distributions of R_{AA} in three different systems: Cu+Cu at $\sqrt{s_{NN}}$ = 62.4 and 200 GeV, and Au+Au at $\sqrt{s_{NN}}$ =200 GeV. The most central collision data is shown in the left panel of the figure, and peripheral collision data is shown in the right panel. The figure illustrates that, in both peripheral and central collisions, the suppression in Cu+Cu is similar for both collision energies. Also, the Au+Au shows significantly more suppression in central collisions. This is due to the much larger volume of matter brought together in the central Au+Au collision, compared to a central Cu+Cu collision.

This trend is further verified in Figure 4.16, where the integrated R_{AA} is shown versus $N_{\rm part}$ for the same three data sets. The left panel of Figure 4.16 shows R_{AA} for the full Au+Au range while the right panel shows a more detailed range for Cu+Cu data. Again, the two Cu+Cu analyses show similar suppression, and both are less suppressed than the π^0 production in Au+Au.

4.3.3 System Size Dependence of Direct Photon Production

It was previously stated that the reference for the direct photon R_{AA} calculation was a fit to a combined pp spectrum. That spectrum and fit is discussed here. Figure 4.17 shows the pp spectra and the corresponding fit function that was used for the R_{AA}.

The following is a description of the fit to two data sets. First, the PHENIX preliminary pp data (blue points in Fig. 4.17) has large, unreasonable (for $p_T > 4$ GeV/c) errors, both statistical and systematic. This issue could not be resolved due to the person(s)

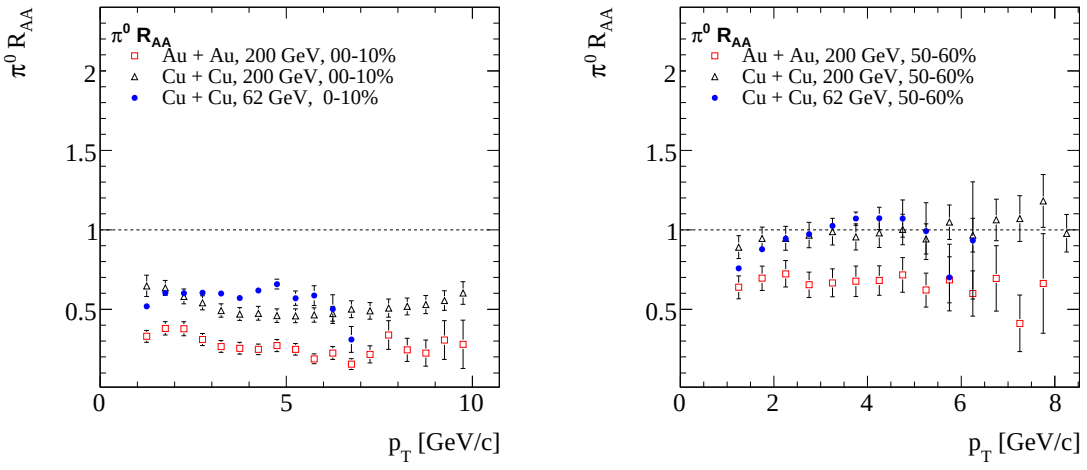

Figure 4.15: Neutral pion R_{AA} in the current analysis (blue) compared to R_{AA} in copper–copper (black) and gold–gold (red) collisions at $\sqrt{s_{NN}} = 200$ GeV. The 62.4 GeV data agree with the 200 GeV copper R_{AA}, while the Au+Au is lower, in both centrality bins.

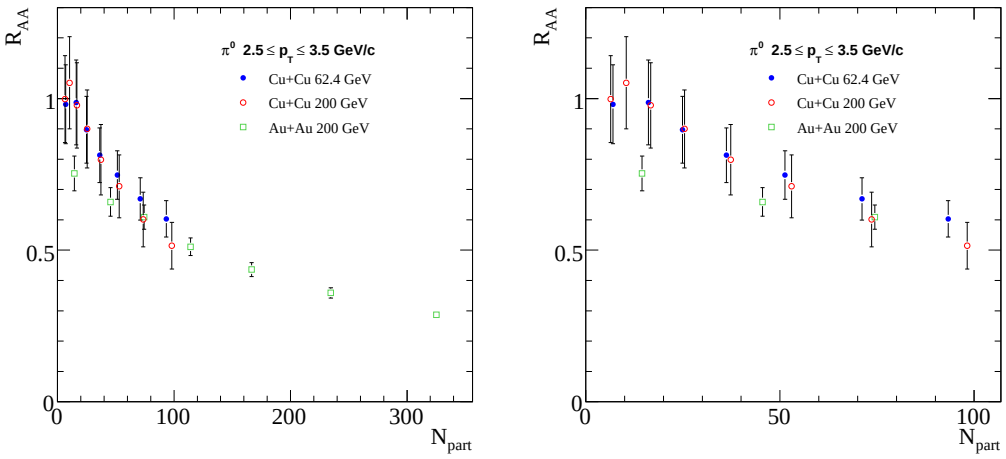

Figure 4.16: Integrated R_{AA} in the transverse momentum region: $2.5 \leq p_T \leq 3.5$ GeV/c for Cu+Cu and Au+Au collisions.

involved in the analysis no longer being in the field. The Data from the ISR[1] [40] (red points) while statistically precise, does not cover the low p_T range where the statistics of the current Cu+Cu analysis dominates. It was reasoned that the combination of these two data sets

[1] ISR was a proton–proton collider set at CERN in the 1980's

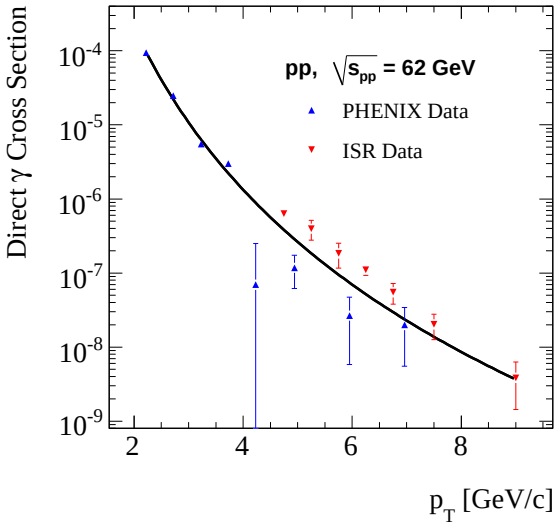

Figure 4.17: Reference fit (black) for direct photon spectra using PHENIX preliminary data (blue) for $p_T < 4$ GeV/c and ISR data for $p_T > 4$ GeV/c (red).

could be used as the *pp* reference, as no other world *pp* data is available at the 62.4 GeV center–of–mass energy needed for this analysis. A fit was made by combining the PHENIX data points for $p_T < 4$ GeV/c and the ISR data points ($p_T > 4$ GeV/c). The deviation of the *pp* data points from PHENIX and ISR to the fit function is shown in Figure 4.18.

The direct photon nuclear modification factor in Cu+Cu at $\sqrt{s_{NN}} = 62.4$ GeV is shown again in Figure 4.19. Also in the figure is the direct photon R_{AA} in Cu+Cu at $\sqrt{s_{NN}}$ =200 GeV and Au+Au at $\sqrt{s_{NN}} = 200$ GeV. In the figure, all three data sets show an R_{AA} value of unity; direct photons are not suppressed in heavy ion collisions with respect to the *pp* reference. No change due to system size (Au+Au versus Cu+Cu) is observed. Also, the differing energy does not effect the results. This supports the expectation that the direct photons will not interact with the created medium, and that the hadron suppression seen is in fact due to the creation of the quark gluon plasma.

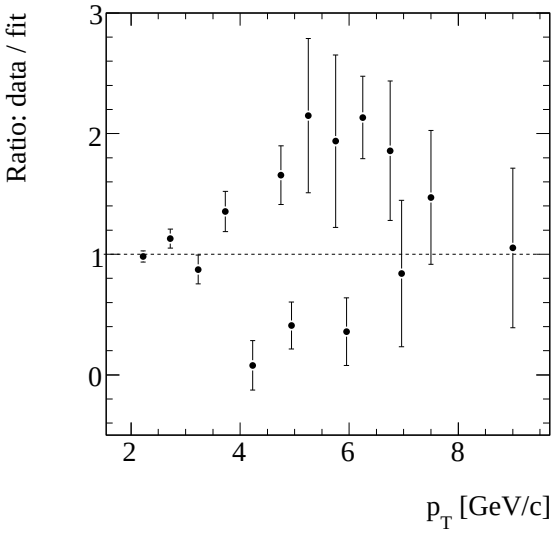

Figure 4.18: Ratio of the *pp* data to the combined fit function from Figure 4.17.

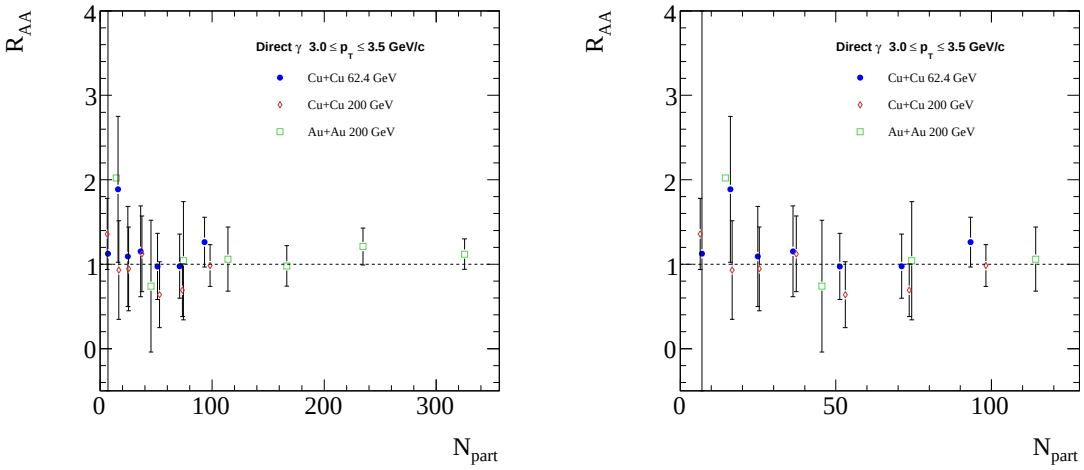

Figure 4.19: Direct photon R_{AA} in three data sets, Cu+Cu at $\sqrt{s_{NN}}$ =62.4 GeV (blue), Cu+Cu at $\sqrt{s_{NN}}$ =200 GeV (red) and Au+Au at $\sqrt{s_{NN}}$ =200 GeV. The figure on the left is on the $N_{\rm part}$ scale of the Au+Au and the right is the Cu+Cu scale. In all data sets, the direct photon R_{AA} can be seen to be at unity.

Chapter 5

Summary

The focus of this work is the detection of neutral pions and a direct photon signal in Cu+Cu collisions at center of mass energy of $\sqrt{s_{NN}}$ = 62.4 GeV. The production of neutral pions were also used to calculate the background to the direct photon spectrum.

The PHENIX experiment was designed and built for the task of detecting the signatures of the quark–gluon plasma, a novel phase of matter very different than that of normal hadronic matter. Thought to exist shortly after the Big Bang, the quark–gluon plasma is expected to be recreated in the laboratory for short periods of time by colliding heavy ions at relativistic energies. Confirmation of the creation of this new form of matter comes from experimental observation of its characteristic signatures in the products of the heavy ion collisions.

Suppression of large transverse–momentum (p_T) particle production in heavy ion collisions, when compared to the expectation of production in scaled pp collisions, is a possible signature of the quark–gluon plasma. Production of these particles stems largely from hard processes, parton–parton interactions with large momentum transfer, leading to parton fragmentation into observable particles. Because these hard scatterings are the same in heavy ion collisions and pp collisions, these produced particles are then ideal probes of the hot dense medium created in central heavy ion collisions. The quark–gluon plasma will have a high color charge density, and this will cause the color–charged partons to lose energy to the medium via the strong interaction. Evidence of these reactions should be seen in high p_T particle suppression.

Hadron suppression has been observed in Au+Au collisions dating back to the first collisions at RHIC. This work, the study of Cu+Cu at $\sqrt{s_{NN}}$ 62.4 GeV attempts to discover

if similar suppression occurs in the smaller system, both in size and energy density. To do so, neutral pions were reconstructed via their two decay photon channel (more than 98% of π^0s decay into two photons) using the PHENIX Electromagnetic Calorimeter(EMCal). This required an accurate energy calibration of the calorimeter. To understand the detector effects on the measurement(s), a Monte Carlo simulation was employed. This simulation provided the corrections needed for the EMCal's limited acceptance and energy resolution. The analysis presented was conducted separately, using the detector's two sub–systems (sampling and Cherenkov calorimeters) as independent detectors, thus providing an internal cross–check of the final, combined, results.

Neutral pion production in central Cu+Cu collisions is seen to be suppressed $\sim$ 40% compared to π^0 yields in *pp* collisions scaled with the corresponding number of binary nucleon–nucleon collisions. In peripheral Cu+Cu collisions however, neutral pion yields are consistent with the scaled *pp* reference. This suppression (in central collisions) is due to parton–parton interaction, as varrified in previous $d + Au$ data from RHIC, where cold nuclear effects were ruled–out as a source of the so called "jet quenching."

Further evidence of the strong interaction with the medium being the source of suppression is found in the direct photon signal. The high–p_T photons, created in the same hard scattering processes as the fragmenting partons, are not subject to the strong interaction. Indeed, as the data shows here, direct photon production is not suppressed with respect to the scaled *pp* production. These particles freely escape the media created in heavy ion collisions, whether it be the quark–gluon plasma, the hadron gas phase, or the mixed phase. Comparisons made here also illustrate direct photon production is not changed due to system size (Cu+Cu versus Au+Au) nor due to collision energy.

RHIC data has shown hadron suppression in heavy ion collisions (compared to that in *pp*) since its first data taking in 2000. Up until these data, the turn–on of this effect has not been seen. It was with this in mind that the Cu+Cu collisions with center of mass energy $\sqrt{s_{NN}} = 62.4$ GeV were examined. For the first time, this analysis shows a direct photon signal in the smaller copper system at the lesser energy (compared to the often analyzed $\sqrt{s_{NN}} = 200$ GeV data). It is found that the production of neutral pions is suppressed in a similar fashion as observed in the larger Au+Au systems. In addition, direct photon production is not affected by the creation of the novel medium in RHIC heavy ion collisions independent of collision size.

Bibliography

[1] W. J. Stirling
"QCD Theory"
arXiv:hep-ph/0411372v1

[2] George Sterman
"QCD Theory at High Energy"
arXiv:hep-ph/0010336v1

[3] A. Ali, G. Kramer
"Jets and QCD: A Historical Review of the Discovery of the Quark and Gluon Jets and its Impact on QCD"
arXiv:1012.2288v2

[4] Alternating Gradient Synchrotron
http://www.bnl.gov/rhic/ags.asp

[5] Brookhaven National Laboratory
http://www.bnl.gov/world/

[6] Super Proton Synchrotron
http://public.web.cern.ch/public/en/research/SPS-en.html

[7] European Organization for Nuclear Research
http://public.web.cern.ch/public/Welcome.html

[8] K. Adcox *et al.*
"Suppression of Hadrons with Large Transverse Momentum in Central Au+Au Collisions at sqrt(s) = 130 GeV"
Phys. Rev. Lett. 88, 022301 (2001)

[9] C. Adler *et al.*
"Disappearance of back-to-back high p_T hadron correlations in central Au + Au collisions at $\sqrt{s_{NN}}$ = 200 GeV"
Phys. Rev. Lett. 90, 82302 (2003)

[10] D. H. Perkins
"Introduction to High Enegry Physics, 4th Ed"
Cambridge, 2000

[11] M. Schmelling
"Status of the strong coupling constant."
In ICHEP 96 : Proceedings,1997, hep-ex/9701002.

[12] K. Johnson
"The m.i.t. bag model"
. Acta Phys. Polon., B6:865, 1975.

[13] S. Ejiri
"Lattice QCD at finite temperature"
arXiv:hep-lat/0011006v2

[14] M. L. Miller *et al.*
"Glauber Modeling in High Energy Nuclear Collisions"
arXiv:nucl-ex/0701025v1

[15] W. Florkowski
"Phenomenology of Ultra-Relativistic Heavy Ion Collisions"
World Scientific, 2010

[16] R. Vogt
" Ultra-Relativistic Heavy Ion Collisions"
Elsevier, 2007

[17] H. Hahn *et al.*
" The RHIC Design Overview"
Nuclear Instruments and Methods in Physics Research Section A: Accelerators, Spectrometers, Detectors and Associated Equipment Volume 499, 1 March 2003

[18] B. B. Back *et al.*
"The PHOBOS detector at RHIC"
Nuclear Instruments and Methods in Physics Research Section A: Accelerators, Spectrometers, Detectors and Associated Equipment Volume 499, 1 March 2003

[19] (M. Adamczyk *et al.*
"The BRAHMS experiment at RHIC"
Nuclear Instruments and Methods in Physics Research Section A: Accelerators, Spectrometers, Detectors and Associated Equipment Volume 499, 1 March 2003

[20] K. H. Ackermann *et al.*
"STAR Detector Overview"
Nuclear Instruments and Methods in Physics Research Section A: Accelerators, Spectrometers, Detectors and Associated Equipment Volume 499, 1 March 2003

[21] K. Adcox *et al.*
"PHENIX Detector Overview"
Nuclear Instruments and Methods in Physics Research Section A: Accelerators, Spectrometers, Detectors and Associated Equipment Volume 499, 1 March 2003

[22] Domenico Elia
"First Results with Heavy-Ion Collisions at LHC from ALICE"
arXiv:1110.1752v1 [nucl-ex]

[23] M. M. Aggarwal *et al.*
"Scaling Properties at Freeze-Out in Relativistic Heavy Ion Collisions"
Phys. Rev. C, 034910 (2011)

[24] M. Del Estal *et al.*
"Nuclear Surface Properties in Relativistic Field Theory"
arXiv:nucl-th/9810026v1

[25] M. Jacob and P. Landshoff
"The Next Generation of Particle Accelerators"
Sci. Am. 242 (1980) 46

[26] S. Mrowczyfiski
"Energy loss of a high-energy parton in the quark-gluon plasma"
Physics Letters B 269 (1991) 383-388

[27] P. Arnold, D. Vaman
"Jet quenching in hot strongly coupled gauge theories simplified"
arXiv:1101.2689v1

[28] J. Nagle *et al.*
"PHENIX Run-5 Copper-Copper 200 GeV Minimum Bias and Centrality Determination"
Internal PHENIX Analysis Note 387

[29] K. Nakamura *et al.*(Particle Data Group)
"The Review of Particle Physics"
J. Phys. G **37**, 075021 (2010)

[30] J. Nagle *et al.*
"PHENIX Run-5 Copper-Copper 62 GeV Minimum Bias and Centrality Determination"
Internal PHENIX Analysis Note 395

[31] B. Sahlmueller *et al.*
"Direct Photon Measurement with the PbGl in $\sqrt{s_{NN}} = 200GeV\,Au + Au$ collisions (Run 04)."
Internal PHENIX Analysis Note 493

[32] N. Novitzky *et al.*
"PHENIX Measurement of pi0 Nuclear Modifications in Run-10 Au+Au Collisions at 39 GeV and 62 GeV"
Internal PHENIX Analysis Note 945

[33] A. Adare *et al.*
"Inclusive cross section and double helicity asymmetry for pi0 production in p+p collisions at sqrt(s)=62.4GeV."
Phys. Rev. Lett. 104, 132301 (2010)

[34] R. Debbe *et al.*
"A Study of Wire Chambers with Highly Segmented Cathode Pad Readout for High Multiplicity Charged Particle Detection" *IEE Transactions On Nuclear Science, Vol. 37, No. 2, April 1990*

[35] K. Adcox *et al.*
"Construction and Performance of the PHENIX Pad Chambers" *Nuclear Instruments and Methods in Physics Research Section A: Accelerators, Spectrometers, Detectors and Associated Equipment, Volume 497, Issues 23, 1 February 2003,*

[36] A. Adare *et al.*
"Onset of pi-zero suppression studied in Cu+Cu collisions at $\sqrt(s_{NN}) = 22.4$, 62.4, and 200 GeV."

[37] C. Klein-Bosing *et al.*
"Centrality dependence of Neutral Pi0 and Eta Production in $\sqrt{s} = 62.4$GeV Cu+Cu Collisions (Run05)."
Internal PHENIX Analysis Note 543

[38] R. Luchtenborg *et al.*
"Direct Photons measured with the PbGl and the PbSc in $\sqrt(s_{NN} = 200$GeV Cu+Cu Collisions (Run05)"
Internal PHENIX Analysis Note 672

[39] C. Klein-Bosing
"Production of Neutral Pions and Direct Photons in Ultra-Relativistic Au + Au Collisions"
Doctoral Thesis

[40] A.L.S. Angelis *et al.*
"Direct Photon Production At The CERN ISR."
Nuc. Phys. B327 (1989)

[41] J. Benjamin *et al.*
"Injecting RHIC From the Brookhaven Tandem Van De Graaff"
Proceedings of the 1999 Particle Accelerator Conference, 1999.

[42] J. Frantz
"Direct Photon Shine: Direct Photon and π^0Production in $\sqrt{s_{NN}} = 200$ GeV $Au+Au$ Collisions"
Doctoral Thesis

[43] L. Aphecetche *et al.*
"PHENIX Calorimeter"
Nuclear Instruments and Methods in Physics Research Section A: Accelerators, Spectrometers, Detectors and Associated Equipment Volume 499, Issues 2-3, 1 March 2003

[44] D. Gabor *et al.*
"The PHENIX lead-scintillator electromagnetic calorimeter: test beam and construction experience "
Transactions on Nuclear Science, Volume: 45, Issue: 3, 06 August 2002

[45] S. Adler *et al.*
"Suppressed π^0 Production at Large Transverse Momentum in Central Au+Au Collisions at $\sqrt{s_{NN}} = 200$ GeV"
Phys. Rev. Lett. 91, 072301 (2003)

[46] J. Adams *et al.*
"Transverse–Momentum and Collision–Energy Dependence of High-p_T Hadron Suppression in Au+Au Collisions at Ultra relativistic Energies"
Phys. Rev. Lett. 91, 172302 (2003)

[47] B. Alver *et al.*
"System Size and Centrality Dependence of Charged hadron Transverse Momentum Spectra in Au+Au and Cu+Cu Collisions at $\sqrt{s_{NN}} = 62.4$ and 200 GeV"
Phys. Rev. Lett. 96, 212301 (2006)

Appendix A

Various Ratios

There were several quantities shown in previous chapters that have different values for different centralies as well as differences in PbSc versus PbGl. Values (γ_{inc} /pI ratios, double ratios, —R_{AA} plots) were shown previously for only one centrality and/or EMCal sub–detector. These quantities are shown here completely for all centrality and both sub–detectors.

First, the ratio of π^0 yields in PbSc / PbGl. As described in the text (see Section **??**), the two detectors agree within two sigma.

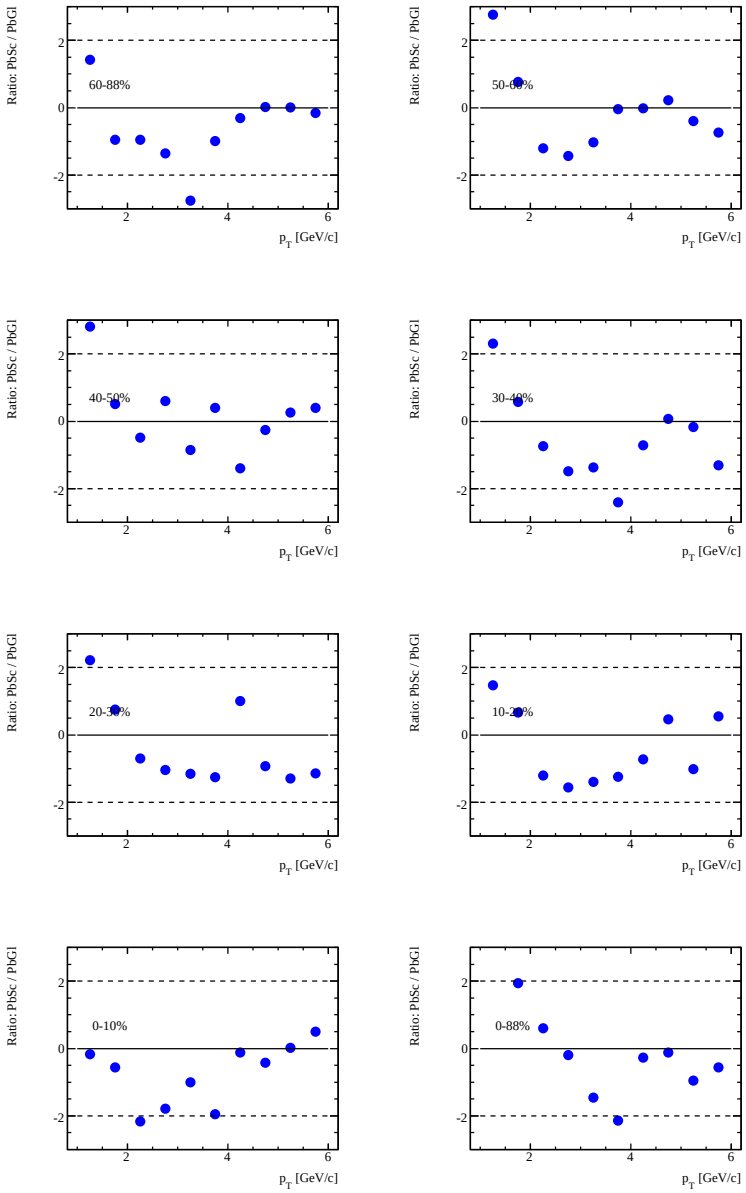

Figure A.1: Ratio of π^0 yields as calculated in PbSc versus those calculated in PbGl. The two detecors agree within 2 sigma (dashed lines).

A.1 γ_{inc} / π^0 Ratios

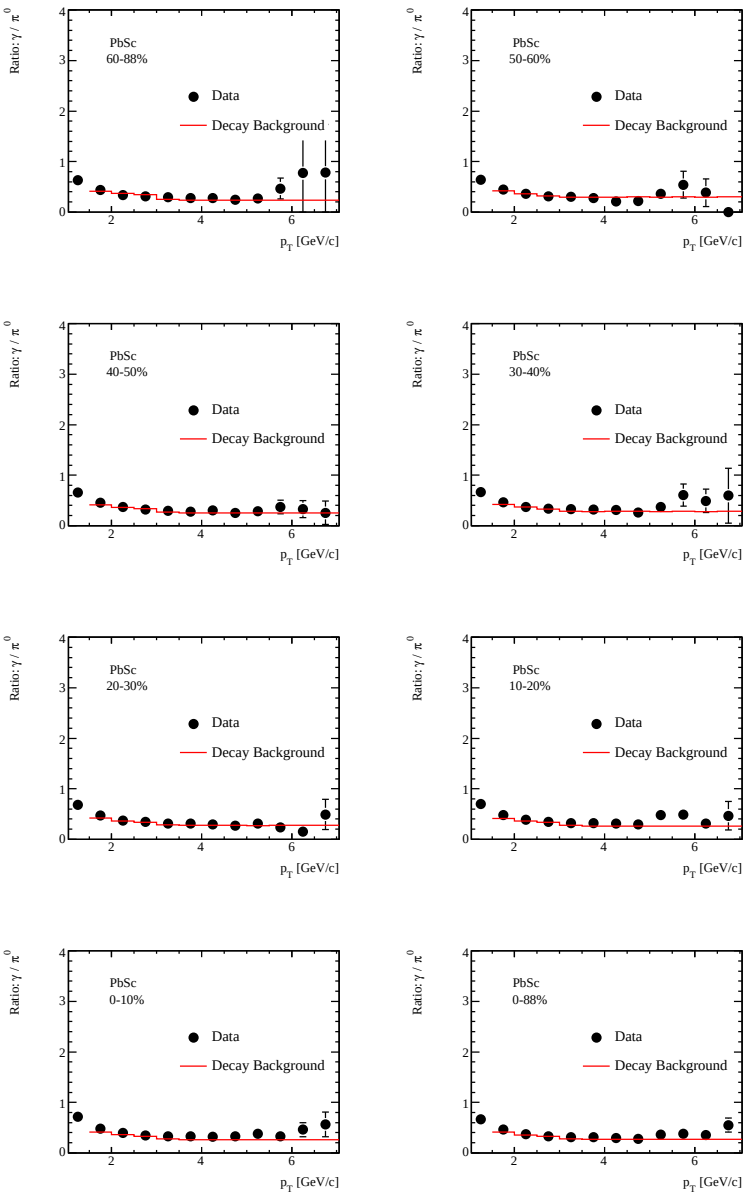

Figure A.2: γ/π^0 in the PbSc, for all centralities. In the figure, data are black and the decay background from simulation is red. The bars represent the statistical error and the bands the systematic error.

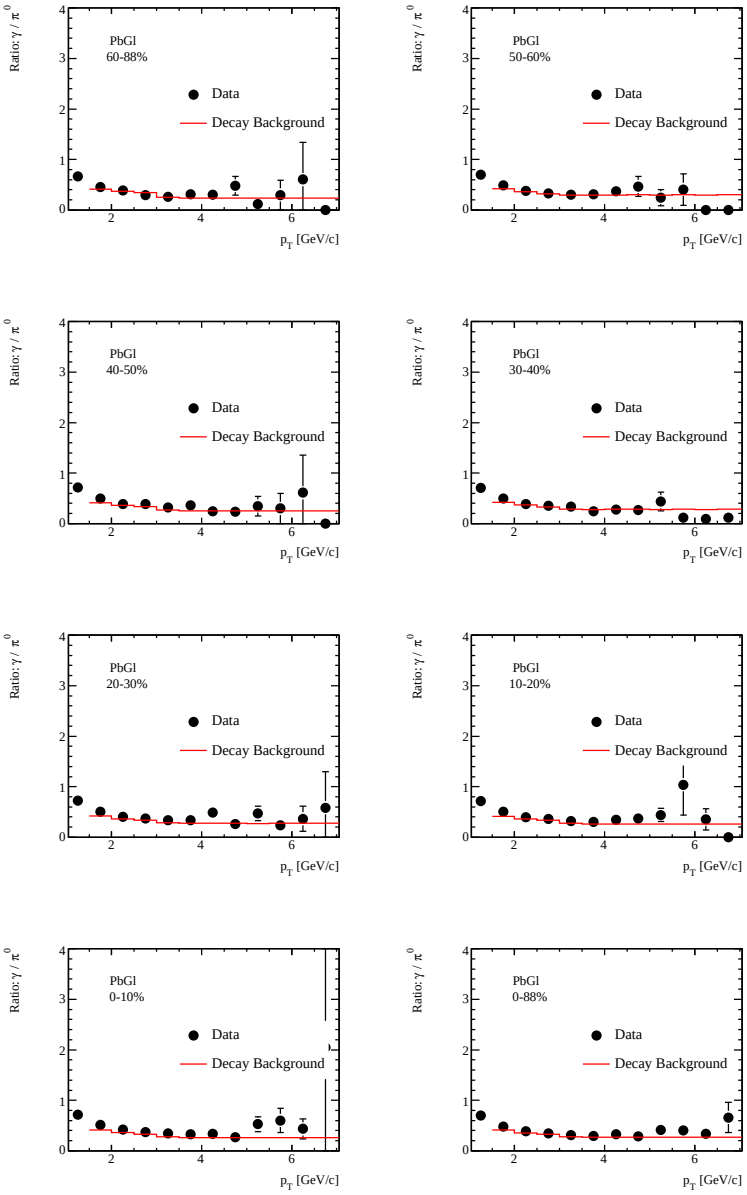

Figure A.3: γ/π^0 in the PbGl, for all centralities. In the figure, data are black and the decay background from simulation is red. The bars represent the statistical error and the bands the systematic error.

A.2 Double Ratios

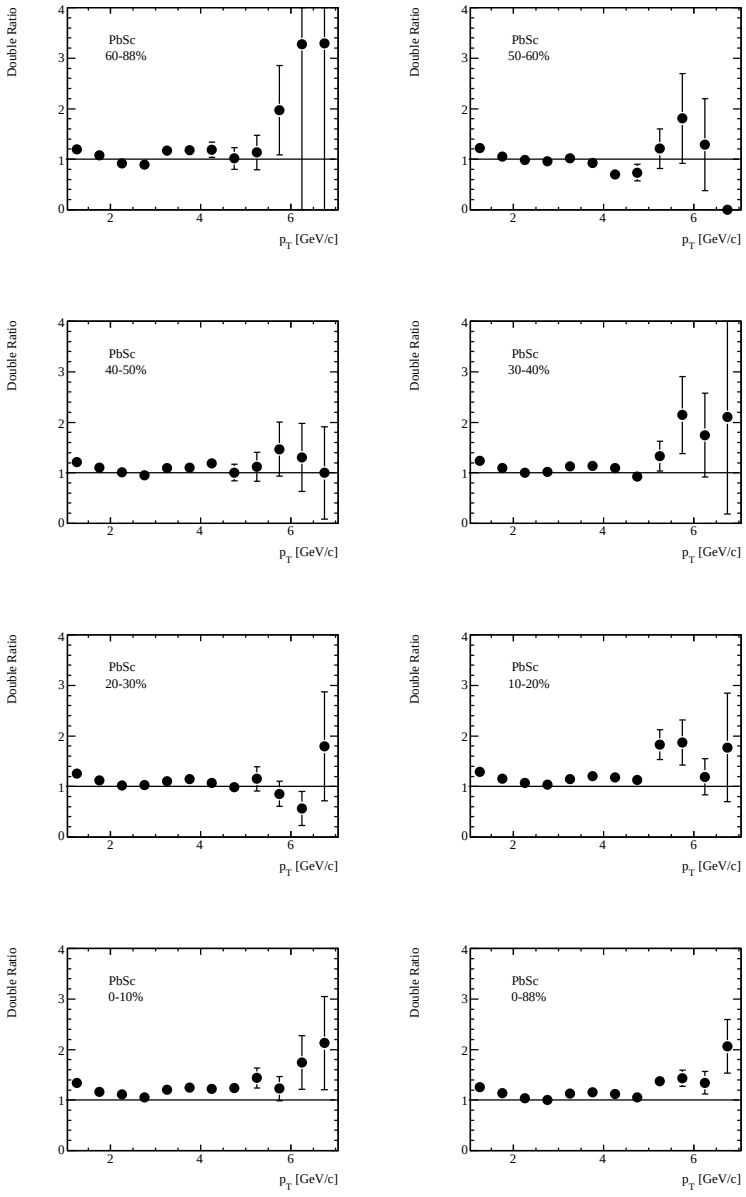

Figure A.4: Double Ratio in PbSc for all centrality classes.

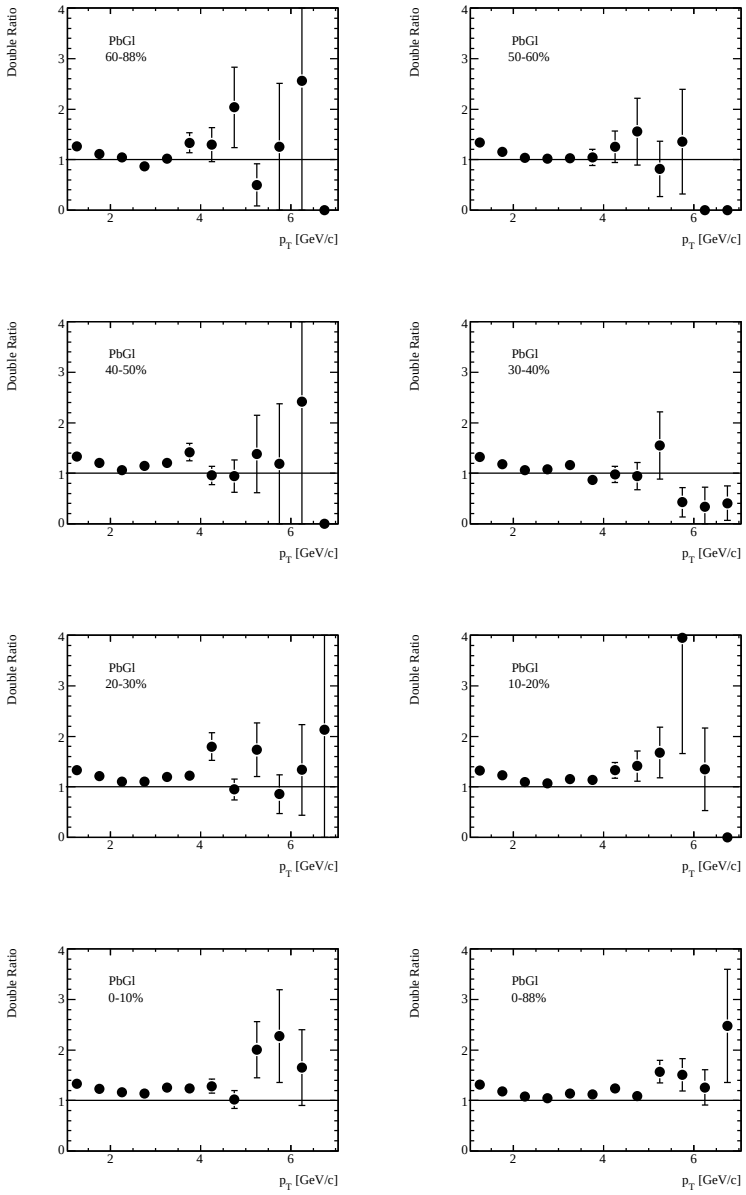

Figure A.5: Double Ratio in PbGl for all centrality classes.

A.3 Direct Photon R_{AA}

The direct photon R_{AA} is calculated for the whole EMCal.

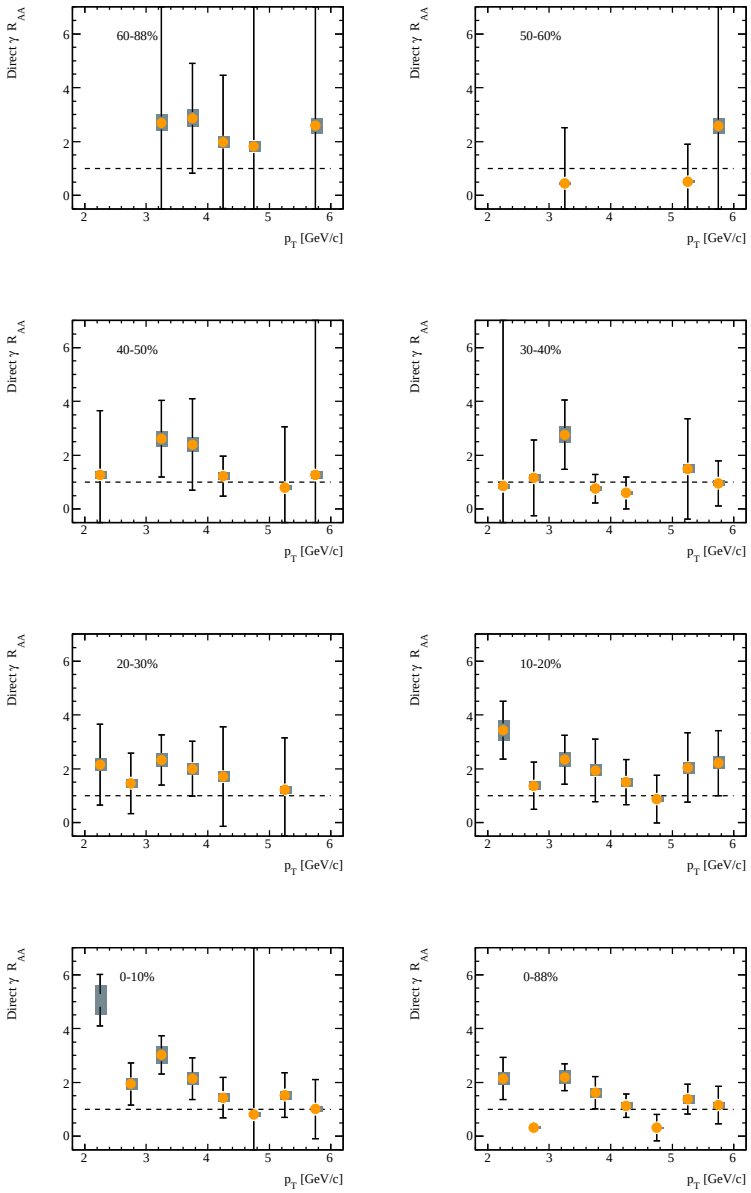

Figure A.6: Direct photon R_{AA} for all centralities

Appendix B

Data Tables

p_T	yield	error
1.25	0.165797	0.00154513
1.75	0.0242242	0.000228516
2.25	0.00427677	3.8388e-05
2.75	0.000882888	8.70257e-06
3.25	0.000208007	2.39788e-06
3.75	5.62799e-05	8.62925e-07
4.25	1.69511e-05	3.58972e-07
4.75	5.68927e-06	1.79089e-07
5.25	1.72708e-06	8.75246e-08
5.75	7.12631e-07	5.27202e-08
6.25	3.34101e-07	3.45693e-08
6.75	9.90329e-08	1.78394e-08
7.25	6.08744e-08	1.36157e-08
7.75	2.43415e-08	8.85717e-09
8.25	1.99019e-08	7.21926e-09
8.75	7.3507e-09	4.36913e-09

Table B.1: π^0 yields in Cu+Cu 62.4 GeV, 0–88%

p_T	yield	error
1.25	0.466622	0.00590357
1.75	0.0684382	0.000879423
2.25	0.0114815	0.000133999
2.75	0.00236775	3.43549e-05
3.25	0.000547488	1.06121e-05
3.75	0.000141953	4.02928e-06
4.25	4.40639e-05	1.74926e-06
4.75	1.523e-05	8.31756e-07
5.25	4.4839e-06	4.19894e-07
5.75	2.00217e-06	2.55914e-07
6.25	8.72599e-07	1.71109e-07
6.75	2.48914e-07	8.02895e-08
7.25	1.22777e-07	5.65289e-08
7.75	6.82167e-08	4.82419e-08
8.25	1.8987e-08	1.89879e-08
8.75	1.78359e-08	1.78369e-08

Table B.2: π^0 yields in Cu+Cu 62.4 GeV, 0–10%

p_T	yield	error
1.25	0.342042	0.00420852
1.75	0.050723	0.000671455
2.25	0.00887001	0.000101499
2.75	0.00179294	2.58675e-05
3.25	0.000431858	8.44189e-06
3.75	0.000119024	3.2907e-06
4.25	3.46418e-05	1.40335e-06
4.75	1.05404e-05	6.83264e-07
5.25	3.12338e-06	3.53209e-07
5.75	1.08439e-06	1.92839e-07
6.25	8.22226e-07	1.55841e-07
6.75	1.14199e-07	5.10843e-08
7.25	1.20304e-07	6.96838e-08
7.75	7.31666e-08	4.36353e-08
8.25	8.67569e-08	4.46395e-08
8.75	2.918e-08	2.91816e-08

Table B.3: π^0 yields in Cu+Cu 62.4 GeV, 10–20%

p_T	yield	error
1.25	0.238158	0.00290801
1.75	0.0353811	0.000468122
2.25	0.00629947	7.41327e-05
2.75	0.00128436	1.89978e-05
3.25	0.000306027	6.33106e-06
3.75	8.32483e-05	2.51613e-06
4.25	2.29204e-05	1.08407e-06
4.75	8.67736e-06	6.12017e-07
5.25	2.44215e-06	3.11663e-07
5.75	1.33289e-06	2.14374e-07
6.25	4.11711e-07	1.14797e-07
6.75	1.63942e-07	7.03262e-08
7.25	7.7944e-08	4.66003e-08
7.75	3.34643e-08	3.34662e-08
8.25	4.93549e-08	3.59762e-08

Table B.4: π^0 yields in Cu+Cu 62.4 GeV, 20–30%

p_T	yield	error
1.25	0.161266	0.00200927
1.75	0.0239608	0.000300965
2.25	0.00431506	5.16129e-05
2.75	0.00088732	1.39502e-05
3.25	0.000211596	4.71796e-06
3.75	6.0508e-05	2.03945e-06
4.25	1.83165e-05	9.5861e-07
4.75	5.66298e-06	4.80018e-07
5.25	1.72019e-06	2.54494e-07
5.75	6.79797e-07	1.58264e-07
6.25	3.21117e-07	1.00485e-07
6.75	2.4021e-07	9.29863e-08
7.25	5.65565e-08	4.1375e-08
7.75	3.90483e-08	2.76142e-08

Table B.5: π^0 yields in Cu+Cu 62.4 GeV, 30–40%

p_T	yield	error
1.25	0.103961	0.00130529
1.75	0.0155297	0.000214351
2.25	0.00282878	3.51208e-05
2.75	0.000582357	9.91279e-06
3.25	0.000145908	3.66129e-06
3.75	3.95427e-05	1.58374e-06
4.25	1.33535e-05	8.05638e-07
4.75	4.13159e-06	4.14402e-07
5.25	1.36872e-06	2.17954e-07
5.75	4.89636e-07	1.2167e-07
6.25	2.35775e-07	8.04418e-08
6.75	6.68776e-08	3.86177e-08
7.25	7.70763e-08	4.61513e-08

Table B.6: π^0 yields in Cu+Cu 62.4 GeV, 40–50%

p_T	yield	error
1.25	0.065154	0.000811332
1.75	0.00967339	0.000138126
2.25	0.00176078	2.37135e-05
2.75	0.000374129	7.0214e-06
3.25	9.26705e-05	2.66958e-06
3.75	2.48954e-05	1.17519e-06
4.25	7.48158e-06	5.86949e-07
4.75	2.32437e-06	3.06065e-07
5.25	8.28687e-07	1.7332e-07
5.75	3.22916e-07	1.05959e-07
6.25	1.80545e-07	7.65464e-08
6.75	–	–
7.25	4.13541e-08	2.92448e-08
7.75	–	–
8.25	–	–
8.75	1.70612e-08	1.70621e-08

Table B.7: π^0 yields in Cu+Cu 62.4 GeV, 50–60%

p_T	yield	error
.25	0.0245827	0.000264052
1.75	0.00353952	4.0767e-05
2.25	0.000638293	7.97569e-06
2.75	0.000135738	2.41507e-06
3.25	3.24163e-05	9.25912e-07
3.75	8.30978e-06	4.04772e-07
4.25	2.5441e-06	2.04083e-07
4.75	8.92755e-07	1.13306e-07
5.25	3.70227e-07	6.80725e-08
5.75	1.17976e-07	3.67864e-08
6.25	2.38537e-08	1.75193e-08
6.75	7.92041e-09	7.92082e-09
7.25	7.34655e-09	7.34693e-09
7.75	–	–
8.25	6.4717e-09	6.47203e-09

Table B.8: π^0 yields in Cu+Cu 62.4 GeV, 60–88%

p_T	yield	error
1.25	0.112031	0.0003589
1.75	0.0113558	3.95863e-05
2.25	0.00159161	7.38154e-06
2.75	0.000292188	2.25612e-06
3.25	6.50345e-05	9.10598e-07
3.75	1.71701e-05	4.30282e-07
4.25	5.18376e-06	2.19701e-07
4.75	1.60592e-06	1.17407e-07
5.25	6.5265e-07	6.7564e-08
5.75	2.75525e-07	4.28439e-08
6.25	1.16512e-07	2.59518e-08
6.75	5.78116e-08	1.72988e-08
7.25	2.69315e-08	1.97625e-08
7.75	6.69104e-09	5.59817e-09
8.25	5.53366e-09	4.79232e-09
8.75	1.81116e-09	2.56137e-09
9.25	5.52132e-09	5.96374e-09
9.75	7.20428e-10	9.60572e-10

Table B.9: γ_{inc} yields in Cu+Cu 62.4 GeV, 0–88%

p_T	yield	error
1.25	0.335	0.00111165
1.75	0.0335246	0.000137451
2.25	0.00463624	3.13784e-05
2.75	0.000829628	1.07407e-05
3.25	0.000182399	4.51432e-06
3.75	4.66808e-05	2.09606e-06
4.25	1.43457e-05	1.12256e-06
4.75	4.74769e-06	6.39041e-07
5.25	1.86449e-06	3.43485e-07
5.75	7.66781e-07	2.07244e-07
6.25	3.92639e-07	1.37896e-07
6.75	1.99074e-07	9.33294e-08
7.25	5.06307e-08	2.75601e-08
7.75	2.60708e-08	3.19301e-08
8.25	7.54097e-09	1.00546e-08
8.75	–	–
9.25	1.55435e-08	2.19818e-08
9.75	6.43731e-09	8.58309e-09

Table B.10: γ_{inc} yields in Cu+Cu 62.4 GeV, 0–10%

p_T	yield	error
1.25	0.240192	0.000812931
1.75	0.0246136	0.000108335
2.25	0.0034303	2.63234e-05
2.75	0.000626112	9.2916e-06
3.25	0.000136554	3.8921e-06
3.75	3.70448e-05	1.91581e-06
4.25	1.10603e-05	9.45295e-07
4.75	3.31337e-06	4.9844e-07
5.25	1.45068e-06	3.02577e-07
5.75	6.44889e-07	1.8947e-07
6.25	2.65113e-07	1.23406e-07
6.75	8.78289e-08	6.21051e-08
7.25	6.61182e-08	3.11687e-08
7.75	1.78688e-08	2.52703e-08
8.25	–	–
8.75	–	–
9.25	1.33005e-08	1.25399e-08

Table B.11: γ_{inc} yields in Cu+Cu 62.4 GeV, 10–20%

p_T	yield	error
1.25	0.164289	0.000573374
1.75	0.016941	8.23394e-05
2.25	0.0023982	2.13015e-05
2.75	0.000447245	7.79823e-06
3.25	9.77522e-05	3.2247e-06
3.75	2.66051e-05	1.56322e-06
4.25	7.70575e-06	7.63628e-07
4.75	2.31699e-06	4.0873e-07
5.25	9.08541e-07	2.1733e-07
5.75	3.11868e-07	1.26202e-07
6.25	9.9261e-08	6.6587e-08
6.75	8.42092e-08	6.75181e-08
7.25	3.51513e-08	4.05894e-08
7.75	7.67171e-09	1.0229e-08
8.25	9.59649e-09	3.83861e-08
8.75	1.59155e-08	2.2508e-08

Table B.12: γ_{inc} yields in Cu+Cu 62.4 GeV, 20–30%

p_T	yield	error
1.25	0.108578	0.000396299
1.75	0.0112555	6.21224e-05
2.25	0.00160351	1.70871e-05
2.75	0.000302457	6.33343e-06
3.25	6.9133e-05	2.71448e-06
3.75	1.79391e-05	1.33679e-06
4.25	5.47475e-06	6.92302e-07
4.75	1.48224e-06	3.40159e-07
5.25	6.69792e-07	2.06713e-07
5.75	2.54911e-07	1.57336e-07
6.25	1.07379e-07	1.1262e-07
6.75	4.90206e-08	4.47497e-08
7.25	3.3031e-08	2.20207e-08
7.75	–	–
8.25	7.38846e-09	9.85129e-09
8.75	–	–
9.25	6.63624e-09	8.84833e-09

Table B.13: γ_{inc} yields in Cu+Cu 62.4 GeV, 30–40%

p_T	yield	error
1.25	0.0695664	0.00027146
1.75	0.00726692	4.71108e-05
2.25	0.0010496	1.36975e-05
2.75	0.000196487	5.11823e-06
3.25	4.4088e-05	2.19143e-06
3.75	1.1792e-05	1.05249e-06
4.25	3.77395e-06	5.79161e-07
4.75	1.03527e-06	2.88508e-07
5.25	4.06308e-07	1.71701e-07
5.75	1.75297e-07	1.3196e-07
6.25	8.94669e-08	7.17336e-08
6.75	2.89313e-08	3.54336e-08
7.25	3.15786e-08	2.10525e-08
7.75	–	–
8.25	1.70664e-08	2.41355e-08

Table B.14: γ_{inc} yields in Cu+Cu 62.4 GeV, 40–50%

p_T	yield	error
1.25	0.0426505	0.000184209
1.75	0.00439291	3.46817e-05
2.25	0.000641773	1.05337e-05
2.75	0.000117096	3.91165e-06
3.25	2.77321e-05	1.77015e-06
3.75	7.092e-06	8.35809e-07
4.25	1.87623e-06	3.67055e-07
4.75	6.41949e-07	1.99913e-07
5.25	2.684e-07	1.47655e-07
5.75	1.55894e-07	9.22292e-08
6.25	3.70299e-08	2.46867e-08
6.75	3.44561e-08	2.29708e-08
7.25	1.93181e-08	2.73199e-08

Table B.15: γ_{inc} yields in Cu+Cu 62.4 GeV, 50–60%

p_T	yield	error
1.25	0.015631	6.71736e-05
1.75	0.00156889	1.24347e-05
2.25	0.000223554	3.7135e-06
2.75	4.13179e-05	1.38103e-06
3.25	9.27719e-06	6.06176e-07
3.75	2.39654e-06	2.77725e-07
4.25	7.31743e-07	1.48666e-07
4.75	2.67999e-07	7.66877e-08
5.25	8.48999e-08	6.31145e-08
5.75	4.92675e-08	3.78725e-08
6.25	1.58319e-08	1.58319e-08
6.75	1.04548e-08	1.28045e-08
7.25	–	–
7.75	2.70161e-09	3.60215e-09
8.25	2.57353e-09	3.43138e-09
8.75	–	–
9.25	4.6171e-09	4.35305e-09

Table B.16: γ_{inc} yields in Cu+Cu 62.4 GeV, 60–88%

p_T	yield	error
1.25	1.26969	0.0238789
1.75	1.14372	0.0225739
2.25	1.0459	0.0194469
2.75	1.01044	0.0227997
3.25	1.12932	0.0333896
3.75	1.14775	0.0492107
4.25	1.15005	0.080481
4.75	1.0595	0.115835
5.25	1.41996	0.247522
5.75	1.44902	0.359377
6.25	1.32144	0.414717
6.75	2.16419	1.24077

Table B.17: Double Ratio in Cu+Cu 62.4 GeV, 0–88%

p_T	yield	error
1.25	1.33602	0.0379904
1.75	1.1824	0.0299725
2.25	1.12554	0.0311673
2.75	1.07574	0.0415952
3.25	1.21686	0.066487
3.75	1.24614	0.0996285
4.25	1.23348	0.156794
4.75	1.1819	0.205208
5.25	1.58132	0.588801
5.75	1.48906	0.950861
6.25	1.72062	0.920558
6.75	3.5266	8.30978

Table B.18: Double Ratio in Cu+Cu 62.4 GeV, 0–10%

p_T	yield	error
1.25	1.29584	0.0357203
1.75	1.1736	0.0357837
2.25	1.07671	0.0291238
2.75	1.04795	0.0400742
3.25	1.14611	0.0643287
3.75	1.18639	0.0956548
4.25	1.21422	0.170188
4.75	1.20098	0.317334
5.25	1.78789	0.579216
5.75	2.39056	2.33606
6.25	1.22984	0.893155
6.75	1.07359	1.07359

Table B.19: Double Ratio in Cu+Cu 62.4 GeV, 10–20%

p_T	yield	error
1.25	1.27385	0.0364472
1.75	1.14011	0.0366158
2.25	1.04238	0.0298861
2.75	1.04577	0.0431693
3.25	1.1274	0.0717132
3.75	1.16642	0.111157
4.25	1.25142	0.282011
4.75	0.975742	0.235078
5.25	1.29746	0.582386
5.75	0.853226	0.458462
6.25	0.759508	0.958736
6.75	1.87631	2.82271

Table B.20: Double Ratio in Cu+Cu 62.4 GeV, 20–30%

p_T	yield	error
1.25	1.25554	0.0352966
1.75	1.11573	0.0303163
2.25	1.01524	0.0303374
2.75	1.03306	0.0453993
3.25	1.13667	0.077369
3.75	1.06771	0.100662
4.25	1.06455	0.183773
4.75	0.927753	0.301591
5.25	1.38401	0.72589
5.75	1.71518	0.819755
6.25	1.39514	0.916337
6.75	1.67942	1.95043

Table B.21: Double Ratio in Cu+Cu 62.4 GeV, 30–40%

p_T	yield	error
1.25	1.23926	0.0361765
1.75	1.13149	0.0373345
2.25	1.02176	0.0327965
2.75	0.998553	0.0550094
3.25	1.12269	0.0937566
3.75	1.1816	0.187009
4.25	1.13195	0.213215
4.75	0.990635	0.361834
5.25	1.18552	0.819163
5.75	1.39657	1.30155
6.25	1.5827	3.03902
6.75	0.912754	0.912754

Table B.22: Double Ratio in Cu+Cu 62.4 GeV, 40–50%

p_T	yield	error
1.25	1.25007	0.0369747
1.75	1.0786	0.0380253
2.25	0.997135	0.0363856
2.75	0.975758	0.0565526
3.25	1.01738	0.0967409
3.75	0.957857	0.174959
4.25	0.84079	0.329474
4.75	0.940095	0.681307
5.25	1.11229	0.673777
5.75	1.69554	1.3675
6.25	0.911172	0.911172

Table B.23: Double Ratio in Cu+Cu 62.4 GeV, 50–60%

p_T	yield	error
1.25	1.21247	0.0272758
1.75	1.08601	0.026868
2.25	0.950914	0.0338014
2.75	0.886511	0.0477184
3.25	1.13068	0.0988528
3.75	1.21531	0.218803
4.25	1.21773	0.370585
4.75	1.27205	0.822584
5.25	0.975231	0.539745
5.75	1.79014	1.53441
6.25	3.09851	5.0932
6.75	4.03354	4.03354

Table B.24: Double Ratio in Cu+Cu 62.4 GeV, 60–88%

p_T	yield	error
1.25	0.0237101	0.00154604
1.75	0.00142338	0.000177574
2.25	6.96877e-05	2.55927e-05
2.75	3.0332e-06	1.33604e-06
3.25	7.45231e-06	1.6914e-06
3.75	2.19948e-06	8.08115e-07
4.25	6.77928e-07	2.6155e-07
4.75	9.02944e-08	1.37783e-07
5.25	1.95072e-07	7.79589e-08
5.75	8.56722e-08	5.18492e-08
6.25	2.7821e-08	3.73197e-08
6.75	3.14094e-08	1.93269e-08
7.25	1.07146e-08	5.53006e-09
7.75	2.01319e-10	2.33617e-09
8.25	2.43305e-10	2.00562e-09

Table B.25: Direct Photon Yield Cu+Cu 62.4 GeV, 0–88%

p_T	yield	error
1.25	0.0842519	0.00731871
1.75	0.00517763	0.000660123
2.25	0.000520013	9.85879e-05
2.75	5.93999e-05	2.38272e-05
3.25	3.25847e-05	7.60765e-06
3.75	9.20728e-06	3.33768e-06
4.25	2.71709e-06	1.42038e-06
4.75	7.19492e-07	6.78657e-06
5.25	6.85017e-07	3.73371e-07
5.75	2.37201e-07	2.57652e-07
6.25	1.62656e-07	1.74019e-07
6.75	1.33189e-07	1.0074e-07
7.25	1.81568e-08	2.36082e-08
7.75	0	0
8.25	2.52992e-09	9.05426e-09

Table B.26: Direct Photon Yield Cu+Cu 62.4 GeV, 0–10%

p_T	yield	error
1.25	0.0547874	0.00484171
1.75	0.00363433	0.00054544
2.25	0.000244992	7.6622e-05
2.75	2.89195e-05	1.85861e-05
3.25	1.74199e-05	6.78053e-06
3.75	5.78269e-06	3.4832e-06
4.25	1.97243e-06	1.09337e-06
4.75	5.42145e-07	5.4692e-07
5.25	6.33981e-07	3.98423e-07
5.75	3.59774e-07	1.96227e-07
6.25	4.96975e-08	1.33563e-07
6.75	2.32179e-08	2.55642e-08
7.25	3.44877e-08	2.81887e-08

Table B.27: Direct Photon Yield Cu+Cu 62.4 GeV, 10–20%

p_T	yield	error
1.25	0.0352009	0.00323291
1.75	0.00207468	0.000381647
2.25	9.83719e-05	6.89106e-05
2.75	1.9863e-05	1.52032e-05
3.25	1.11552e-05	4.47846e-06
3.75	3.8313e-06	1.95359e-06
4.25	1.43704e-06	1.55535e-06
4.75	0	0
5.25	2.4282e-07	3.83771e-07
5.75	0	0
6.25	0	0
6.75	3.92395e-08	7.48751e-08
7.25	1.37881e-08	2.29986e-07

Table B.28: Direct Photon Yield Cu+Cu 62.4 GeV, 20–30%

p_T	yield	error
1.25	0.0220061	0.00211399
1.75	0.00116467	0.000236384
2.25	2.45621e-05	0.00484687
2.75	9.91754e-06	1.20645e-05
3.25	8.34516e-06	3.89524e-06
3.75	9.12852e-07	6.43705e-07
4.25	3.18005e-07	3.1472e-07
4.75	0	0
5.25	1.87103e-07	2.3403e-07
5.75	6.30963e-08	5.50947e-08
6.25	1.70998e-08	3.57817e-08
6.75	0	0
7.25	1.70752e-08	1.75255e-08

Table B.29: Direct Photon Yield Cu+Cu 62.4 GeV, 30–40%

p_T	yield	error
1.25	0.0133272	0.00135481
1.75	0.000842185	0.00017139
2.25	2.25383e-05	4.2611e-05
2.75	0	0
3.25	4.86911e-06	2.64846e-06
3.75	1.78555e-06	1.26518e-06
4.25	4.00144e-07	2.43726e-07
4.75	0	0
5.25	6.16089e-08	1.75042e-07
5.75	5.13075e-08	3.06648e-07
6.25	2.99714e-08	7.30168e-08
6.75	0	0
7.25	1.20594e-08	1.74439e-08

Table B.30: Direct Photon Yield Cu+Cu 62.4 GeV, 40–50%

p_T	yield	error
1.25	0.00847038	0.000832359
1.75	0.000317616	0.00011848
2.25	0	0
2.75	0	0
3.25	4.78065e-07	2.19198e-06
3.75	0	0
4.25	0	0
4.75	0	0
5.25	2.22248e-08	6.13761e-08
5.75	5.94297e-08	1.56368e-07

Table B.31: Direct Photon Yield Cu+Cu 62.4 GeV, 50–60%

p_T	yield	error
1.25	0.00273329	0.000261848
1.75	0.000124528	3.23376e-05
2.25	0	1.77762e-06
2.75	0	0
3.25	1.01716e-06	3.75532e-06
3.75	4.32814e-07	3.07356e-07
4.25	1.31723e-07	1.64268e-07
4.75	5.69573e-08	6.88885e-07
5.25	0	0
5.75	2.13778e-08	9.68934e-08
6.25	1.0212e-08	1.76519e-08
6.75	4.29719e-09	4.74895e-09

Table B.32: Direct Photon Yield Cu+Cu 62.4 GeV, 60–88%

Appendix C

RHIC Runs

In the PHENIX nomenclature there exits a few redundancies. One example is the term "run number." In one sense run number can refer to the operational year that RHIC provided collisions for data-taking. For instance, the data collected for this analysis is from RHIC's run 5, which was 2005. Table C.1 lists the collision species, energy (per nucleon), and integrated luminosity for each of the run years as of this writing. Alternatively, run number can mean the period of time, anywhere from 30 minutes or so up to one or two hours, over which individual events are recorded. Referring to this latter case, the run numbers used here are listed in table C.2

Run Number	Species	Beam Energy $[GeV/nucleon]$	Integrated Luminosity
Run 1 (2000)	Au+Au	27.9	$< 0.001\ \mu b^{-1}$
	Au+Au	65.2	$20\ \mu b^{-1}$
Run 2 (2001-02)	Au+Au	100.0	$258\ \mu b^{-1}$
	Au+Au	9.8	$0.4\ \mu b^{-1}$
	p+p	100.0	$1.4\ pb^{-1}$
Run 3 (2002-03)	d+Au	100.0	$73\ nb^{-1}$
	p+p	100.0	$5.5\ pb^{-1}$
Run 4 (2003-04)	Au+Au	100.0	$3.53\ nb^{-1}$
	Au+Au	31.2	$67\ \mu b^{-1}$
	p+p	100.0	$7.1\ pb^{-1}$
Run 5 (2004-05)	Cu+Cu	100.0	$42.1\ nb^{-1}$
	Cu+Cu	31.2	$1.5\ nb^{-1}$
	Cu+Cu	11.2	$0.02\ nb^{-1}$
	p+p	100.0	$29.5\ pb^{-1}$
	p+p	204.9	$0.1\ pb^{-1}$
Run 6 (2005-06)	p+p	100.0	$88.6\ pb^{-1}$
	p+p	31.2	$1.05\ pb^{-1}$
Run 7 (2006-07)	Au+Au	100.0	$7.25\ nb^{-1}$
	Au+Au	4.6	*small*
Run 8 (2007-08)	d+Au	100.0	$437\ nb^{-1}$
	p+p	100.0	$38.4\ pb^{-1}$
	Au+Au	4.6	*small*
Run 9 (2008-09)	p+p	250.0	$110.4\ pb^{-1}$
	p+p	100.0	$114.0\ pb^{-1}$
Run 10 (2009-10)	Au+Au	100.0	$10.3\ nb^{-1}$
	Au+Au	31.2	$544\ \mu b^{-1}$
	Au+Au	19.5	$206\ \mu b^{-1}$
	Au+Au	3.85	$3.2\ \mu b^{-1}$
	Au+Au	5.75	$7.8\ \mu b^{-1}$
Run 11 (2010-11)	p+p	250.0	–
	Au+Au	9.8	$33.2\ \mu b^{-1}$
	Au+Au	100.0	–
	Au+Au	13.5	–
Run 12 (2011-2012)	p+p	100.0	N/A
	p+p	255.0	N/A
	U+U	96.5	N/A
	Cu+Au	100.0	N/A

Table C.1: RHIC collision species for each operational year. The highlighted selection is the data used in this analysis. Note that the center of mass energy ($\sqrt{s}$) is twice the beam energy.

161208	161213	161214	161309	161310	161311	161312	161378	161379	161381
161385	161386	161387	161389	161390	161567	161568	161569	161570	161571
161571	161580	161581	161589	161592	161597	161598	161599	161600	161604
161571	161580	161581	161589	161592	161597	161598	161599	161600	161604
161611	161612	161614	161615	161617	161618	161665	161676	161680	161699
161700	161710	161711	161716	161767	161768	161770	161771	161773	162032
162033	162034	162036	162038	162042	162046	162047	162051	162052	162056
162058	162059	162068	162074	162075	162079	162087	162092	162136	162299
162300	162301	162302	162303	162307	162316	162317	162318	162319	162320
162321	162747	162749	162751	162752	162869	162871	162873	162874	162875
162876	162877	162880	162885	162886	162887	162889	162891	162893	162896
162902	162903	162904	162907	162908	162911	162913	162914	162915	162916
162917	162995	162996	162998	163019	163044	163045	163046	163048	163049

Table C.2: Run numbers used in the analysis